

Diss. ETH No. 13105

The Pion Beta Decay Experiment and A Remeasurement of the Panofsky Ratio

A dissertation submitted to the
Swiss Federal Institute of Technology Zurich (ETHZ)
for the degree of
Doctor of Natural Sciences

presented by

Thomas Flügel

Dipl. Phys.

born Nov. 7, 1968

citizen of Germany

accepted on the recommendation of

Prof. Dr. H. Hofer, examiner

Prof. Dr. H.-C. Walter, co-examiner

March 1999

Der Ball ist rund !
(Sepp Herberger)

Abstract	5
Zusammenfassung	6
1. Introduction	8
2. The Pion Beta Decay Experiment	10
2.1 Theory	10
2.1.1 Fermi Theory of the Beta Decay	10
2.1.1.1 Beta Decay, Parity Violation and V-A Theory	12
2.1.1.2 The Beta Decay of Nuclei	12
2.1.1.3 Beta Decay of the Pion	14
2.1.2 The Standard Model of Electroweak Interactions	14
2.1.3 Cabibbo Theory and Unitarity of the CKM-Matrix	15
2.2 The Pion Beta Decay Experiment at PSI	16
2.2.1 Motivation for a Precise Measurement of the Pion Beta Decay Rate	16
2.2.2 Experimental Technique	18
2.3 The PiBeta Detector	20
2.3.1 Beam Counters and Target	21
2.3.2 Charged Particle Tracking Detectors	21
2.3.2.1 Multiwire Proportional Chambers	21
2.3.2.2 Plastic Scintillator Hodoscope	22
2.3.3 Electromagnetic Calorimeter	23
2.3.4 Mechanical Support Structure	23
2.4 Background and Trigger	24
2.5 Determination of the Rate	26
3. The Electromagnetic CsI Calorimeter	28
3.1 Properties of CsI	29
3.1.1 The Scintillation Process of Alkalihalides	31
3.2 Crystal Inspections	32
3.2.1 Visual Inspection	32
3.2.2 Distance Measurement	32
3.2.3 Ratio of Fast Emission to Total Light Yield	32
3.2.4 Optical Non-uniformity and Light Yield	33
3.2.4.1 Wrapping Material	34
3.2.4.2 Crystal Coating	37
3.2.4.3 Crystal Tomography	37
3.2.4.4 CsI Crystal Uniformity Tests with a ^{137}Cs Source	39
3.2.5 Calibration of the Light Yield	40
3.2.5.1 Photomultiplier and Optical Coupling	41
4. Performance of the CsI-Calorimeter	42
4.1 Refinements to the GEANT Simulation	44
4.2 Angular Resolution and Track Reconstruction	46
4.3 Detector Performance in Beam	50
4.3.1 On-line Calibration	51
4.3.2 On-line Results	52
5. Radiative Decays of Pions and Muons	53
5.1 Clump Finding Algorithm	55

6. The Panofsky Ratio	60
6.1 Theory	60
6.1.1 Pion Nucleon Scattering	61
6.1.1.1 SCX s-wave Scattering	61
6.1.1.2 Pion Photoproduction	62
6.2 Experimental Set-up	63
6.2.1 The Calorimeters	65
6.2.1.1 The CsI Array	65
6.2.1.2 The NaI-Wall	65
6.2.1.3 Trigger	66
6.3 Kinematics	66
6.4 Background Processes	68
7. Analysis of the Panofsky runs	69
7.1 Secondary Pedestal Correction	69
7.2 Gain Matching	71
7.2.1 On-line Gain Matching	71
7.2.2 Off-line Gain Matching	72
7.3 Geometric Corrections for Position Recognition	75
7.4 Summing	77
7.5 Data Analysis and Software Cuts	80
7.5.1 Simulation and Background Discussion	80
7.5.2 Neutron Cut	81
7.5.3 Hodoscope Cut	83
7.6 Photon Spectrum and Fit	83
7.7 Discussion of the Result and Calculation of the Scattering Length $a_1 - a_3$	85
8. Conclusion	87
Appendix	88
Bibliography	91
List of Figures and Tables	95
Acknowledgements	97

Abstract

The rare semileptonic decay $\pi^+ \rightarrow \pi^0 e^+ \nu_e$ ($\pi\beta$) is a fundamental manifestation of the weak interaction and thus allows a stringent test of the standard model. Especially the unitarity of the Cabibbo-Kobayashi-Maskawa matrix, the conserved vector current hypothesis and the calculation of radiative corrections can be proved. The beta decay of the pion is analogous to the superallowed pure Fermi transition in nuclear beta decay. Inconsistencies in the analysis of superallowed nuclear beta decays and, furthermore, ambiguities in the measurement of neutron decay parameters call for a new measurement of the $\pi\beta$ decay rate. The difficulty in measuring the $\pi\beta$ decay rate is due to the small branching ratio of $\sim 1 \cdot 10^{-8}$. The current measurement precision is one order of magnitude lower than theoretical calculations. With the goal to reach an accuracy of 0.5% the Pion Beta Decay experiment (PiBeta) at the Paul Scherrer Institute, Villigen, Switzerland has been assembled.

The signature for the $\pi\beta$ decay is the coincident detection of the pair of photons following π^0 decay after a pion has stopped in the target. A low systematical error for the determination of the $\pi\beta$ decay rate will be achieved by a normalization to the $\pi^+ \rightarrow e^+ \nu_e$ decay. This demands a properly designed detector with a shower calorimeter as the central part. It must be capable to detect the ~ 70 MeV positron from the $\pi^+ \rightarrow e^+ \nu_e$ decay and the ~ 70 MeV photons from the π^0 decay with similar efficiency. This is provided by the spherical PiBeta calorimeter that consists of 240 CsI crystals. It has a high rate capability and also offers good energy resolution and high granularity. With an optimization of the surface treatment an energy resolution of 4.2 MeV FWHM for 70 MeV (beam) positrons was reached. This way, a good suppression of the background event $\mu^+ \rightarrow e^+ \nu_e \bar{\nu}_\mu$ can be achieved.

The PiBeta detector currently is almost entirely equipped and will be prepared for production runs starting in 1999. Results from laboratory measurements and test beam periods also went into the GEANT simulation, such as optical non-uniformity, photon statistics and electronic noise. With the simulation the development of electromagnetic showers in the calorimeter was studied and compared with measurements.

During the beam period in 1996 an array of 40 CsI crystals comprising a fifth of the final PiBeta calorimeter was used to study the response to the decay $\pi^+ \rightarrow e^+ \nu_e (\gamma)$. Since a high efficiency of the PiBeta detector for this process is mandatory to achieve a low systematical error also the radiative decay $\pi^+ \rightarrow e^+ \nu_e \gamma$ must be identified. With the well-matched simulation the overall shower distribution within the PiBeta calorimeter was modelled using a threshold function. With this, a cluster finding algorithm was developed to identify radiative decays. Finally the branching ratio for the decay $\pi^+ \rightarrow e^+ \nu_e \gamma$ with photons exceeding an energy of 5 MeV was obtained to be $(2.9 \pm 1.2) \cdot 10^{-6}$ which agrees well with the theoretical value of $2.7 \cdot 10^{-6}$. This also shows the feasibility of the final PiBeta detector to measure the branching ratio of $\pi^+ \rightarrow e^+ \nu_e \gamma$ within a certain kinematic region. Consequently, the pion vector form factor can be re-measured.

Another beam period in 1997 was dedicated to the calibration of the PiBeta calorimeter with photons. Negative pions therefore were stopped in a liquid hydrogen target. Then either charge exchange or radiative capture occur. The resulting photons with distinct energies were detected in an array of 44 CsI crystals. Additionally the relative strength of the two occurring π -p reactions was determined with high precision thanks to the good energy resolution of the calorimeter. This way, the Panofsky ratio (P) was re-measured. The analysis of the well-separated photon distributions resulted in 1.546 ± 0.010 for P . With this value the isovector π -N scattering length b_1 amounts to -0.085 ± 0.002 inverse pion masses. This result agrees well with the most recent value of $b_1 = -0.00868 \pm 0.0014$ from pionic hydrogen spectroscopy.

Zusammenfassung

Das Standardmodell beschreibt erfolgreich Elementarteilchen und ihre Wechselwirkungen. Insbesondere die Entdeckung postulierter Teilchen wie W^\pm - und Z -Boson und t -Quark machen es zu einem allgemein akzeptierten Modell. Allerdings ist die Abwesenheit einer Erklärung für das Vorhandensein von exakt drei Quark- und Leptonenfamilien, ebenso wie der phänomenologische Ansatz mit 18 freien Parametern - unter anderem die Einfügung der Teilchenmassen - unbefriedigend. Aus diesem Grunde sind neue Modelle beziehungsweise Erweiterungsmodelle erwägenswert. Eine wichtige Aufgabe der Teilchenphysik ist die genaue Untersuchung des Standardmodells und die Suche nach Teilchen, welche von Theorien, wie beispielsweise der Supersymmetrie, vorausgesagt werden. Diesem Zweck dient auch ein Experiment am Paul Scherrer Institut (PSI) in Villigen, Schweiz, wo mit dem "PiBeta-Detektor" der seltene Zerfall $\pi^+ \rightarrow \pi^0 e^+ \nu_e$ - der sogenannte Pion Beta-Zerfall ($\pi\beta$) - untersucht wird.

Die Wahrscheinlichkeit für den Pion Beta-Zerfall ist ausschliesslich durch die Eigenschaften der schwachen Wechselwirkung bestimmt. Mit der angestrebten Messgenauigkeit von 0.5% können theoretische Voraussagen und Rechnungskorrekturen überprüft werden, welche grössenordnungsmässig die gleiche Genauigkeit aufweisen. Das Interesse an diesem Zerfallsmodus ist gegeben durch die Bedeutung des Resultates bezüglich der Universalität der schwachen Wechselwirkung, der Erhaltung des Vektorstromes und der Unitarität der Cabibbo-Kobayshi-Maskawa-Matrix (CKM-Matrix). Die Berechnung der Zerfallswahrscheinlichkeit hiermit führt zu einem Verzweigungsverhältnis von $(1.025 \pm 0.002) \cdot 10^{-8}$.

Die theoretische Beschreibung fusst auf der Fermi-Theorie des Beta-Zerfalls, welche die Kopplungsstärke des hadronischen Stromes der Pionen mit dem leptonischen Strom durch die Fermi-Konstante G_F bestimmt. Deren Gleichheit mit der Kopplungsstärke für den μ -Zerfall ist eine Folge der Universalität der schwachen Wechselwirkung. Weiterhin wird angenommen, dass der vektorielle Anteil des Stromes für Hadronen¹ und Leptonen identisch ist. Ein von den Berechnungen abweichender Wert für die Pion Beta-Zerfallsrate würde diese Hypothesen relativieren.

Die von Glashow, Weinberg und Salam formulierte Theorie der elektroschwachen Wechselwirkung erklärt mit der Parität- und CP-Verletzung auch die Nichterhaltung der Quarkflavour-Quantenzahlen. Dieses wird durch die CKM-Matrix beschrieben, welche durch Drehungen im Raum des elektroschwachen Isospins die Quark-Eigenzustände der elektroschwachen WW darstellt. Mit Kenntnis der Kopplungskonstante kann das Matrixelement V_{ud} , der Kosinus des Cabibbo-Winkels, aus dem Beta-Zerfall bestimmt werden. Mit einem Wert von ~ 0.974 [PDG98] stellt V_{ud} den wesentlichen Beitrag zur quadratischen Summe der Zeilenelemente der CKM-Matrix dar. Ein von eins abweichender Wert hätte weitreichende Konsequenzen für das Standardmodell.

Um experimentell ähnliche Genauigkeiten wie die theoretischen Vorhersagen zu erreichen, ist zum einen eine sehr hohe Detektoreffizienz bei hoher Strahlintensität und zum anderen eine optimale Auslegung des Detektors notwendig. Zur Messung der Pion Beta-Zerfallsrate wird ein Pionenstrahl in einem aktiven Target gestoppt und das in 10^{-16} s in zwei Photonen mit einer Energie von ~ 68 MeV zerfallende π^0 indirekt nachgewiesen. Anstelle einer absoluten Messung wird die Zerfallsrate relativ zu dem Prozess $\pi^+ \rightarrow e^+ \nu_e$ bestimmt, was eine höhere Genauigkeit zulässt, da die Zerfallsrate von $\pi^+ \rightarrow e^+ \nu_e$ auf 0.3% genau bekannt ist. Die relative Messung, welche durch die gegebene Positronenergie von ~ 69 MeV ermöglicht wird, bedingt aber auch, dass die Detektorakzeptanz für beide Prozesse vergleichbar ist. Dies kann mit dem PiBeta-Kalorimeter gewährleistet werden, welches durch Wahl des Szintillatormaterials und der Form hierauf optimiert ist. Die 240 zu einer Kugel angeordneten CsI-Szintillatoren weisen eine hohe Nachweiseffizienz bei einer Raumwinkelabdeckung von 80% auf.

Für die Abgrenzung zu Untergrundereignissen ist eine gute Energieauflösung des PiBeta-Kalorimeters notwendig, da bei dem Zerfall ruhender geladener Pionen vorwiegend Positronen mit einer Energie bis zu 53 MeV aus der Zerfallskette $\pi \rightarrow \mu \rightarrow e$ auftreten. Um die Energieauflösung zu optimieren, sind die

¹ Lediglich ein Formfaktor muss berücksichtigt werden.

Szintillatoren und deren Lichtausbeute optimiert und anschliessend einzeln vermessen und getestet worden. Die Ergebnisse dieser Untersuchungen gehen auch in die Simulation des Detektors ein.

Die fortlaufende Angleichung der Simulation an Messergebnisse und die experimentelle Bestätigung von simulierten Resultaten, lässt Studien über das Verhalten elektromagnetischer Schauer und die Entwicklung von Analyseschritten ebenso zu, wie eine Fehlerabschätzung für Korrekturen und Cuts.

Die vorliegende Arbeit gibt im ersten Teil, ausser einer Einführung in die Theorie des Beta-Zerfalls, einen Einblick in das Pion Beta-Zerfallsexperiment. Hierbei werden die einzelnen Detektorkomponenten und deren Eigenschaften erläutert. Besonderes Gewicht wird dabei auf das elektromagnetische Kalorimeter gelegt. Die Entwicklungsschritte, welche zur Favorisierung der Oberflächenbehandlung mit wellenlängenschiebenden Lack und Teflonfolie führten, werden dargestellt und die Qualitätskontrolle für die CsI-Kristalle erläutert. Darüberhinaus werden einige Simulationen zum elektromagnetischen Kalorimeter und die Auswertung physikalisch relevanter Daten aus zwei Test-Strahlzeiten vorgestellt und diskutiert.

Mit Hilfe von GEANT Simulationen wurde die Winkelauflösung des Kalorimeters bestimmt und das Ergebnis bei einer Teststrahlzeit bestätigt. Der ermittelte Wert von $3.6^\circ \pm 0.2^\circ$ für das auf Nachweiseffizienz und Energieauflösung optimierte Kalorimeter ermöglicht kinematische Berechnungen auch neutraler Teilchen¹ und liefert somit eine weitere Bestimmungsgrösse des zugrundeliegenden Prozesses. Hierauf aufbauend wurde ein Spurrekonstruktions-Algorithmus entwickelt, der die Aufgabe hat, die Verteilung elektromagnetischer Schauer im Kalorimeter daraufhin zu prüfen, ob sie von einem oder von mehreren Teilchen herrühren und die entsprechenden Energien zu bestimmen. Dies ist besonders bei der Betrachtung strahlender Pion- und Myonzerfälle relevant.

Während zufällige Koinzidenzen des Zerfalls $\mu^+ \rightarrow e^+ \nu_e \bar{\nu}_\mu \gamma$ zum $\pi\beta$ -Untergrund beitragen, erlaubt die Bestimmung der Energie- und Winkelverteilung von $\pi^+ \rightarrow e^+ \nu_e \gamma$ die Messung des Verhältnisses der Pion-Formfaktoren, denn mögliche innere Anregungen gehen einher mit der Aussendung von Photonen. Gleichwohl ist der Hauptanteil an strahlenden Zerfällen auf Bremsstrahlungsprozesse zurückzuführen. Unter Anwendung des Spurrekonstruktions-Algorithmus konnte das Verzweigungsverhältnis für $\pi^+ \rightarrow e^+ \nu_e \gamma$ zu $(2.9 \pm 1.2) \cdot 10^{-6}$ für Photonen mit einer Energie über 5 MeV bestimmt werden. Dieses Resultat stimmt gut mit dem berechneten Wert von $2.7 \cdot 10^{-6}$ überein. Dadurch konnte die Anwendbarkeit dieses Verfahrens erwiesen und eine weitere Einsatzmöglichkeit des PiBeta-Detektors aufgezeigt werden.

Schliesslich wurde die Reaktion $\pi^- p \rightarrow \pi^0 n \rightarrow \gamma \gamma n$ benutzt, um das Kalorimeter mit Photonen zu kalibrieren. Hierfür wurden negative Pionen in einem Flüssigwasserstoff-Target zur Ruhe gebracht. Dabei können zwei Reaktionen auftreten, deren relative Stärke das Panofsky-Verhältnis festlegt. Die oben bezeichnete Ladungsaustauschreaktion resultiert in einer Energieverteilung der Photonen zwischen 55 MeV und 83 MeV. Mit geringerer Häufigkeit entstehen ein Neutron und ein Photon im Endkanal. Die Energie dieses Photons beträgt 129.4 MeV. Bei hinreichend guter Energieauflösung lassen sich beide Reaktionen im Photonenspektrum identifizieren. Eine Neubestimmung des Panofsky-Verhältnisses mit einem Teil des PiBeta-Kalorimeters liefert das Ergebnis 1.546 ± 0.010 . Dieses ist proportional zu der isovektoriellen Pion-Nukleon Streulänge b_1 , welche sich hiermit zu $(-0.085 \pm 0.002)/m_\pi$ ergibt.

¹ Für die Spurrekonstruktion geladener Teilchen stehen zwei zylindrische Vieldraht-Proportionalkammern zur Verfügung

1. Introduction

Modern particle physics describes fundamental interactions by the exchange of virtual particles. As photons mediate the electromagnetic interaction, gluons transport the strong interaction and vector gauge bosons the weak interaction. (Gravitation is not yet successfully explained by a quantum theory.) Also the constituents of particles are classified by the standard model. This results in three generations of quarks and leptons. The group theoretical description of fundamental interactions is connected with conservation laws. Experiments showed that weak interaction does not conserve parity and quark flavour, unlike strong interaction. As a result, the quark mass eigenstates do not coincide with the weak isospin eigenstates. The transformation, that is rotation of the quark mass state, is summarized in the Cabibbo-Kobayashi-Maskawa (CKM) matrix [Kob73, Cab63]. This matrix has to be unitary. Several tests aim to verify whether $V_{ud}^2 + V_{us}^2 + V_{ub}^2 = 1$ of which the first element $V_{ud} \sim 0.974$ [PDG98], the cosine of the Cabibbo angle, is the largest contribution; V_{ud} is accessible through beta decay.

In order to achieve a highly precise measurement of V_{ud} , and thus a test of the standard model, the Pion Beta Decay experiment (PiBeta) at the Paul Scherrer Institute (PSI), Villigen, Switzerland investigates the rare semileptonic decay $\pi^+ \rightarrow \pi^0 e^+ \nu_e$ ($\pi\beta$). This process is an exact analogy to the β^+ decay of a nucleus, but lacks the necessity of nuclear corrections. The decay probability of this super-allowed Fermi decay is calculable to 0.2% precision. A measurement of similar precision therefore is essential, but difficult due to the branching ratio of $(1.025 \pm 0.002) \cdot 10^{-8}$. With the prospected measurement precision of 0.5%, the conserved vector current (CVC) hypothesis and radiative corrections due to quantum electrodynamics can be proved, as well. An even higher precision of about 0.3% could be achieved after a remeasurement of the $\pi^+ \rightarrow e^+ \nu_e$ decay rate and then also the universality of the weak interaction would be tested. Competitive measurements to prove the unitarity of the CKM matrix have either shown ambiguous results or were consistent but lacked the desired precision. The currently most accurate measurement of the pion beta decay branching ratio has an error of 3.8% [Dep68].

Several considerations led to the present form of the Pion Beta decay experiment in order to provide the desired accuracy. A π^+ beam of high intensity will be stopped in an active target and the pair of photons from the nearly instantaneous (10^{-16} s) decay $\pi^0 \rightarrow \gamma\gamma$ then provides a clear signature of a $\pi\beta$ event. Rather than an absolute measurement of the decay rate, a relative measurement is desirable because of a lower systematical error. This will be achieved by the normalization to the decay $\pi^+ \rightarrow e^+ \nu_e$. In order to obtain similarly high efficiencies for the positrons from $\pi^+ \rightarrow e^+ \nu_e$ and the $\pi\beta$ -photons, which are of similar energy, a spherical shower calorimeter with good energy resolution and fast response was built. Therefore 240 hexagonal and pentagonal CsI crystals form a sphere that covers 80% of the 4π sr solid angle. It provides good energy resolution, fast response and a high granularity. Using the concept of a self supporting structure only little non-sensitive material is used. CsI was chosen as the scintillating material because it delivers relatively high light yield with a fast response. Furthermore it provides the best stopping power and shortest radiation length compared to similar materials.

In order to achieve a good energy resolution the light yield of the scintillators has to be maximized. Additionally the quality of each CsI crystal that went into the calorimeter was reviewed carefully. For a good energy resolution also a uniform response of light over nearly the entire crystal volume is necessary. The surface treatment of the crystals therefore was optimized. It was found that two layers of Polytetrafluor-Ethylene (PTFE) foil with an additional layer of aluminized mylar provide both good light yield and uniformity. The crystals were also painted with a layer of wavelength shifting lacquer to enhance diffuse reflection. As a result of this treatment the energy resolution for 70 MeV (beam) positrons was improved from 5.2 MeV to 4.2 MeV FWHM between the beam periods in 1996 and 1997. The results of the scintillator studies are also important parameters for the Monte Carlo simulations of the detector.

The disadvantage of a stopped pion experiment is the positron background due to the decay chain $\pi \rightarrow \mu \rightarrow e$ with a maximum positron energy of 53 MeV. In order to discriminate background events, an efficient triggering and a good energy resolution of the calorimeter are mandatory. This background event can be identified by the timing structure of the decaying muon. Furthermore the energy resolution of 4.2 MeV for 70 MeV positrons is ample to discriminate this source of background.

The present work will report on the developments and experimental result during the production and final assembly stage of the PiBeta detector¹. Furthermore two test beam periods that took place during the development phase with a subset of the final detector are described. These beam periods were planned for detector calibration but also led to basic physical results where one is the radiative pion decay probability and the other the so-called Panofsky ratio [Pan50].

In parallel to the evaluation of the detector parts a GEANT simulation was initiated. Results from laboratory test and beam periods went into the simulation code, such as optical non-uniformity, photon statistics and electronic noise. Having reached consistency between data and simulation of the calorimeter response [Bro96], several studies became possible. With this, the comparison of shower developments of positrons and photons within the calorimeter was of large interest. On top of that a track reconstruction and cluster finding algorithm was developed. With the use of track reconstruction the angular resolution was determined with the simulation to be $3.6^\circ \pm 0.2^\circ$ for 70 MeV positrons. A comparison to 70 MeV beam positrons could confirm this result. The angular resolution further depends on energy and particle type because of differently developing showers. In general, one obtains from simulations that positrons start to shower earlier than photons due to their charge with a slightly wider cone. With higher energies the shower penetrates deeper into the calorimeter (for both positrons and photons) while the transverse shower spread becomes smaller. For example 70 MeV photons have a mean shower depth of 7.6 cm at a cone radius of 2.6 cm. This proves that the uniform response of the first half of a crystal is crucial.

Another problem to be addressed is untypical development of electromagnetic showers that show some widespread depositions of small fractions of the particle energy within the calorimeter. The overall shower distribution within the PiBeta calorimeter could be modelled using a threshold function which requires that at least 98% of the shower energy are contained within the area under the graph of that function. This threshold function can be used twofold when implemented in a track finding algorithm. I) It offers a clustering routine in order to rebuild the deposited shower energy. II) It decides whether the deposited energy originates from one or more incoming particles. With the help of the algorithm the probability to find the radiative decay $\pi^+ \rightarrow e^+ \nu_e \gamma$ with a photon energy exceeding 5 MeV was obtained to be $(2.9 \pm 1.2) \cdot 10^{-6}$. This agrees well with the theoretical value of $2.7 \cdot 10^{-6}$. At lower photon energies the radiative decay mostly emerges from inner bremsstrahlung, while higher photon energies - which occur with lower probability - give access to the ratio γ of the pion form factors. This ratio can be remeasured with high statistics using the complete PiBeta detector.

The 1997 beam time was foreseen for calorimeter calibration with both 70 MeV positrons and photons. In order to generate the photons a liquid hydrogen target was used to stop negative pions. The charge exchange reaction then delivers photons from 55 MeV up to 83 MeV due to the π^0 decay into a pair of photons within 10^{-16} s. With the use of a NaI detector array to tag one of the photons the desired photon energy was chosen. As a competitive reaction also radiative capture occurs, where the intermediate pionic hydrogen transforms into a 8.9 MeV neutron and a 129.4 MeV photon. The ratio of both possible reactions can be obtained with a calorimeter of good energy resolution. This measurement was carried out using an CsI-array of 44 crystals. The so-called Panofsky ratio P is directly proportional to the pion-nucleon scattering length b_1 . With the obtained value of 1.546 ± 0.010 for P , b_1 becomes (-0.085 ± 0.002) in units of inverse pion masses.

¹ Meanwhile it became ready to operate

2. The Pion Beta Decay Experiment

The goal of this experiment is the measurement of the rate of the rare decay $\pi^+ \rightarrow \pi^0 e^+ \nu_e$ ($\pi\beta$) with an accuracy of 0.5%. The β -decay of the pion is analogous to the superallowed pure Fermi transition in nuclear β -decay since pions are spinless. It is a fundamental semileptonic weak interaction processes and thus calculable with minimal model-dependent corrections. The accuracy of the theoretical description allows a very precise test of the standard model of electroweak interactions if the experimental result is of comparable precision. This will allow to prove theoretical calculations of the decay rate including radiative corrections and consequently probe the unitarity of the Cabibbo-Kobayashi-Maskawa mixing matrix.

Before the description of the experimental technique the motivation and the importance of a precise measurement shall be explained. The theoretical description shall start with an introduction to the nuclear β -decay using the Fermi theory of point interaction including the conserved vector current (CVC) hypothesis, followed by the description of the electroweak interaction and the CKM-matrix.

2.1 Theory

One of the radioactive decays, which were discovered by Bequerel (1896) and investigated by Curie (1898), is the so-called (Thomson in 1899) β -decay. At first it was observed on the heaviest natural isotopes with an excess of neutrons. The ' β -particle' was found to be an electron emitted by the nucleus inside which a neutron transformed into a proton. Because of unexplainable discrepancies regarding conservation laws and the Pauli-principle, Pauli in 1930 proposed the (probably massless) neutrino. This β -decay then could be regarded as the interaction of four fermions, which theoretically was first described by Fermi [Fer34].

2.1.1 Fermi Theory of the Beta Decay

In the generic decay $n \rightarrow p e \bar{\nu}$ a neutron couples to a vector field and hence becomes a proton while the incoming neutrino turns into an electron. In this picture at a single-point in space time the neutron wavefunction is transformed into that of the proton as the neutrino wavefunction transforms into that of the electron, since the anti-neutrino can be regarded as a neutrino that travels backward in time. The strength of the coupling in the single-point has to be obtained experimentally.

Fermi's idea was to compare the four-fermion point interaction as an interaction of two currents in analogy to the electromagnetic interaction. For proton-electron scattering, for instance, the matrix-element can be written as

$$M = -\frac{4\pi\alpha^2}{q^2} J_\mu^p J_e^\mu.$$

J represents the current densities for proton and electron, respectively, and q the momentum transfer. Here the proton couples to the electron with the strength α which is known as the fine structure parameter $\alpha = e^2/4\pi\epsilon_0\hbar c$.

Fermi consequently introduced the weak current that decomposes into a hadronic and a leptonic current. Using the picture of second quantization (field quantization) the transition operator can be pictured as annihilator of the particle of the right hand side and creator of the particle on the left hand side. In the theory of four-fermion point interaction two particles are transformed simultaneously and therefore one writes the matrix element [Fey58]

$$M = \sum_i g_i (\bar{\Psi}_p \Omega_i \Psi_n) (\bar{\Psi}_e \Omega_i \Psi_\nu).$$

The operators Ω_i are denoted accordingly to their behaviour under parity transformations (see below) accompanied with their coupling constants g_i . Ψ represent the wave functions of the fermions participating in the β -decay, since they are solutions of the Dirac equation for free particles

$$\left(i\hbar \gamma^\mu \frac{\partial}{\partial x^\mu} - mc \right) \Psi(x^\mu) = 0.$$

In order to describe observables (which must be real expressions) in the Dirac theory¹, bilinear forms like $\bar{\Psi} \Omega \Psi$ with Ω being a 4x4 hermitean matrix, have to be generated. This results in 16 linear independent basic matrices which are be classified as follows

$$\begin{aligned} (\text{Scalar}) \quad \Omega_S : S &\equiv \bar{\Psi} \Psi \\ (\text{Vector}) \quad \Omega_V : V^\mu &\equiv \bar{\Psi} \gamma^\mu \Psi \\ (\text{Pseudoscalar}) \quad \Omega_P : P &\equiv \bar{\Psi} \gamma^5 \Psi \\ (\text{Axialvector}) \quad \Omega_A : A^\mu &\equiv \bar{\Psi} \gamma^\mu \gamma^5 \Psi \\ (\text{Tensor}) \quad \Omega_T : T_{(\mu \neq \nu)}^{\mu\nu} &\equiv \bar{\Psi} (\gamma^\mu \gamma^\nu - \gamma^\nu \gamma^\mu) \end{aligned}$$

with

$$\gamma^0 = \begin{pmatrix} 0 & 1 \\ 1 & 0 \end{pmatrix}, \gamma^i = \begin{pmatrix} 0 & \sigma^i \\ -\sigma^i & 0 \end{pmatrix}, \gamma^5 = \gamma^0 \gamma^1 \gamma^2 \gamma^3 = \begin{pmatrix} \sigma^0 & 0 \\ 0 & -\sigma^0 \end{pmatrix} \quad (i=1,2,3)$$

where σ^i are the Pauli spin matrices and 1 the unit matrix.

This set of matrices guarantees that solutions of the Dirac equation also will fulfil Lorentz-invariance. The parity operator can be introduced by building the chiral projection operators:

$$P_R = \frac{1+\gamma^5}{2} = \begin{pmatrix} 1 & 0 \\ 0 & 0 \end{pmatrix} \text{ and } P_L = \frac{1-\gamma^5}{2} = \begin{pmatrix} 0 & 0 \\ 0 & 1 \end{pmatrix}$$

one sees that with the help of these operators one can project the chirality state of the spinor

$$\chi_L = P_L \begin{pmatrix} \chi_R \\ \chi_L \end{pmatrix} = \frac{1-\gamma^5}{2} \begin{pmatrix} \chi_R \\ \chi_L \end{pmatrix} = \begin{pmatrix} 0 & 0 \\ 0 & 1 \end{pmatrix} \begin{pmatrix} \chi_R \\ \chi_L \end{pmatrix} = \begin{pmatrix} 0 \\ \chi_L \end{pmatrix}$$

(and analogous for the right-handed component).

The chiral symmetry was introduced by Feynman and Gell-Mann to account for parity violation, which was not known to Fermi. It can be shown that only V- and A-coupling correctly describe the maximal parity violation, since

$$(\bar{\Psi}_e \Omega_i P_R \Psi_\nu) = (\bar{\Psi}_e P_L \Omega_i \Psi_\nu) \text{ for } i = V, A.$$

Using this, the matrix element becomes

$$M = G_V \left(\bar{\Psi}_p \gamma^\mu (1 - \lambda \gamma_5) \Psi_n \right) \left(\bar{\Psi}_e \gamma^\mu (1 + \gamma_5) \Psi_\nu \right); \quad \lambda = \frac{G_A}{G_V}.$$

In this form one sees that axial coupling is affected by the strong interaction, while the pure leptonic process couples with the strength G_V . This also is an important claim of the CVC-Hypothesis, namely that the form factors of leptons are unity and therefore are not renormalized by strong interaction. The

¹ Here the Weyl representation is used.

CVC hypothesis is a direct consequence of the analogy to the electromagnetic interaction, as there is conservation of charge. As a result the coupling of the lepton current to the hadron current must be of equal strength not regarding whether there are nucleons or pions. So the Pion Beta decay rate is calculable like above.

2.1.1.1 Beta Decay, Parity Violation and V-A Theory

The evidence for parity violation in β -decay has been established by two epochal experiments shortly after Lee and Yang formulated its possible occurrence. Wu et al. [Wu57] discovered the polarisation asymmetry of electrons in the β -decay of polarised ^{60}Co ; a year later Goldhaber et al. [Gol58] found the complete polarisation of neutrinos by measuring the photon spin direction determined by the deexcitation of a $^{152}\text{Eu}^*$ nucleus after K-capture. In order to account for the chiral symmetry breaking of the weak interaction only left-handed fermions participate and the mediating particles must be vectors of spin 1 and left-handed, as well. As a consequence the transition operators must be of the (V-A) kind, since only vector- and axial vector- coupling correctly describes maximal parity violation.

A textbook example to verify (V-A) theory is the calculation of pion-decay into leptons, since parity violation in pion and muon decays was observed along with the nuclear β -decay measurements mentioned above. Following the four fermion interaction picture with replacing the pion by a hadronic current of an up-quark changing into a down quark in the single-point, which demands universality of the weak interaction. It claims an universal coupling constant for all lepton decay and scattering processes (the equivalence of the coupling strength for weak interacting hadronic particles is expressed in the CVC hypothesis). In this example of a pion decay into leptons the conservation of angular momentum then determines the spin direction of the charged leptons, which have to be opposite to the (anti-)neutrino since pions do not carry spin. Finally, regarding conservation of momentum, the charged leptons have the same chirality as the neutrinos. The helicity of the neutrino must be -1. Hence, neutrino helicity determines the chirality of the charged lepton. Due to the fact that the probability to find a massive particle with unfavourable helicity goes with $1-\beta$, the rate of the decay $\pi^+ \rightarrow e^+ \nu_e$ should be lower than for $\pi^+ \rightarrow \mu^+ \nu_\mu$. With the approximation $m_e^2/m_\pi^2 \ll 1$ the ratio of decay rates turns out to be

$$R = \frac{\pi \rightarrow e\nu}{\pi \rightarrow \mu\nu} = \frac{1-\beta_e}{1-\beta_\mu} \cdot \frac{(m_\pi^2 - m_e^2)^2}{(m_\pi^2 - m_\mu^2)^2} \equiv \frac{m_e^2}{m_\mu^2} \left(\frac{1}{1 - m_\mu^2/m_\pi^2} \right)^2 = 1.275 \cdot 10^{-4},$$

where the first term describes the ratio of probabilities to generate a right-circular electron or muon, the second term represents the phase space difference. From the masses alone the $\pi^+ \rightarrow e^+ \nu_e$ decay would have been favoured by a factor of 5.5 (assuming scalar interaction)[Per87]. The experimental value is $(1.267 \pm 0.023) \cdot 10^{-4}$ [PDG98] and thus confirms the validity of (V-A) interaction.

2.1.1.2 The Beta Decay of Nuclei

The transition-rate of the process $n \rightarrow p e \bar{\nu}$ is calculable by first order time dependent perturbation theory also known as Fermi's 'golden rule', resulting in

$$w = P(E) dE = \frac{2\pi}{\hbar} G^2 |M|^2 \frac{dn_f}{dE_0}.$$

Here w is the probability density for an electron to be emitted in the energy interval $E+dE$. The expression $\frac{dn_f}{dE_0}$ represents the density of final state, M the transition matrix and G a combination of coupling constants.

After a short calculation (see [Kal72] for example) and integration over the electron energies one obtains for the decay width:

$$\Gamma = \frac{\ln 2}{t} = P(E) = G^2 f \frac{\ln 2 |M|^2}{K} \quad \text{with } K = \frac{2\pi^3 \hbar^7 c^6 \ln 2}{(mc^2)^5}.$$

The function f comprises the kinematic terms of the integrated state density and the electromagnetic interaction of the electrons and t represents the half-life. The connection of ft -values, which are used to classify the β -decays, to the coupling constant one obtains after calculating the matrix element. Here the simplest case is a transition without a flip of the nucleon spin (I) and thus with anti-parallel electron and neutrino spins. An example of this pure Fermi transition is the inverse β -decay $^{14}\text{O} \rightarrow ^{14}\text{Ne}^+ \nu$. In order to calculate the matrix element one forms an isospin $T=1$ triplet of isotopes with the atomic number $A=14$. The isospin positions T_z are calculated assuming a ^{12}C core with additional nucleons

$$\begin{array}{cc} & T_z \\ ^{14}\text{O} & 1 \\ ^{14}\text{N} & 0 \\ ^{14}\text{C} & -1 \end{array}.$$

Due to the spin pairing of the nucleons this triplet does not carry a net spin. Because of a transition without spin change ($0 \rightarrow 0$) the ^{14}O decay is an example of a pure Fermi decay. Hence, the calculation of the matrix element M simplifies to sum over isospin T with $T_z=1$ in the initial state and $T'_z=0$ in the final. One obtains

$$M = \sqrt{T(T+1) - T_z T'_z} = \sqrt{2} \quad \text{and finally } ft = \frac{K}{2G_V^2},$$

since terms other than of vector type do not contribute

Nuclear β -decays are classified according to their $\log(ft)$ -values:

Type of transition	ΔI	parity	$\log(ft)$ value
super-allowed	0	+	~ 3.5
allowed	0,1, no $0 \rightarrow 0$	+	~ 5.7
(multiple) forbidden	0,1 or >1	-	> 7.5

Table 2-1 Classification of β -decays [Mey84]. ΔI means the change of nuclear spin.

Before one can extract the exact coupling constant from the ft -value, corrections have to be taken into account (see [Wil94,97] for a comprehensive discussion. Those are

- radiative corrections δ_r (from QED and QCD) of 3-4%
- nuclear correction δ_c of 0.2-1%
- screening effects due to Coulomb interaction with the core

Thus one writes $f^*t = ft (1+\delta_r) (1-\delta_c)$. The rate of the pure Fermi nuclear β -decay is directly related to the vector coupling constant assuming the CVC hypothesis that claims the coupling to the hadronic current independent from the participating particles. Pions and nucleons therefore can be treated equally within this theory. Furthermore the standard model assumes the existence of an universal coupling constant for all weak processes. Hence, measuring the decay rate of a β -decay, G_V can be obtained or, taking G_μ from the muon decay, universality of the weak interaction can be tested.

2.1.1.3 Beta Decay of the Pion

Since pions are forming a spin 0 triplet with isospin $T=1$, a transition between two pions is analogous to the superallowed nuclear Fermi β -decay and therefore the pion beta decay $\pi^\pm \rightarrow \pi^0 e^\pm \bar{\nu}$ can be

described in the same way. Opposed to the nuclear β -decay neither inner nor outer nuclear corrections have to be taken into account; only radiative corrections (calculable with an accuracy of 0.2% [Sir92]) have to be considered. Thus the pion beta decay rate can be calculated with higher precision. A simple estimation of the pion beta decay rate can be done using the Sargent rule that asserts the dependence of the decay probability over time to the fifth power of the energy [Per86]. This gives

$$P = \frac{mc^2}{\hbar} G_V^2 \frac{\Delta^5}{30\pi^3} = 0.43s^{-1},$$

since the pion mass difference Δ is the source of the transition energy ($\Delta = m_{\pi^+} - m_{\pi^0} = 4.5937 \text{ MeV}$ [Cza93]). With an exact calculation including radiative corrections one gets after Källén [Kal72]:

$$\frac{1}{\tau_{\pi\beta}} = \frac{G_V^2 \Delta^5}{30\pi^3} \left(1 - \frac{\Delta}{2m_{\pi^+}}\right)^3 f' \times (1 + \delta_\pi)(1 - \delta_\mu) = (0.391 + 0.012 - 0.003)s^{-1} \pm 0.2\% .$$

(A more recent calculation by Sirlin [Sir92] gives $(0.3996 \pm 0.0006) s^{-1}$).

Here the function f is representing the integrated state density including electroweak corrections, δ_π the radiative corrections for the π of 0.012, and δ_μ represents the radiative correction for the $\mu^+ \rightarrow e^+ \nu_e \bar{\nu}_\mu$ decay. With the pion lifetime of 26.03 ns this is equivalent to a branching ratio (BR) of $1.031 \cdot 10^{-8}$ or a ratio of $0.838 \cdot 10^{-4}$ compared to our calibration decay $\pi^+ \rightarrow e^+ \nu_e$.

2.1.2 The Standard Model of Electroweak Interactions

In analogy to the isospin of the strong interaction one classifies the known fundamental particles accordingly to their weak isospin T^w . Since the weak interaction is maximum parity violating they form a left-handed doublet that carries weak charge and a right-handed singlet that does not. The latter therefore is identified with the projection $T_z^w = 0$.

Weak Isospin	1 st Generation	2 nd Generation	3 rd Generation
$T_z^w = +\frac{1}{2}$	$\begin{pmatrix} \nu_e \\ e^- \end{pmatrix}_L$	$\begin{pmatrix} \nu_\mu \\ \mu^- \end{pmatrix}_L$	$\begin{pmatrix} \nu_\tau \\ \tau^- \end{pmatrix}_L$
$T_z^w = -\frac{1}{2}$	$\begin{pmatrix} u \\ d \end{pmatrix}_L$	$\begin{pmatrix} c \\ s \end{pmatrix}_L$	$\begin{pmatrix} t \\ b \end{pmatrix}_L$
$T_z^w = 0$	$\begin{pmatrix} e^- \\ \nu_e \end{pmatrix}_R$	$\begin{pmatrix} \mu^- \\ \nu_\mu \end{pmatrix}_R$	$\begin{pmatrix} \tau^- \\ \nu_\tau \end{pmatrix}_R$

Table 2-2 The generations of quarks and leptons in the standard model of electroweak interaction.

The logical consequence of the analogy of the weak interaction to electromagnetism is the advent of a particle¹ mediating the weak force like the photon mediates the electromagnetic interaction with the coupling constant α . The coupling constant of the weak interaction then is G_V , furthermore the electric charge conservation law corresponds to the conservation of the vector current. Within the electroweak theory the beta transition is described using a virtual gauge vector boson (W-Boson) that couples the hadronic current to the leptonic current with equal strength. For a vanishing momentum transfer $q^2 \ll M_W^2$, where M_W represents the mass of the W, the coupling constant g_w of the W-Boson is directly related to G_V via

$$\frac{g_w}{8M_W^2} = \frac{G_V}{\sqrt{2}} .$$

¹ As seen before this necessarily has to be a boson obeying vector coupling.

The success of formulating local gauge invariance with non-Abelian symmetry groups, i.e. SU(2) - introduced by Yang and Mills - and the maximum chiral symmetry breaking of the weak interaction led to the electroweak interaction theory that was independently formulated by Weinberg and Salam based on previous work of Glashow [Gla61]. Herein the weak isospin group SU(2) was combined with the weak hypercharge group U(1) in order to account for charge conservation.

Characteristic is the spontaneous symmetry breaking of the SU(2)xU(1) group by the Higgs field that explains the short reach of the weak interaction. This led to the prediction of the intermediate massive Vector-Bosons and their total chiral asymmetry. On top of that the U(1) symmetry remained unbroken and the (massless) intermediate Vector-Bosons was identified as the photon. This fundamental concept of gauge invariance and spontaneous symmetry breaking was verified later; at first, theoretically, when t'Hooft proved the renormalizability in 1971 before the predicted neutral currents were found (1973). Finally, the triumph for the Glashow-Weinberg-Salam theory of electroweak interaction was the discovery of the W^\pm - and Z^0 -Bosons (1983). (Up to now only the Higgs-Boson remained undiscovered.)

The CVC Hypothesis in the framework of the SU(2)xU(1) electroweak group is a direct consequence of the Noether theorem that claims a conserved quantity for any continuous symmetry. Unlike axial transformations, vector rotations in hadronic flavour space leave the vacuum invariant and therefore a conserved vector current must exist.

2.1.3 Cabibbo Theory and Unitarity of the CKM-Matrix

While the weak interaction conserves the lepton number, it violates the conservation of the quark flavour. This was observed in rare decays which showed that strangeness, for instance, was not a good quantum number. Rather than introducing quark-quark coupling constants, Cabibbo, in order to preserve universality, proposed the new quark eigenstates d' and s' . They are calculated by rotation of the quark eigenstates of the flavour-preserving strong interaction. For example $s' = s \sin \theta_C + d \cos \theta_C$, with θ_C being the Cabibbo mixing-angle. The generalization by Glashow, Iliopoulos and Maiani in 1970 led to the proposal of the C-quark by Björken and Glashow as a consequence of (weak) isospin symmetry. After the discovery of CP-violation in 1964, Kobayashi and Maskawa extended the model by introducing phase factors and proposing a third generation of heavier quarks. The quark-mixing between the three generations is summarized in the CKM mixing matrix.

$$\begin{pmatrix} d' \\ s' \\ b' \end{pmatrix} = \begin{pmatrix} V_{ud} & V_{us} & V_{ub} \\ V_{cd} & V_{cs} & V_{cb} \\ V_{td} & V_{ts} & V_{tb} \end{pmatrix} \begin{pmatrix} d \\ s \\ b \end{pmatrix}.$$

Now vector coupling can be related directly to leptonic decays. Due to the absence of quark-mixing in leptonic decay, because of universality, the vector coupling constant can be expressed in terms of the muon decay constant $G_\mu = G_V/V_{ud}$. The matrix element V_{ud} therefore can be determined by measuring the pion beta decay branching ratio. The further elements of the first row - as recommended by [PDG98] - are 0.2196 ± 0.0023 for V_{us} and 0.00316 ± 0.0009 for V_{ub} .

The classification of elementary particles and their interactions, furthermore the successful discovery of proposed fundamental particles like the gauge vector bosons of electroweak interaction [Ua183a,Ua183b] and the t-quark [Aba95,Abe95], makes the standard model (SM) a trusted fundament of modern physics. Controversially, the phenomenological ansatz with 18 free parameters and the purpose to find a unified quantum field-theory description of the fundamental interactions would make an extension of the standard model desirable. Among the possibilities we mention the Minimal Supersymmetric Standard Model and the String model. They are suggesting either an additional set of elementary particles or more fundamental constituents of the particles currently considered elementary. These elementary particles are classified into three families of quarks and leptons each. Unexplained

evidence like the presence of a chiral symmetry group which is parity violating, the origins of mass, mixing angles and CP-violating phase give raise for possible physics beyond standard model.

The standard model predicts the unitarity of the CKM matrix. A distinct deviation from this demands an expansion of the standard model or new physics. The main concepts are briefly summarized:

- Existence of a fourth generation of heaviest quarks and - presumably - leptons¹.
- A supersymmetric extension of the minimal SM predicts the existence of a bosonic partner of every fundamental fermion and a fermionic partner of every fundamental boson. The supersymmetric partners are considered to be heavier than 100 GeV; but the exchange of supersymmetric particles would affect muon and B-meson decays, for example. The effect of electroweak symmetry breaking also would violate the conservation of lepton numbers. [Moh92]
- The existence of a right handed W_R gauge boson would result in an admixture of (V+A)-interactions to the (V-A)-theory [Wil94].
- Additional neutral gauge bosons Z' - which are predicted by some 'Grand Unification Theory' models - would lead to higher order corrections for the calculation of the decay rate due to possible quantum loop corrections.[Mar87]
- Compositeness of elementary fermions and vector gauge bosons would lead to a correction of the quark mixing angles.[Sir89]

2.2 The Pion Beta Decay Experiment at PSI

2.2.1 Motivation for a Precise Measurement of the Pion Beta Decay Rate

A precise measurement of the pion beta decay ratio allows a test of the CVC hypothesis and unitarity of the CKM-Matrix. Although other experiments have done excellent work in this field, a new measurement has to be considered in order to meet the same precision as the theoretical calculation. On top of that there is a discrepancy in the interpretation of neutron decays data, as well as for superallowed nuclear β -decay.

The most current analysis of the nuclear β -decay comprises a fit of the determined ft values of 9 superallowed $0^+ \rightarrow 0^+$ transitions. After a remeasurement of four half-lives Koslowski et al. [Kos97] are obtaining an average ft -value of (3072.3 ± 2.0) s which results² in $V_{ud} = 0.9740 \pm 0.0005$. Although they claim no significant deviation from CVC predictions at the $4 \cdot 10^{-4}$ level, the unitarity test fails by more than two standard deviations since $V_1 = V_{ud}^2 + V_{us}^2 + V_{ub}^2 = 0.9972 \pm 0.0013$. Opposed to that finding Wilkinson [Wil94] propagates a Z^2 -dependent radiative correction based on theoretical considerations [Sir87] which can be achieved using a three parameter fit of the 9 precision data of superallowed transitions. He obtains $V_1 = 1.0000 \pm 0.0017$ which is also supported by the least χ^2 -value for that three parameter fit; but the implementation of a Z^2 -dependent correction due to a phenomenologically QCD-dependence is not necessarily consistent with the CVC hypothesis anymore. Although Wilkinson can add the datum of the ^{10}C superallowed β -decay on cost of the a slightly higher error [Wil94], Savard et al.[Sav95] favour a linear extrapolation to $f^t(Z=0)$ because of a significantly lower systematical error. Their result shows consistency with the one of [Kos97] at a slightly higher uncertainty.

Neutron lifetime measurements - and hence the evaluation of neutron ft -values - are of similar precision as superallowed nuclear β -decay transition measurements; but due to the influence of the strong

¹ This would demand a heavy neutrino with a mass beyond half a W-Boson mass

² This result also is recommended by [PDG98]; but with an increased error of 0.0010

interaction the axialvector coupling constant G_A must be obtained independently to calculate V_1 . The ft -value of the free neutron decay is related to the coupling constants as follows

$$ft = \frac{K}{G_V^2 + 3G_A^2} = \frac{K/G_V^2}{1 + 3\lambda^2}.$$

While G_A can not be measured directly, λ is available through the angular distribution of the electrons with respect to the direction of the decaying polarised neutron. The so-called beta decay asymmetry parameter A_0 was obtained to -0.1160 ± 0.0015 [Lia97] and is related to λ by

$$A_0 = -2 \frac{\lambda^2 + \lambda}{1 + 3\lambda^2} \text{ and hence } \lambda = -1.266 \pm 0.004.^1$$

Measurements of the neutron lifetime τ_n have been achieved using two methods; either using neutrons from a reactor or an accelerator or via storage of (ultra-)cold neutrons (UCN). Unfortunately the obtained results differs significantly (more than two standard deviations) from each other.

The method of neutron storage allows the determination of τ_n by the decay law

$$N(t) = N_0 e^{-t/\tau_n} \text{ using } 1/\tau_n = 1/\tau_n + 1/\tau_l, \text{ where } 1/\tau_l$$

represents the probability for neutron losses at the side walls of the trap. An average of the so obtained results gives $\tau_n = 885.9 \text{ s} \pm 1.7 \text{ s}$ [Mos96]. With beam methods τ_n is determined by measuring the change in the beam flux due to neutron β -decay. The neutron lifetime then is proportional to the ratio of neutron amount N divided by the amount of neutron decays (dN/dt). The latter is obtained using the proton or electron energy spectrum. The obtained neutron lifetime from beam experiments amounts in average to $\tau_n = 894.2 \text{ s} \pm 4.2 \text{ s}$ [Mos96].

Although the averaged value of 886.7 ± 1.9 [PDG98] - in connection with the above given λ - is consistent with the unitarity of the CKM-matrix ($V_1 = 1.0005 \pm 0.0032$), the inherent inconsistency of neutron lifetime measurements and the obtained asymmetry parameter value demands an independent test. Nevertheless, more accurate measurements are planned for both beam neutron decay [Mak98] and stored UCN [Sch95, Uts98].

Previous measurements of the pion beta decay rate are in good agreement with the standard model but have too large an uncertainty to prove theoretical calculations. The most recent determinations of the pion beta decay rate are:

$$\text{Depommier et al. (1968): } 0.38 \pm 0.03 \text{ s}^{-1} \text{ [Dep68]}$$

$$\text{McFarlane et al. (1985): } 0.394 \pm 0.015 \text{ s}^{-1} \text{ [McF85]}$$

These experiments that measured the pion beta decay rate prior to PiBeta are suffering a high uncertainty. In addition to a relatively low total number of $\pi\beta$ events, the major contribution to the error origins from the determination of the detector efficiency or acceptance.

Depommier et al. [DEP68] used a carbon degrader and an active CH_2 target to stop 77 MeV pions at a rate of $\sim 3.5 \cdot 10^4/\text{s}$. Their calorimeter consisted of an array of eight lead-glass counters that covered 60% of the 4π sr solid angle. The radial thickness was equivalent to 6.8 radiation lengths. The detector efficiency was calibrated using the charge exchange reaction $\pi^+ p \rightarrow \pi^0 n$ (SCX) followed by $\pi^0 \rightarrow \gamma\gamma$ with a precision of 3.6%. This way they obtained a branching ratio of $1.00^{+0.08}_{-0.1} \cdot 10^{-8}$.

Seventeen years later McFarlane et al. [McF85] used an intense pion beam ($2 \cdot 10^8 \pi/\text{s}$) at LAMPF to measure the branching ratio with higher precision. The measurement of the decay in flight helped to reduce the background due to the Michel decay of the muon at the cost of a low acceptance for the detection of a photon pair (and thus a $\pi\beta$ event). For the calibration they inserted either a liquid

¹ A previous result $\lambda = -1.254 \pm 0.004$ [Ero90] differs significantly

hydrogen target or a CH₂-target close to the π -decay region. Thus they obtained energy scale, conversion efficiency and absolute timing of their apparatus by detecting monoenergetic π^0 s from either SCX or $\pi^+C \rightarrow \pi^0+X$ ($\pi^+C \rightarrow \pi^0+X'$, respectively). Together with the total number of pions which was determined using the averaged counting rate of three monitors they obtained a branching ratio $BR_{\pi\beta}$ of $1.026 \pm 0.039 \cdot 10^{-8}$.

Subsequently, a remeasurement of the pion beta decay with highest precision requires both an intense pion beam and a high detection efficiency. Both can be achieved with the PiBeta detector at PSI. To overcome the problem of the precise determination of the detector efficiency and of the exact pion stop rate a relative measurement was considered. Since the branching ratio of the $\pi^+ \rightarrow e^+ \nu_e$ decay is known to a precision of 0.3% [Cza93] it is an excellent source for a normalization.

For not being restricted by the finite detector size (which would mean low efficiency) a stopped pion experiment is advisable; but due to the main pion decay (see Table 2-3) this results in a large positron background via the $\pi \rightarrow \mu \rightarrow e$ decay chain. The Michel positron background can be well separated with a good energy resolution of the calorimeter since the positron of the decay $\pi^+ \rightarrow e^+ \nu_e$ has an energy of 69.78 MeV while the so-called Michel-decay $\mu^+ \rightarrow e^+ \nu_e \bar{\nu}_\mu$ results in 52.83 MeV positrons at most. (The muon from $\pi^+ \rightarrow \mu^+ \nu_\mu$ cannot leave the target and decays at rest.) Michel positrons can be further suppressed by the long muon decay time of 2.2 μ s, compared to the pion life time of 26 ns. Furthermore additional background from hadronic reaction of the pions with matter (mostly SCX) must be suppressed. This is a) possible through the time structure (hadronic events are prompt) and b) with a plastic scintillator hodoscope.

2.2.2 Experimental Technique

The Pion Beta Decay experiment is being carried out at the $\pi E1$ channel of the Paul Scherrer Institute. Positive pions with a momentum of 116 MeV/c first pass active degrading material before coming to rest in the central part of a plastic scintillator target where they decay with 26 ns mean life time. The decay channels of main interest are the rare pion beta decay, the $\pi^+ \rightarrow e^+ \nu_e$ decay, which is used for the calibration of the decay rate, and the most frequent pion decay $\pi^+ \rightarrow \mu^+ \nu_\mu$. The latter is the major source of background, since the muons of 4.2 MeV are not capable to leave the target and decay with a mean life time of 2.2 μ s into positrons and neutrinos. These positrons are referred to as Michel positrons. For the position sensitive identification of the positrons, they are passing two highly efficient multiwire proportional chambers (MWPC) with low mass and a thin plastic scintillator hodoscope before they enter the calorimeter.

The goal of the Pion Beta Decay experiment is the measurement of the $\pi\beta$ -branching ratio relative to the decay $\pi^+ \rightarrow e^+ \nu_e$ with a precision of 0.5%. This implies, at an external systematical error of 0.4% [Poc95], a statistical error of better than 0.3 % (or 10^5 $\pi\beta$ events). The key considerations for the PiBeta detector were a minimization of the systematical error and a large acceptance for the two decay photons from the π^0 decay, as well as for the positron from the $\pi^+ \rightarrow e^+ \nu_e$ decay.

Then the pion beta decay rate can be obtained by

$$BR_{\pi\beta} = \frac{BR_{\pi e \nu} N_{\pi\beta}}{N_{\pi e \nu} BR_{\pi^0}} \times \text{corrections}.$$

Thus the determination of $\pi\beta$ events relies on the identification of two clearly separated coincident photons from π^0 -decay¹. Due to the low phase space for this three-body-decay the π^0 will only receive low kinetic energy, since the π^+ decays at rest. The photon energy range in dependence of Θ_π which represents the relative angle between photon and pion direction calculates to

¹ The π^0 will decay almost instantaneously with a lifetime of $8.4 \cdot 10^{-17}$ s [PDG98] into a pair of photons

$$65.28 \text{ MeV} < E_\gamma = \frac{m_{\pi^0}}{2} \gamma (1 + \beta \cos(\Theta_\pi)) < 69.77 \text{ MeV}$$

since the maximum kinetic energy T_{\max} of the pion using $\Delta m_\pi = 4.5937 \text{ MeV}$ is at

$$T_{\pi^0, \max} = \frac{\Delta m_\pi^2 - m_e^2}{2m_{\pi^+}} = 0.0746 \text{ MeV}.$$

Here $\beta = \frac{|P_{\pi^0, \max}|}{E_{\pi^0, \max}}$, $\gamma = \frac{1}{\sqrt{1-\beta^2}}$ have been used.

For the participating leptons the allowed range of kinetic energy lies between 0 MeV and 4 MeV. The direction of the two photons deviates at most 3.8° from collinearity¹.

	Process	Branching Ratio
$\Gamma\pi_1$	$\pi^+ \rightarrow \mu^+ \nu_\mu (\gamma)$	0.9998770
$\Gamma\pi_{1\gamma}$	radiative $\Gamma\pi_1$ ($E_\mu < 3.38 \text{ MeV}$)	$1.24 \cdot 10^{-4}$
$\Gamma\pi_2$	$\pi^+ \rightarrow e^+ \nu_e (\gamma)$	$1.230 \cdot 10^{-4}$
$\Gamma\pi_{2\gamma}$	radiative $\Gamma\pi_2$ ($E_\gamma > 21 \text{ MeV}$)	$1.61 \cdot 10^{-7}$
$\Gamma\pi_3$	$\pi^+ \rightarrow e^+ \nu_e e^+ e^-$	$3.2 \cdot 10^{-9}$
$\Gamma\mu_1$	$\mu^+ \rightarrow e^+ \nu_e \bar{\nu}_\mu (\gamma)$	~ 1
$\Gamma\mu_{1\gamma}$	radiative $\Gamma\mu_1$ ($E_\gamma > 10 \text{ MeV}$)	0.014
$\Gamma\mu_2$	$\mu^+ \rightarrow e^+ \nu_e \bar{\nu}_\mu e^+ e^-$	$3.4 \cdot 10^{-5}$

Table 2-3 π and μ decay modes and probabilities taken from [PDG98].

At PSI an intense pion beam with low contamination and high momentum resolution ($\pm 2\%$) is available. The $\pi E1$ beam line at the Paul Scherrer Institute supplies high intensity pion and muon beams up to 10^8 particles per second, depending on the selected momentum between 10 and 500 MeV/c. Beam studies [Ass95] have found the transport of 116 MeV/c particles to be a good compromise of high rate and low e^+ and μ^+ contamination in the π^+ beam. The transport of muons and positrons into the area occurs mostly due to subsequent pion and muon decays at flight. Afore, a 4 mm carbon degrader plate located within the second dipole magnet stopped the protons and sufficiently degraded pions, muons and positrons to enable separation in the downstream dipole magnets due to different deflection angles. A lead collimator at the focal point with 10 mm circular opening finally stops the displaced positrons and muons. This way contamination can be reduced by two orders of magnitude [Bro96]. The focal point then is refocused by a quadrupole triplet over a distance of 3.625 m to the reaction centre. With this, a beam profile of ca. 1 cm r.m.s. diameter and a rate of $2 \cdot 10^6 \pi/s$ can be achieved with a momentum spread of about 2% [Ass95].

¹ The minimal relative angle was obtained using $\left[\text{atan} \left(\frac{\sin(\Theta_\pi)}{\gamma(1+\beta \cos(\Theta_\pi))} \right) + \text{atan} \left(\frac{\sin(\Theta_\pi)}{\gamma(1-\beta \cos(\Theta_\pi))} \right) \right]_{\Theta_\pi=90^\circ}$

2.3 The PiBeta Detector

The signal for a pion beta decay are the two photons from the nearly instantaneous (10^{-16} s) decay of the π^0 , the positron remains in the target. The two photons are exiting the target nearly back-to-back without degradation, passing the MWPCs and the hodoscope and finally are detected in the calorimeter. The $\pi\beta$ -trigger requires two coincident signals with an energy exceeding a threshold of 55 MeV. These signals have to occur in opposing sections of the calorimeter sphere within 20 ns.

A high acceptance for $\pi\beta$ as well as for $\pi^+\rightarrow e^+\nu_e$ can be achieved by a detector that encloses the reaction centre. A detector exclusively filled with sensitive material is capable to detect a major fraction of all photons from the π^0 . The PiBeta detector consists of several parts which are classified into beam counters, electromagnetic calorimeter, charged particle tracker, background shielding and mechanical support.

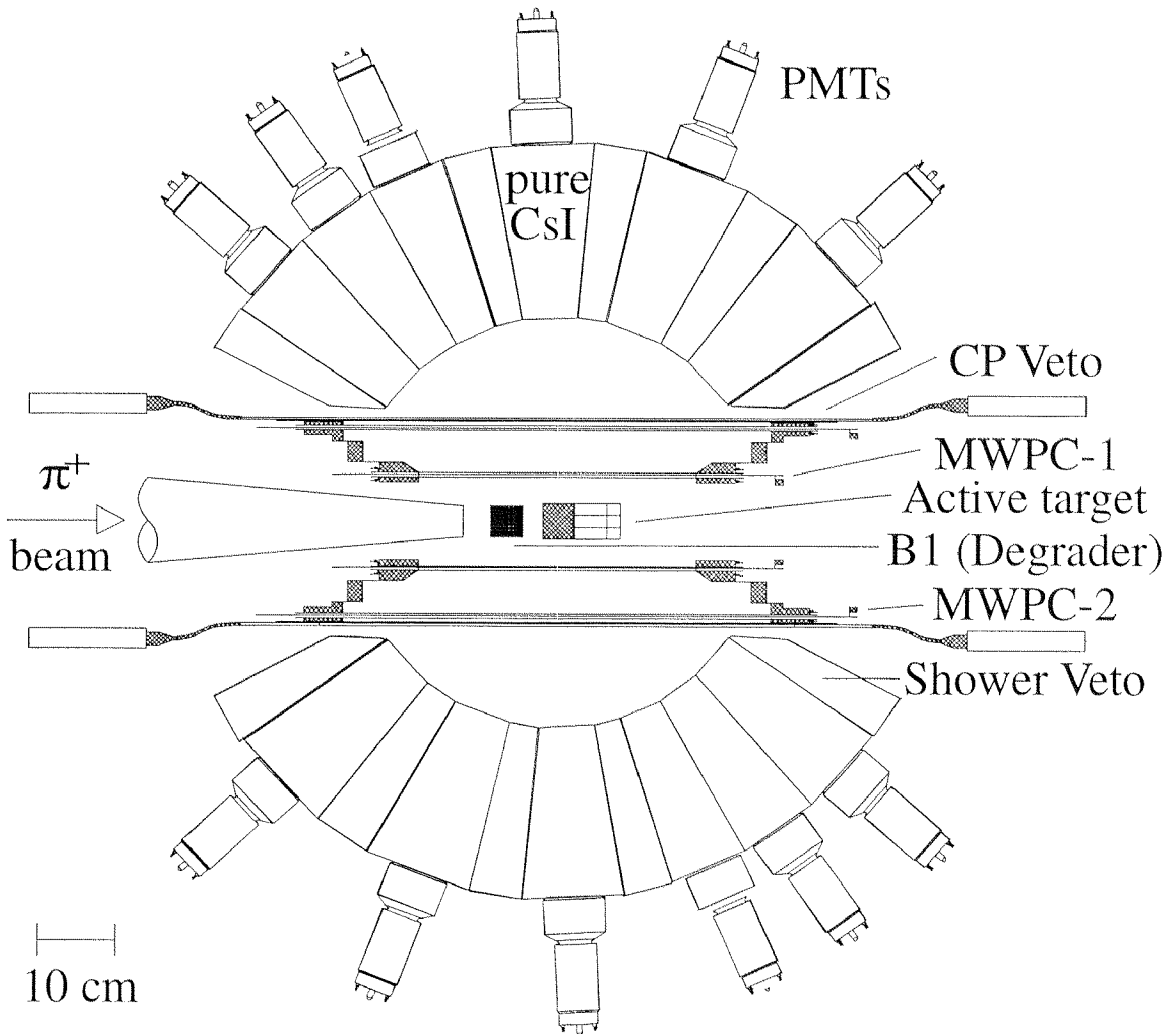


Figure 2-1 Cross section of the PiBeta detector. See text for description.

In the following sections the experimental apparatus will be introduced in more detail starting with the pion beam, followed by the beam counter and target. Then the tracking part and the electromagnetic calorimeter are treated. After the description of mechanical support and outer shielding, the trigger part and data acquisition will be introduced. Background suppression will be discussed continuously throughout the following sections.

2.3.1 Beam Counters and Target

For an additional suppression of beam contamination and to accomplish a well-defined time signal a 1mm plastic scintillator plate is placed in the focal point of the pion beam. The beam counter B0, which is located outside the view of Figure 2-1, is located directly behind the lead collimator after the beam enters the experimental area. An active degrader B1 follows 3.5 m downbeam directly after the evacuated beam pipe. B1 consists of 4 cm thick plastic scintillator which was chosen for an optimum stopping rate within the active target. In coincidence with B0 it identifies a valid pion signal, due to a discrimination against the muon and positron contamination. At 19.6 m total length of the beam line the difference in Time-of-Flight amounts 6 ns between pions and muons and 2.5 ns between pions and positrons. This coincidence - timed with the target signal - is also used to determine the pion stop timing and rate.

The pion stops close to the centre of the 4 cm long cylindrical active target and its decay products are registered. The target consists of 9 elements arranged in three segmented concentric rings and has a total diameter of 4 cm. Each segment is coupled via light guides to 1 cm diameter Hamamatsu 5600 photomultiplier tubes. The same PMT type is used for the read out of the degrader. Energy and timing information therefore is available. The chosen target diameter keeps the conversion probability of the ~68 MeV photons low while it stops the muons of the $\pi^+ \rightarrow \mu^+ \nu_\mu$ whose energy is about 4.2 MeV. The 69 MeV positron from the $\pi^+ \rightarrow e^+ \nu_e$ decay suffers energy loss between 4 MeV and 6.4 MeV, since it has to pass $2/\sin(\theta)$ cm of plastic scintillator material, where θ is the angle between the z-axis (defined by the direction of the beam) and the positron track. The positron from the pion beta decay will stop within the target due to its low kinetic energy.

2.3.2 Charged Particle Tracking Detectors

2.3.2.1 Multiwire Proportional Chambers

In order to identify charged particle tracks and resolve multiple coincidences, primarily of positrons, multiwire proportional chambers (MWPC) are needed. Beside positron tracking for the $\pi^+ \rightarrow e^+ \nu_e$ trigger a high degree suppression of accidental Michel events determines the demand for the MWPCs. They are capable of determine charged particles coordinates to better than 2 mm and achieve an additional suppression factor of $6 \cdot 10^{-3}$ for Michel positrons [Ass95].

An important constraint was a negligible energy loss and a low photon conversion probability. This was achieved by a self supporting structure made of Mylar and Rohacell which results in low specific masses of 36 mg/cm^2 for the inner and 43 mg/cm^2 for the outer chamber.

Two cylindrical MWPCs are surrounding the target located between target and calorimeter. They are located 60.15 mm and 120.1 mm radially from the target centre. The anodes that consist of 192 wires for the inner and 385 for the outer chamber are sandwiched between the cathodes. The anode wires are made from 20 μm diameter gold-plated Tungsten. For both chambers the wire spacing is 1.96 mm. The cathodes of the inner chamber are divided into strips of 3 mm that are wound as a helix with 35° , while the slope of the 2.4 mm wide strips of the outer chamber are at about 44° . The cathode material is aluminium; mylar is used for the electrical insulation. The gas mixture consists of 49.9% argon, 49.9% ethane and 0.2% freon (CBrF_3).

The wire chambers were designed and manufactured at JINR, Dubna (Russia). They have been tested using a ^{90}Sr electron source. An efficiency of 99.9% was measured by inserting a plastic scintillator behind the two wire chambers for normalization. An azimuthal position resolution of 0.2 mm was obtained as well [Kho98].

2.3.2.2 Plastic Scintillator Hodoscope

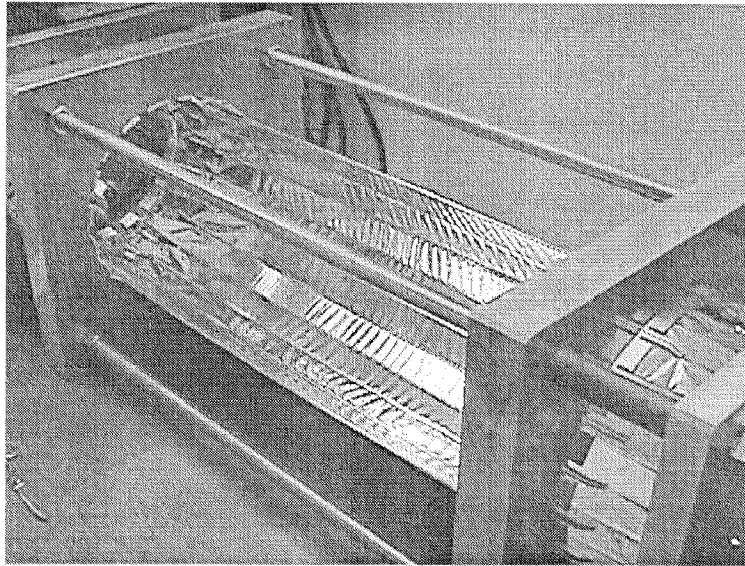


Figure 2-2 Plastic Scintillator Hodoscope strips in a test mounting assembly. The aluminium ring at the right-hand side is designed such that the hodoscope will slide inside the access holes of the calorimeter and will be supported by the steel cones which also carry the detector housing.

For an efficient discrimination of heavy charged particles, minimum ionizing and neutral particles, the MWPCs must be complemented with a plastic scintillator. Its thickness of 3.2 mm is sufficient to identify minimum ionizing particles but still adequate to keep the conversion probability for both photons and positrons low. In this way they can veto charged tracks for the $\pi\beta$ trigger and veto neutral tracks for the $\pi^+\rightarrow e^+\nu_e$ trigger.

The plastic scintillator hodoscope consists of 20 strips with an active length of 600 mm and a thickness of 3.2 mm. They form a regular icosagon that directly encases the outer MWPC. Each of the modules is coupled via light guide at both ends to photomultiplier tubes. The strips are wrapped in aluminized mylar to provide efficient light transport before the readout. The hodoscope has been successfully tested during the calibration beam periods in 1996 and 1997 as can be seen in Figure 2-3.

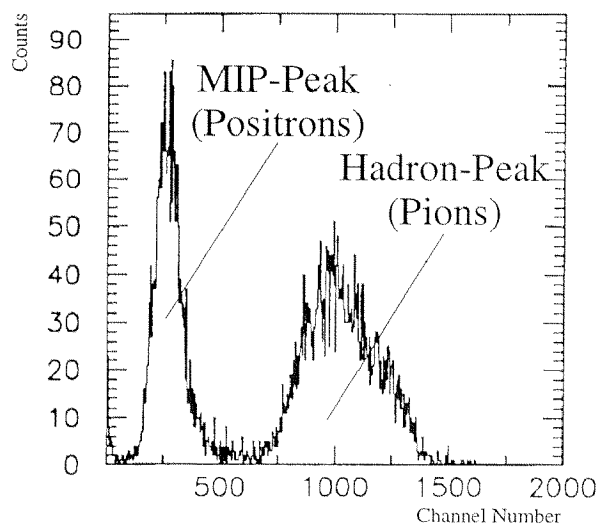


Figure 2-3 Response of one hodoscope strip to positrons and hadrons. The on-line spectrum was obtained by explicitly including prompt events into the trigger. The hodoscope is capable to separate neutral particles (no signal), minimum ionizing particles (narrow peak) and hadronic particles (broad peak), i.e. elastically scattered muons.

2.3.3 Electromagnetic Calorimeter

The calorimeter consists of 240 (pure) CsI crystals. CsI is a fast and rather dense scintillation material with relatively high light yield. Its purpose is the efficient detection of the coincident photons from the π^0 decay, of the positrons from $\pi^+ \rightarrow e^+ \nu_e$, as well as a good energy discrimination of Michel positrons. This requires a good resolution of about 5 MeV FWHM.

The crystals are forming a sphere of 960 mm outer diameter that covers 77% of the 4π sr solid angle. Ten of the 240 crystals, at each side, enclose the beam entrance and its symmetric counterpart. They are used to identify lateral shower losses and therefore referred to as veto crystals. CsI offers a low Molière radius of 3.8 cm and thus small lateral distribution of showers. With a high Z and relatively high density its radiation length, which amounts 1.85 cm, is small and therefore the calorimeter provides a good stopping power for both positrons and photons. Undoped CsI was used due to its fast response time.

Due to the importance of the shower calorimeter its geometry, as well as the properties of the CsI crystals, are described in the following chapter.

2.3.4 Mechanical Support Structure

All the above described components together with cables and electronics are mounted on a common platform. This allows continuous measurements throughout the years under stable conditions since only the entire platform is to be craned in and out the π E1-area. This way also a pre-calibration with cosmic muons of all detector modules can be achieved outside the experimental area.

The calorimeter was designed as a self-supporting structure to exclude non-sensitive material within the calorimeter volume. The sphere is kept together by a spherical steel housing that has holes for the fitting cylinders that surround the PMTs and fix each crystal. The spherical housing itself is attached to two opposing steel cones which are held in place by an enclosing drum seen in Figure 2–4. The steel cones also define the beam entry and access holes and furthermore the lateral support for the veto crystals and thus define an axis of rotation symmetry (see ch. 3).

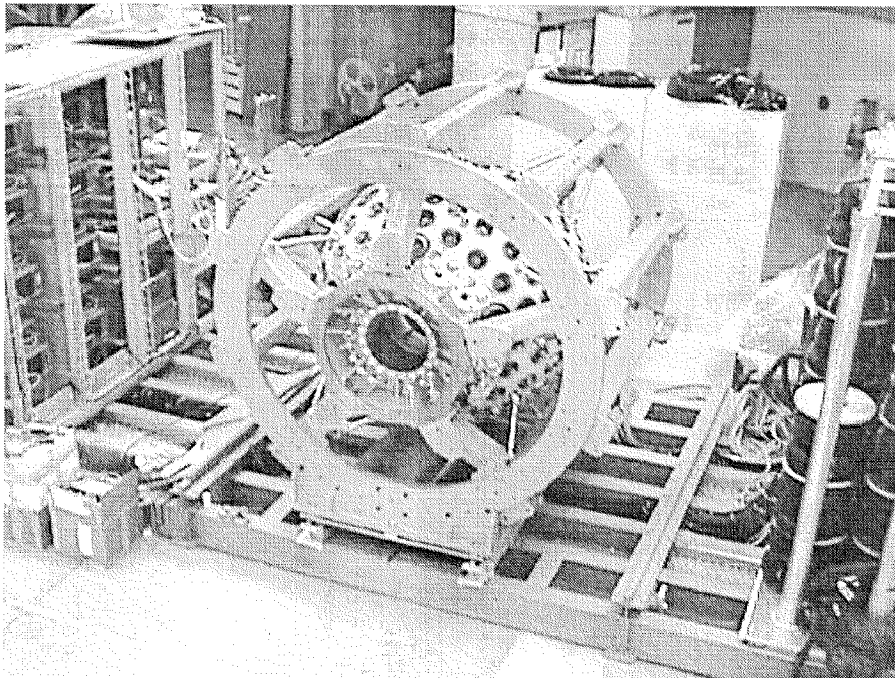


Figure 2–4 The support of the electromagnetic calorimeter on the mounting platform. The sphere holds the calorimeter; thread-rings at the holes above each crystal provides precise radial adjustment applying pressure onto the back of the crystals.

Stable measurement conditions also demand strict temperature control, since the scintillator and the PMT voltage dividers are temperature sensitive. In order to provide stable condition they are surrounded by 4 cm of Styrofoam ('thermal-house'). The thermal-house provides both thermal insulation and light-tightness. A dedicated cooling system which continuously blows cold air into the thermal-house recirculating the heated air (mostly energy dissipated by the PMT bases) in order to keep the temperature stable. In order to keep the humidity low a water cooling device operates close to 0°C. A system of fans and a heater then regulates the temperature to circa 16°.

2.4 Background and Trigger

Before a description of processes and sources of background the layout and nomenclature of the trigger shall be introduced. While discussing the background events, the motivation of the trigger layout should become clear.

Three trigger gates are used for the experiment. Those are the Pion stop gate (P), Delayed Pion Gate (DPG) and DPG'. They are generated using beam counters, degrader and target. The target signal indicates a stopped pion that fires two beam counters. Immediately P is opened for ten nanoseconds, after this DPG is enabled for 80 ns. DPG is followed by DPG' which opens for another 80 ns.

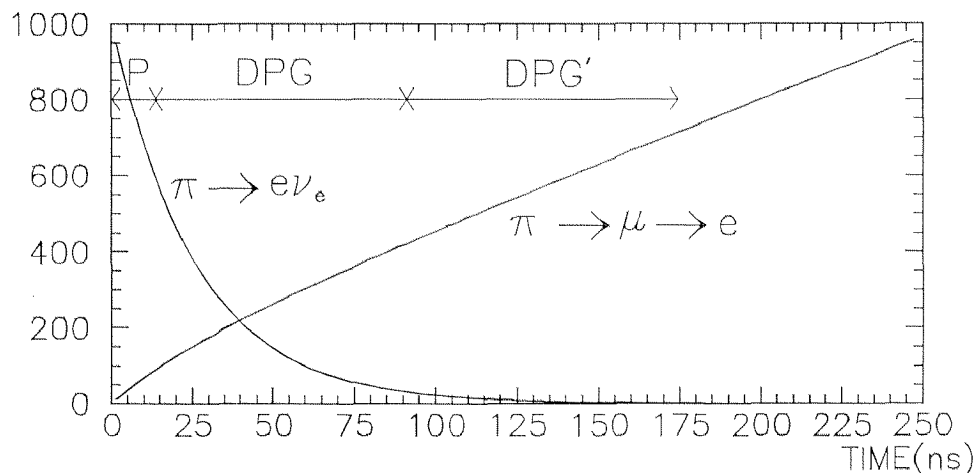


Figure 2-5 Showing pion life time and Michel event decay time and its relevance for the trigger.

For the detection of a $\pi\beta$ event a coincidence of two showers exceeding 55 MeV (the high threshold above the Michel endpoint) in two opposing sectors of the calorimeter is required. In order to generate a fast calorimeter trigger several crystals are combined into clusters. 220 calorimeter modules (without the veto crystals) are located in groups of six to nine crystals. So they are forming 60 overlapping clusters with the outcome that every vertex is contained in at least one cluster. Its applicability has been tested in Geant simulation and works due the fact that in most of the cases a large fraction of energy is contained in a single crystal or around a crystal vertex [Ass95].

The crystals in a cluster are summed using 12 analog adding modules (UVA 125), which have been designed at the University of Virginia. They provide two logical outputs for a high and a low discriminator threshold. Then using LeCroy 4518 Fan In/Out 10 so-called superclusters (SC) are formed by combining the 6 neighbouring clusters that surround the Pentagonal¹ crystals. This is done separately for the low threshold and the high threshold branch. The low threshold branch (SC Lo) will determine the calorimeter's timing, while the high threshold branch (SC Hi) contains the energy information above the Michel endpoint.

¹ see ch. 3. for the definition of the crystal shapes

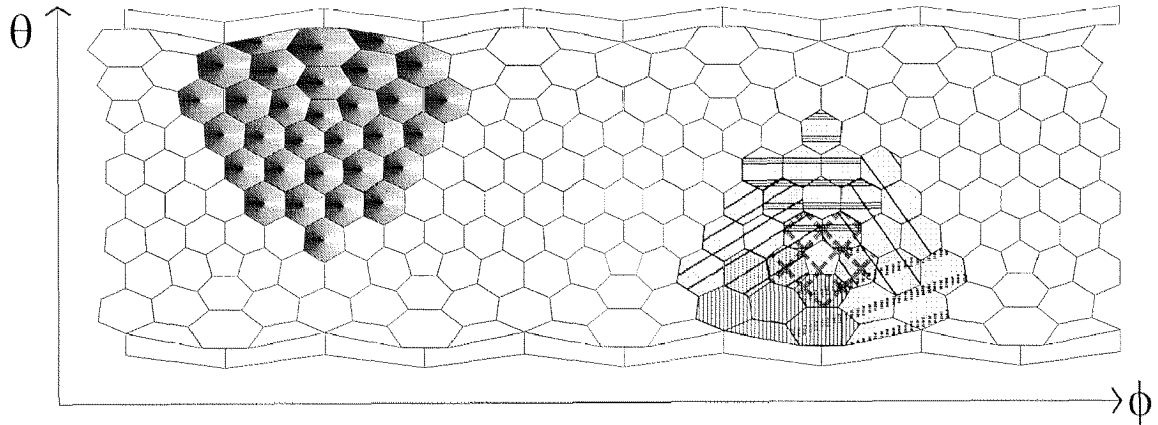


Figure 2-6 PiBeta single event display showing two opposing superclusters and the composition of a supercluster as an 'OR' of six clusters.

A SC Hi signal must be followed within 20 ns by another SC Hi signal from a non-neighboured supercluster during a valid DPG to record a $\pi\beta$ event. For a $\pi^+ \rightarrow e^+ \nu_e$ event one shower exceeding 55 MeV during the DPG is sufficient. The DPG' mainly applies to the Michel decay due to the longer lifetime of a muon with 2.2 μ s. The main processes and background decays are summarized in Table 3.

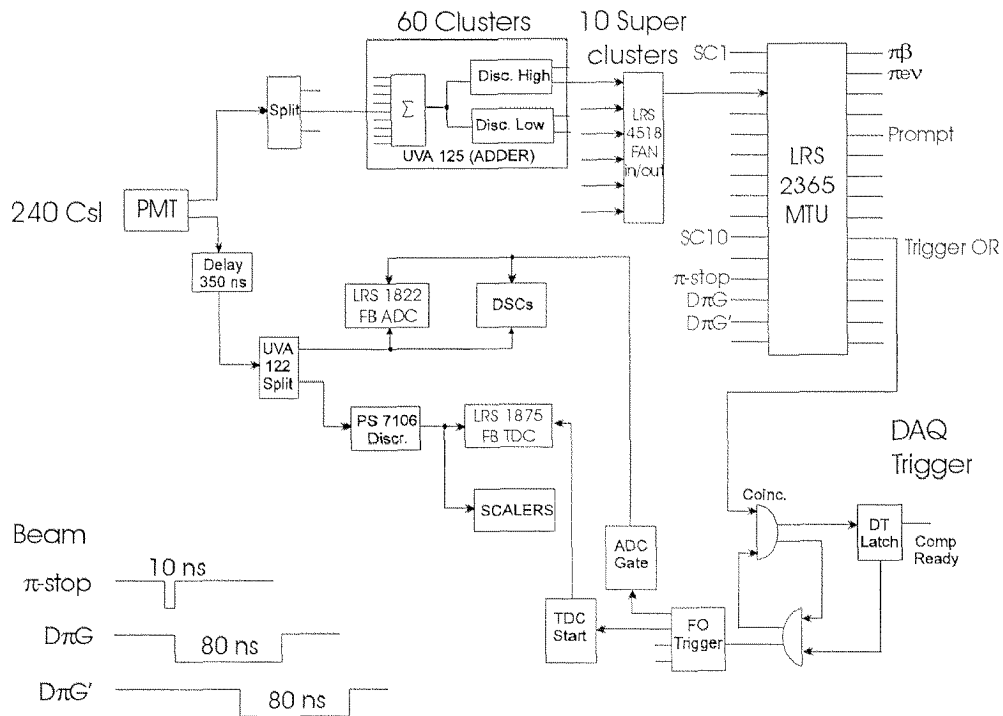


Figure 2-7 Sketch of the detector scheme. For explanation see text.

The inputs from P, DPG, DPG' and 10 SC Hi are generating the desired triggers that are stored in pattern registers. So the $\pi^+ \rightarrow e^+ \nu_e$ trigger, for example, is formed by $SC\ Hi * DPG * \bar{P}$. The logical OR of various event triggers creates a LAM ('Look At Me') signal and supplies the ADC gate as well as the TDC start signal. ADC and TDC analog signals of all connected channels are FASTBUS modules (LeCroy 1822 and 1875) while the logical modules are controlled through CAMAC interface. The master trigger unit (MTU LeCroy 2365) is read by the data acquisition computer using the PSI CAMAC Input/Output controlling unit IO506.

The data acquisition system used in the experiment is the called MIDAS [Rit97]. It provides a platform-independent data acquisition and controlling based on plain C++ code. MIDAS handles all of the on-line analysis, including the digital settings of threshold and delays, slow control (high voltage settings for the PMTs and temperature control for example) data readout and storing on mass storage devices. The same system provides the tools for off-line analysis, since it can be used with the PAW [PAW96] analysis tool including the generation of user specified n-tuples.

The actual values of all detector channels are read when the MTU signalizes the desired trigger pattern. Data in binary format can be stored simultaneously on tape and harddisk. Further information for an ongoing run such as time, temperatures, applied PMT high voltages, pedestal values, thresholds, etc. are stored in a database. The database entries are recorded at the beginning and the end of each run in the data file.

Due to the low decay rate all background processes must be well under control. The background mainly comes from the $\pi \rightarrow \mu \rightarrow e$ decay chain resulting in positron energies of $m_\mu/2$ at maximum - known as Michel positrons. Thus, a clear discrimination from $\pi\beta$ - and $\pi^+ \rightarrow e^+ \nu_e$ -events is possible. A high energy threshold in the UVA 125 adder of 55 MeV will take care of most of it. The low threshold branch is dedicated for background studies and appropriately prescaled.

An important source of background for the $\pi\beta$ signal are 4-fold accidental coincidences of Michel-events and $\pi^+ \rightarrow e^+ \nu_e \gamma$, since both are capable to exceed the high threshold level of 55 MeV. A highly efficient charged particle tracking is capable to identify this type of Michel background. The positron identification is done with the MWPCs which resolves double tracks. The hodoscope, on the other hand, can suppress the background from radiative decays by a cut on neutral particles (see Figure 2-3).

The $\pi^+ \rightarrow e^+ \nu_e$ trigger is more susceptible to be accidental background, since the presence of only a single shower within DPG is required. Besides cuts in off-line analysis a background pile-up rejection will be applied. With the fast digitization of all CsI pulses accidental coincidences can be suppressed. The applicability of this so-called 'domino sampling chip' has been successfully tested [Bro96].

An additional source of background appears due to interaction of beam pions with target and degrader material resulting in hadronic particles. Neutral, as well as charged ejectiles, are suppressed by vetoing on the prompt gate.

This also applies for single charge exchange (SCX) in the degrader which would result into a π^0 background at $6 \cdot 10^{-6}$ level. A 10 ns delay of the PG can rule out entirely the π^0 emanating from SCX in the degrader. This was demonstrated in the 1994 beamtime [Ass95, Bro96].

The thermal-house will be surrounded with 5 cm thick lead bricks to inhibit ambient background to enter the calorimeter. In order to reject cosmic muon initiated showers - besides a clean pion stop trigger- large plastic scintillator paddles roofs the lead-house. The logical OR of the paddles will also be fed into the master trigger in order to act as a veto. The lead house is needed to prevent self vetoing by particles escaping the calorimeter, such as soft photons, electrons or positrons. In addition the suppression of ambient background, mostly neutron induced reactions inside the experimental area, is valuable.

2.5 Determination of the Rate

Since the PiBeta detector is designed for similar response to both positrons and photons of about 70 MeV the determination of the pion beta decay rate via the $\pi^+ \rightarrow e^+ \nu_e$ rate can be written straightforwardly as

$$\Gamma_{\pi\beta} = \frac{BR_{\pi\beta}}{\tau_\pi} = \frac{1}{\tau_\pi} \frac{BR_{\pi \rightarrow e\nu} \times N_{\pi\beta}}{N_{\pi \rightarrow e\nu} \times BR_{\pi \rightarrow \gamma\gamma}} \times \text{corrections}.$$

The corrections comprise several sources of inefficiencies for the number of counts as there are:

- Differences in the acceptances of the shower detector, particularly close to the veto crystals (see Figure 4–3). This effect has three sources, the first comes from a different shower profile, since positrons start to shower earlier, the second is due to missing photons in the π^0 decay, since they are not emitted collinear and the third is caused by scattering of the $\pi^+ \rightarrow e^+ \nu_e$ positron within the target.
- Self-vetoing due to backsplashing shower particles. Here also a photon induced shower could generate a signal in the plastic veto hodoscope when charged particles from the shower are leaving the calorimeter through the front face. This would result in vetoing a valid event.
- Positron annihilation before entering the calorimeter can occur in the target, in the hodoscope and in air. Bremsstrahlung of the positron could lead to a misinterpretation of the event, as well as photon conversion in the target or in the hodoscope.
- Instrumental inefficiencies of the MWPCs and the hodoscope.
- Missing events can be caused due to photons traversing the calorimeter without undergoing an interaction. Positrons, as well as the photons, can leak through gaps between crystal modules. Thus, precise dimensions for the modules are crucial and only a thin crystal wrapping was considered. The achieved alignment precision during the final assembly was in the order of 0.2 mm.

The main contribution to the systematical error is the current accuracy of the $\pi^+ \rightarrow e^+ \nu_e$ BR measurement, which is of 0.3%. Together with the above mentioned uncertainties, the systematical error is estimated to be in the range of 0.5%. In order to keep the statistical error comparably low $1 \cdot 10^7$ s of beam time at a rate of $2 \cdot 10^6$ stopped pions will be necessary.

3. The Electromagnetic CsI Calorimeter

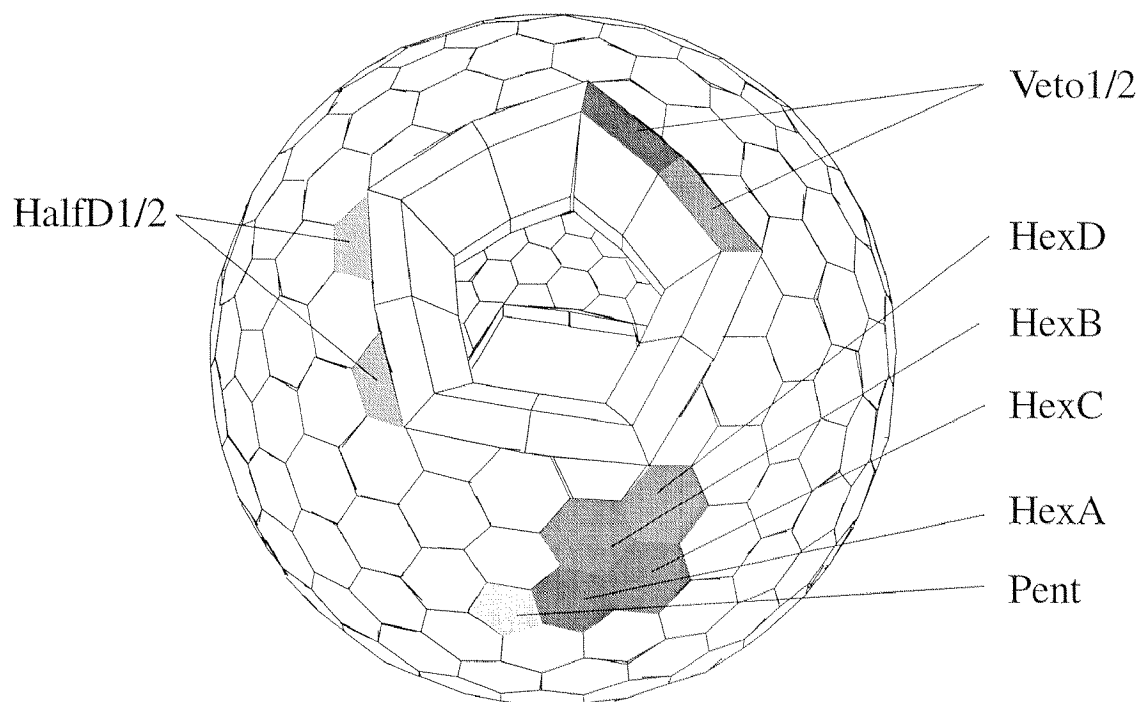


Figure 3-1 Layout of the spherical CsI calorimeter. The different shades of grey indicate the 9 occurring crystal shapes. These are Pentagon (10), HexA (50), HexB (50), HexC (50), HexD (40), HalfDs (10 each) and Vetoes (10 each) - making a total of 240 crystals. .

The calorimeter must provide good energy and angular resolution as well as high stopping power for both ~ 70 MeV photons and positrons. Furthermore a fast response and reasonable costs are required. This was achieved by using 240 pure CsI crystals with a length of 22 cm corresponding to 12 radiation lengths. They are forming a partial sphere that covers 77% of the full 4π sr solid angle. The calorimeter was designed using a class II geodesic breakdown of an icosahedron [Ass95].

Thus, the sphere is approximated by 60 triangles (or 12 pentagons, respectively) which leads to a repeating structure at $\phi_n = 36^\circ + (n-1) \cdot 72^\circ$ for one hemisphere and $180^\circ - \phi_n$ for the other (compare with Figure 2-6). At the poles two pentagons were omitted for beam entrance and readout access. Instead, ten flat crystals on either side act as a veto for shower losses and beam particles. The remaining ten pentagons (plus overlapping crystals) act as superclusters for the trigger that is sensitive to two photons in opposite arrays of the sphere.

In order to reach high granularity - and hence provide a good angular resolution - each of these basic triangles consists of 4 1/5 crystals. Due to the curvature of these basic triangles we end up with 4 types of full and two of half hexagonal truncated pyramids, one pentagonal pyramid and two different veto crystals.

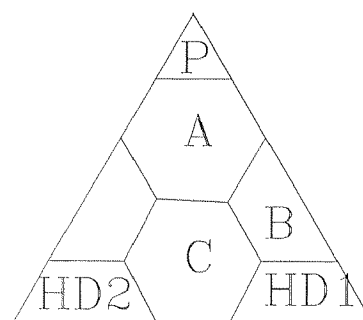


Figure 3-2 One of 60 basic triangles forming the calorimeter sphere. It is showing a fifth of the PENT, two halves of the HEX B and furthermore a HD1 plus a HD2 would form a HEX D.

3.1 Properties of CsI

Asking for a fast and dense scintillating material with relatively high light yield, pure CsI was the only choice. It shows two main emission components. One in the near UV region at 310 nm and one at 460nm (the properties of CsI are summarized in Table 3-1). In comparison to BaF₂, CsI provides a better suited wavelength for PMT readout and a shorter radiation length. BGO is not suitable because of its long decay time of ~240 ns. Such a slow calorimeter response would lead to multiple coincidences and reduced energy resolution due to pile up, since i) the pion decay time is faster by an order of magnitude and ii) the time structure of the accelerator is 19.75 ns.

Density	4.51 g /cm ³
Radiation length X_0	1.85 cm
Molière radius R_M	3.8 cm
Atomic Number Z	55, 53
Peak wavelength	310 nm / 460 nm
Refractive Index (@ 310 nm)	1.95
Decay time (fast/slow)	~15 ns / ~ 1 μ s
Lightyield (fast component)	~ 100 Photoel./MeV
Temperature Coefficient	-1.5%/K
Hygroscopic	slightly

Table 3-1 Properties of (pure) CsI; compare with Phys. Rev. D50 (1994) 1261 and Figure 3-5.

The drawbacks of CsI are a high temperature gradient of -1.5%/K and a slight hygroscopicity. Both properties require a temperature and climate controlled surrounding for the calorimeter. This is necessary, anyhow, to provide stable working conditions for the voltage dividers of the photomultiplier tubes.

A short radiation length provides compactness due to a high stopping power for both positrons and photons. This especially is valid for higher energies (>10 MeV), when the positron, or electron respectively, loses energy by bremsstrahlung rather than by ionization which initiates electromagnetic showers¹.

Photons and positrons (or electrons, respectively) passing matter are losing energy mostly due to electromagnetic processes. Photons may undergo Compton scattering, produce photoelectrons or create electron-positron pairs depending on the energy. Positrons can ionize, emit bremsstrahlung or annihilate with an electron. The cross section for these individual processes depends on the particle energy, as well as the density and the atomic number of the material. Figure 3-3 shows the energy dependence of processes responsible for the energy loss of photons.

¹ see section 7.4 for a more detailed discussion

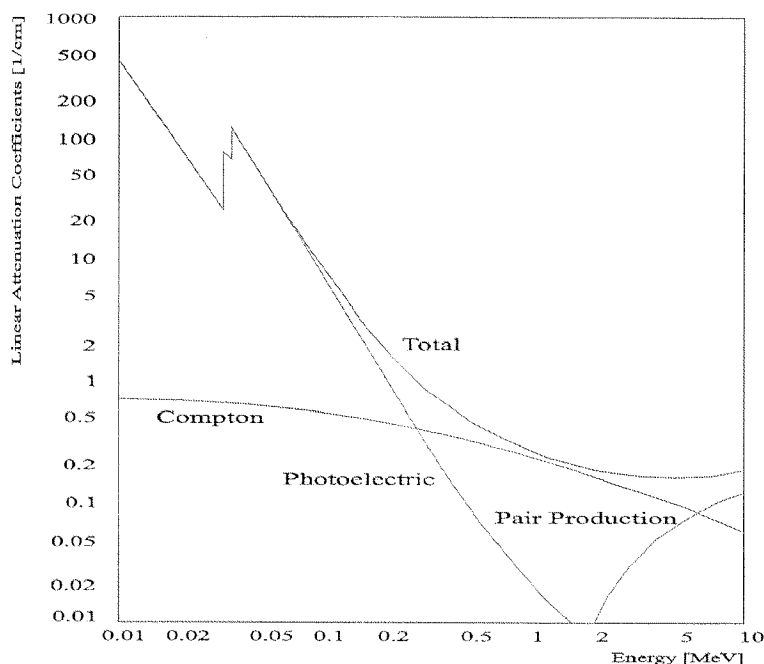


Figure 3-3 Linear Attenuation Coefficient of CsI as a function of photon energy. At larger energies (beyond the scale of this figure), where the pair production process is dominating, the energy loss of photons and electrons is similar.

For energies much higher than the pair energy (1.022 MeV), pair production is the dominant process. At those energies the daughter particles will again be able to undergo the above mentioned electromagnetic processes. In this way an electromagnetic shower emerges. Such a shower can be characterized using the position of the shower maximum and the average shower width. In average a shower appears to be a cone; but can also have extreme distributions, i.e. when a daughter particle traverses several crystals without interactions and consequently deposit energy in a remote crystal. Some examples of these untypical distributions are shown in Figure 3-4.

Due to multiple scattering of shower particles there is also a notable lateral energy deposition. This distribution scales well with the Molière radius. In order to avoid intercalibration effects due to the summing over several crystals and to keep the energy loss low, a small Molière radius is desired.

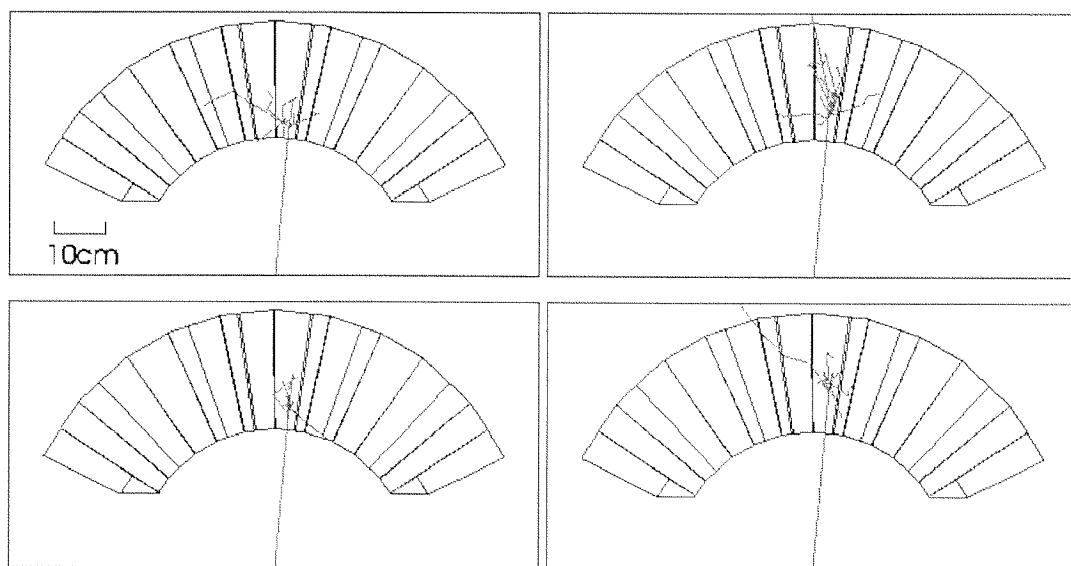


Figure 3-4 Untypical shower distributions of 50 MeV photons impinging the CsI calorimeter

3.1.1 The Scintillation Process of Alkalihalides

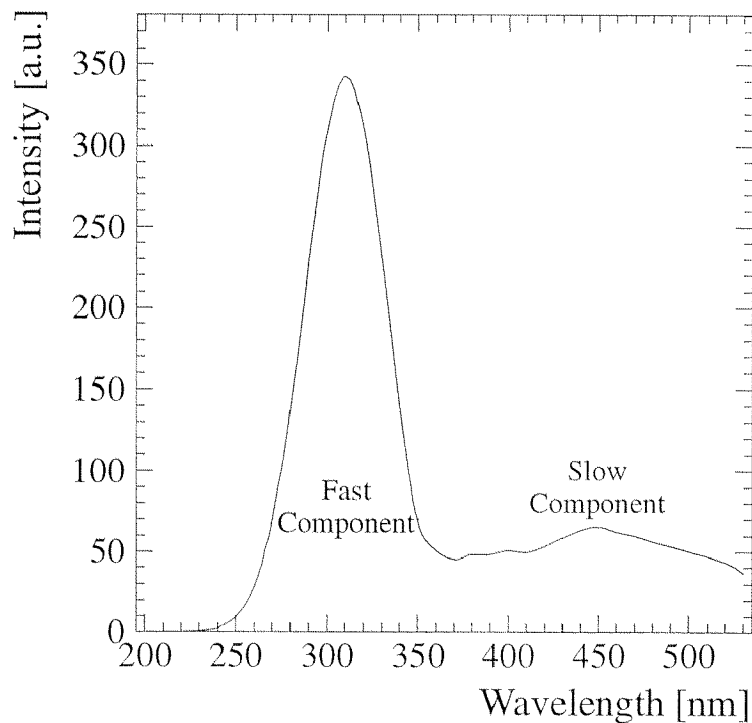


Figure 3-5 Light Emission Spectrum of (pure) CsI.

Interactions of ionizing radiation with matter lead (to a certain extent) to the excitation of electrons into higher energy states or to the creation of electron-hole pairs, respectively. The radiative deexcitation is characterized by the emission of photons whose wavelengths correspond to the energy of the excited state since $E=h\nu$. Only few materials show the emission of visible - or better: detectable - light, the so called luminescence. (NaI is capable to reemit 7% of the energy of the ionizing radiation as light [Bir64].) The number of generated photons in principle is proportional to the energy loss of an ionizing particle traversing a scintillating material. Important and widely used inorganic scintillators are alkali halides like NaI, CsI and BaF that often are doped with activators (e.g. Thallium) in order to yield a high light output. Unfortunately these activators act as electron traps and thus delay the emission of light. Most fast scintillators on the other hand normally show low light output and emit light in the UV-region. For pure alkali halides (of which NaI and CsI are the most common and best studied) there are three possible processes that can result in luminescence. One is caused by defects of the crystal structure that can act as traps for bound electron-hole pairs (excitons). The deexcitation, in general, happens within a few nanoseconds and can be non-radiative or radiative [Enz58]. The latter case is considered to be responsible for the fast decay component in the near UV. A competing effect resulting in fast scintillation light is the so called Crossluminescence [Jan87]. It is caused by radiative transitions of the electrons between valence band $\Gamma(5p)^6$ and upper core band $\text{Cs}^{2+}(5p)^5$ [Kub88]. But, having the valence band width (2.4 ± 0.3 eV) subtracted from the difference of threshold energies (7.6 ± 0.4 eV) [Smi75], the maximum wavelength for CsI crossluminescence would be at $240(+35)$ nm. However, Jansons et al. suspect Auger transitions to be responsible for the absence of a fast UV crossluminescence light in CsI [Jan87].

Another component emerges when electrons are temporary bound within Γ^- vacancies; these vacancies presumably occur because of an O_2 content replacing Γ^- -Ions during the growing process [Kub88]. Since this is a stronger metastable state it results in the slow emission of visible light that is responsible for the slow component. It was found by Hamada et al. [Ham95] that this component (in the case of CsI) slowly disappears with time and can be suppressed by moderate heat treatment, although there was a growing

enhancement of the slow component for higher temperatures starting at 150°C. This way they could conclude that intrinsic vacancies are the source for the slow component. (Section 3.2.3 will be dedicated to the ratio of the slow luminescence component to the fast luminescence component.)

3.2 Crystal Inspections

The CsI crystals were grown, cut and polished by AMCRYS-H in Kharkow, Ukraine from raw Material delivered by Metallgesellschaft, Frankfurt/M. and from Novosibirsk, Russia. After first tests concerning the specifications for the individual CsI crystal the steady process of delivery, check-ups and preparation started. To this end a set of standard procedures has been established at PSI for a critical inspection of each delivered crystal.

This quality control guaranteed not only good performance of the final calorimeter in all sections but also provided information of light output and optical uniformity that could already be used in the GEANT simulations.

The crystal tests can be classified in

- 1) Visual inspection
- 2) Check of dimensional tolerances
- 3) Measurement of the light yield ratio of the two emission components
- 4) Optical uniformity determination
- 5) Light yield measurement.

(Between steps 3) and 4) the crystals were coated and wrapped.)

3.2.1 Visual Inspection

Due to the hygroscopy and softness of CsI the shipping was quite delicate. Thus, a very basic check for cracks, optical irregularities and shipping damage was performed first.

3.2.2 Distance Measurement

Since the calorimeter's construction principle relies on a self-supporting structure comparable to a Roman arch a dimension precision in the order of tenth of a millimetre for each module is indispensable. Larger discrepancies would cause air gaps, deviations from the optimal shape and a poor or impossible mechanical fit; as a result the acceptance correction would result into a higher systematic error. The distance measurements to determine the dimensional accuracy of the crystals were performed at PSI using the computer controlled 3-Coordinate-Measuring-Machine from WENZEL Precision. It allows the determination of positions with a precision of 7 μm . The touch head of the machine was programmed to automatically scan the surface of a crystal; for each plane 6 points were scanned. The angles between the planes are obtained, the vertices of the crystal were calculated which then could be compared with the specified values. A maximum deviation of 0.3 mm for a vertex and an angular offset of 0.08° for opposite sides was tolerated.

3.2.3 Ratio of Fast Emission to Total Light Yield

The ratio of the two main contributions to the light emission spectrum of pure CsI was measured as a test for the fabrication quality. The slow emission component is generated by I⁻ vacancies, say crystal defects. Hence, high-purity raw material with exact stoichiometry, as well as a controlled and clean

growing process minimized the contribution of this component. The ratio of the fast emission component to the total emission (F/T ratio) therefore indicates the 'goodness' of the crystal and provided quality control for the growing process.

For the measurements, which are performed under similar conditions for each crystal, the bare crystal was air-coupled to a 3" EMI 9822QB photomultiplier. The response signal obtained with cosmic muons was fed into the Flash ADC of a digital scope (Hewlett Packard TDS 740), where two gate integrals were defined, a 100 ns long one (F) which would contain the fast component and a 1000 ns wide one (T) to obtain the overall yield. A personal computer using the built-in IEEE488 bus read out and analyzed the data. Along with the individual spectra, the ratio of charge collected during the two gating times was histogrammed and the mean value of that histogram gave the F/T ratio. After ca. 10 minutes of measuring time a sample of 1000 raw pulses was obtained. Since the contribution of the slow component should be low to allow a good timing resolution and to avoid pileup, the ratio of the fast component to the total light yield was required to exceed 70%.

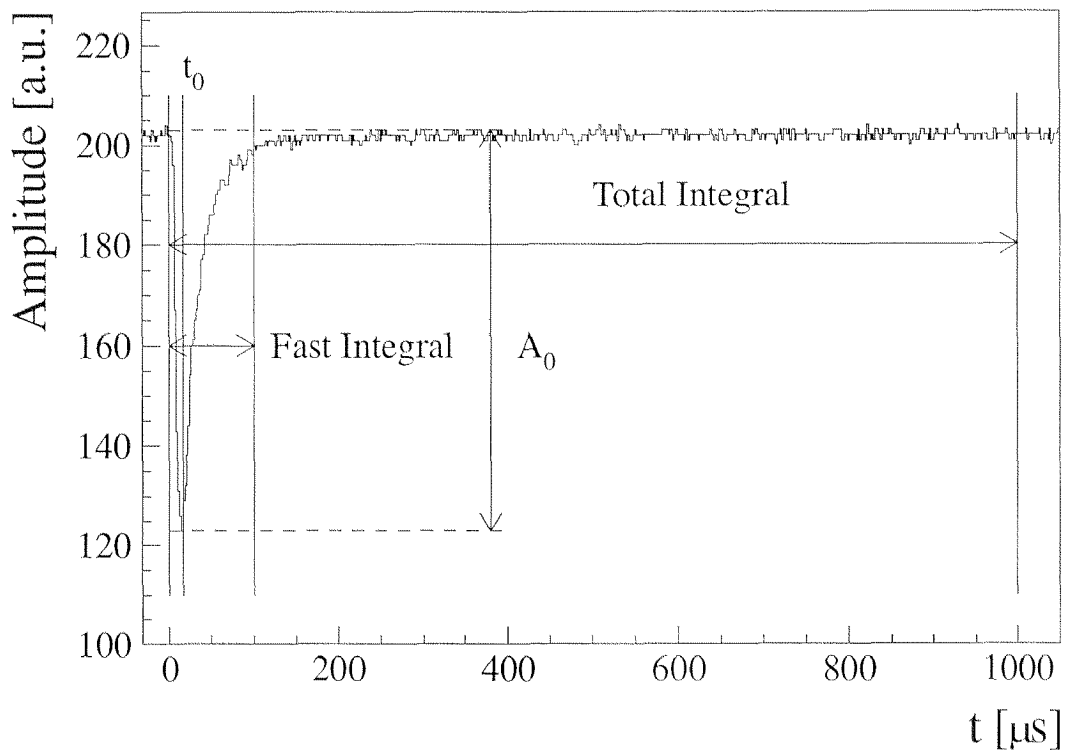


Figure 3-6 Response function of a CsI Scintillator under test obtained with a digital oscilloscope. The charge integration gates are also shown. The ratio of the collected charges then gives the F/T-ratio.

After some difficulties in the beginning of the delivery process we were supplied with CsI crystals showing an average F/T close to 80% thanks to better raw material and improved growing conditions.

3.2.4 Optical Non-uniformity and Light Yield

Crucial for a precise measurement of the pion beta decay rate is a good separation of twofold Michel coincidences and $\pi\beta$ events through their energies. Therefore a good energy resolution and a low tail due to missing energy and thus high light yield and good optical uniformity are required. An electromagnetic shower which develops in average within the first 10 cm of a crystal will deposit variable energy at different depth of the calorimeter material. Any variation of the calorimeter response over the depth will contribute to an over- or underestimated- integrated energy and thus result in a broader peak. The energy resolution σ_E/E of an electromagnetic calorimeter can be parametrized as

$$\frac{A}{E} \oplus \frac{B}{\sqrt{E}} \oplus C \quad (3.a),$$

where \oplus indicates a squared sum. Here A is the noise term, B the stochastic term and C the constant term. The optical non-uniformity directly contributes to C since it can be interpreted in a similar way as a gain difference in neighbouring crystals. Assuming a conical distribution of the electromagnetic shower with depth r and defining φ to represent the opening angle of the shower cone, the integrated shower energy S is

$$\iint_{r \varphi} N_{ph}(r, \varphi) dr d\varphi$$

with N_{ph} representing the distribution of photoelectrons/MeV within the calorimeter. Consequently the longitudinal and radial variation due to optical non-uniformity and gain variation σ_c is

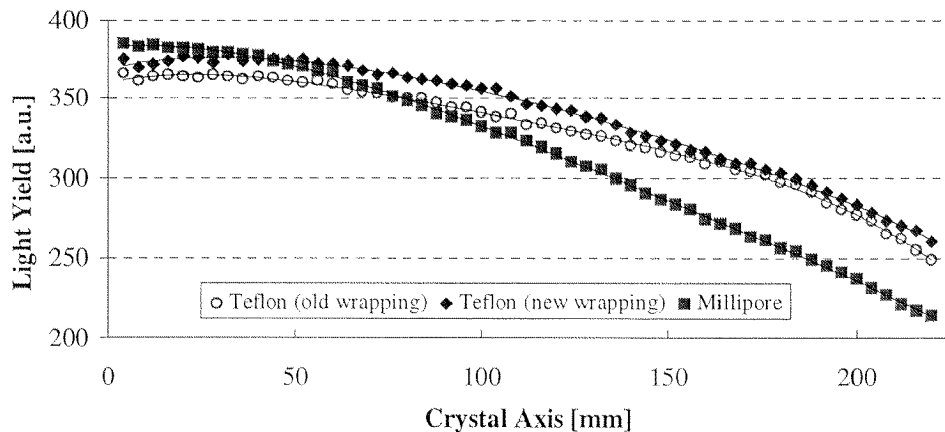
$$\sigma_c = \frac{d^2 S}{dr d\varphi} = N_{ph}(r, \varphi)$$

and thus $\sigma_c/E = N_{ph}/E = \text{constant} = C_1$.

Tapered crystals are likely to have a position dependence in their light output. This started a series of investigation to minimize the influence of the non-uniformity without degradation of the light yield, which will be introduced in the following section. The required uniformity had to be better than 0.3%/cm for the first half of the crystal. (Since the shower mean of 70 MeV positrons or photons lies within the first third of the crystal length, the second half (nearby the read out) is of lesser importance.)

3.2.4.1 Wrapping Material

In addition to intrinsic properties of the crystal and its shape also the surface treatment determines the optical properties of a detector module. Light output and optical uniformity are mainly influenced by the surface treatment and the wrapping material. Since we deal with truncated crystals, light that emerges close to the front face¹ is being focused towards the PMT; this simply is understandable in terms of the reflection law. On the contrary, light generated closer to the rear face partly has to travel nearly two times the crystal length and, therefore, will suffer losses (which for example can be seen in Figure 3–7). This leads to a variation of the light yield as a function of the crystal length that is summarized by the term (optical) non-uniformity.



¹ Front face means the side of the crystal pointing towards the target in the final assembly. This side is opposite to the side which is read out by PMT (later called rear face).

Figure 3–7 Comparison of common reflecting materials. Each data point represents the evaluated light yield for a registered path of beam pions perpendicularly the CsI crystal. Since the measurement conditions were identical for all wrapping samples, no pathlength correction was applied for the sake of simplicity. (The position of the PMT is on the right hand side.) The diamonds show the response for a Teflon wrapping where also an existing wrapping (open circles) was replaced by a new wrapping of same thickness. The slight degradation is the effect of abrasion that causes a decreasing transparency of the material, i.e. due to pressure. However, it still was superior to the Millipore wrapping (filled squares).

In order to overcome non-uniformity, a number of surface treatments of the front side and additionally a variation of reflecting materials has been investigated. The non-uniformity sufficiently was reduced by placing a black paper onto the front side, which still allows total reflection at this side due to an air gap, but which will absorb all the light leaving the crystal through the front face.

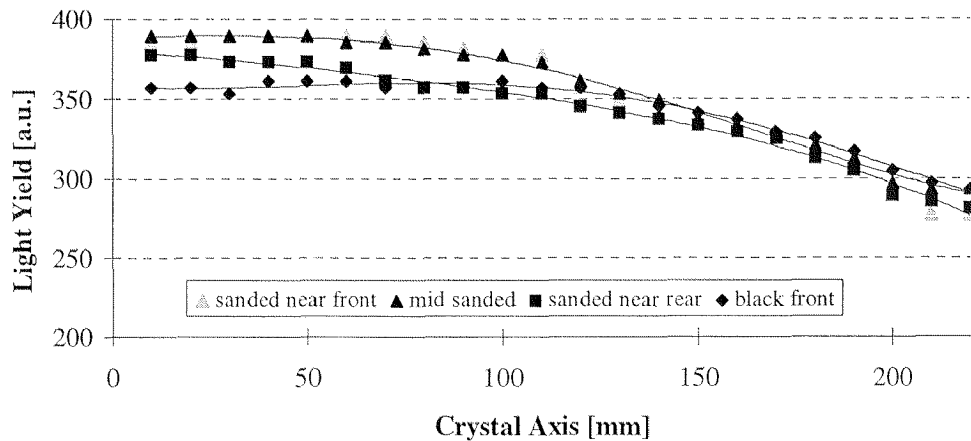


Figure 3–8 Influence of uniformity from treatment of the front side. (In all cases the crystal was wrapped in Teflon foil.) In order to achieve a uniform response, after choosing the optimal wrapping material, sections with enhanced light output have to be reduced. Consequently partial light absorption by sanding or by applying an opaque material can not be avoided. The insertion of a black paper that would still allow total reflection at the crystal surface was superior to sanding and provided an uniform light response within the first 10 cm of the crystal.

Since the reflectivity of the wrapping material is a function of wavelength several standard materials as PTFE¹-Foil (Teflon), Millipore[®], Tyvek[®] and aluminized Mylar have been tested. The first three materials are diffuse reflectors which mean that they obey the (2nd) Lambert law², while aluminized mylar acts as a mirror.

- Teflon, originally developed by DuPont, is an inert PTFE foam. The foaming process gives PTFE a white colour and hence good reflective properties. It is widely available in several thicknesses and sizes. For this test 50 µm thick PTFE-foil was used.
- Millipore Membranes are fabricated for the use in biological and chemical laboratories as filter sheets. They consist of polyvinylidene fluoride (PVDF) and are available in different varieties with a standard thickness of 110 µm. Their reflection properties have been investigated for some years [Bir93], but main disadvantage are the high costs.
- Tyvek, from DuPont, has the advantage of low cost at a good reflectivity. However, it is lacking opaqueness and normally has a thickness of 250 µm.

The development process was carried out in two stages. Firstly, two rectangular CsI crystals of the same manufacture as for our specific crystals have been wrapped with the same material at a time to account

¹ PolyTetraFlourEthylene

² If the rays meet the surface at an angle, then the illuminance is proportional to the cosine of this angle with the normal.

for systematic imperfections. An UV-sensitive PMT was coupled with an airgap to the crystals. Then the light yield was determined by the response to cosmic muons.

As a result of this test two materials were excluded from further examinations. From experience a diffuse reflector is better suited for a bulky and truncated scintillator [Der82,Bir93]. As expected, the wrapping with aluminized mylar showed the lowest light yield. Due to a low opaqueness and probably a low reflectivity in the UV-region the Tyvek wrapping did not lead to promising results. A treatment of Tyvek with reflecting paint (Kodak White Reflectance Coating 6080), which offers a reflectivity of more than 95% for UV light, could not improve the light yield notably. Also the use of painted Mylar was considered; but it was not applicable for wrapping any more after drying.

In the second step also the non-uniformity of the light output was measured. This was realized at a test set-up at the π M1 beam line at PSI with 80 MeV protons. A three inch EMI 9822QKB phototube has been coupled to the crystal using an adhesive silicon rubber (DowCorning 6500). The crystal to probe was put in a light tight and temperature controlled box that was located behind two quadratic wire chambers. By this the light yield and the point of incidence were obtained simultaneously. For this evaluation only the portion of light that was collected during the first 100 ns was taken into account.

Different shapes of the CsI crystals have been used for the evaluation of the wrapping material to account for the geometric influence to the light collection. Two kinds of Durapore sheets and different wrapping thicknesses of Teflon have been investigated. After this, some methods to reduce optical non-uniformity have been compared (see Figure 3–8).

Two layers of properly wrapped Teflon-foil provided higher light output than one layer of Millipore, which had a comparable thickness. This was demonstrated for several crystals (one typical example is shown in Figure 3–7). Nevertheless, Bird et al.[Bir93] found Millipore to be superior to Teflon, since he obtained a better energy resolution for CsI(Tl) crystals. Although Millipore (in this study) showed better results for a sample of pure CsI with a large (>50%) contribution of the slow emission component, Teflon seems to have better reflecting properties for UV-light. This is decisive since pure CsI has the main emission component peaking at 310 nm.

As a result two layers of Teflon foil finally suited best the requirements of reflecting properties, optical uniformity and reasonable costs. Also a minimization of inactive material between the crystals was achieved this way. The Teflon layers were surrounded by one layer of aluminized mylar foil that both optically ‘seals’ the crystal and protects the Teflon foil from dirt and damage.

3.2.4.2 Crystal Coating

It is known that CsI is a slightly hygroscopic material and emits wavelength scintillation light with a main component in the near UV at 310 nm. Both led to the idea of using an additional surface treatment. A lacquer that does both, seals the crystal for moisture in air and improves the reflecting properties was required. There already existed some expertise for Teflon AF[®] which applies a thin transparent water-nonpermeable coating on the CsI surface [Wus96].

In order to provide reproducibility a 2'' PMT (Philips XP2020Q) was permanently coupled to the test-crystal. After gluing the PMT to the crystal the coat was applied by dipping the crystal into the solvent that dried after a few hours. To avoid PMT damage the suggested ‘baking’ of the lacquer was avoided; thus the coating did not stick perfectly onto the surface and could easily be removed for cross-checking. Nevertheless a uniform film of ~10 μ m coating on the CsI could be applied that way. The light output of this crystal was measured with different wrapping materials, with and without coating using both cosmic muons and a pion beam. In either case the light output did slightly decrease after applying the coating. This idea of coating therefore was not followed any more until a Ukrainian group came up with a lacquer where a wavelengthshifter (WLS) was added to the coating material. So a set of crystals (one of each type) was chosen to demonstrate the properties of the lacquer. They were investigated in the RASTA apparatus (see ch. 3.3.4.3) for light yield, uniformity and timing before and after painting. In order to obtain the timing resolution the crystal was sitting between two 9.5 mm thick plastic scintillators. The signals from the plastic scintillator were used for the TDC start, which was stopped by the CsI signal. The standard deviation of the timing distribution then determined the timing resolution.

Before and after painting the value was between 0.5 and 0.6 ns. So one could conclude that the WLS in the lacquer does not degrade the overall collecting time of light within the crystal. For the studied crystals an increase in light yield up to 30% has been established and, even more important, the uniformity improved considerably.

Crystal	Type	Uniformity [%/cm]		No. of Photoelectrons	
		without lacquer	with lacquer	without lacquer	with lacquer
S004	Pent	-1.3	-0.37	83.7	112.9
S029	Hex A	-0.6	0.075	59.3	78.7
S064	Hex B	-0.49	-0.035	67.2	78.4
S067	Hex B	-1.75	-0.2	52.2	84.5
S114	Hex C	-0.53	0.3	63.7	75.3
S161	Hex D	-0.26	0.05	56.2	78.3

Table 3-2 Some results regarding optical properties of different shapes of CsI crystals before and after applying optical coating. The relative error is considered to be 2%, where approximately half is statistical and half systematic in origin. The uniformity is defined by the relative change of the light output over the horizontal axes (z-axes) of the crystal.

3.2.4.3 Crystal Tomography

Two set-ups for a CsI crystal tomography have been established, one using cosmic muons and one operating with a ^{137}Cs source. A cross check with several crystals measured in both apparatus could demonstrate the equality of results. Variations in the optical non-uniformity of similarly shaped crystals after applying the surface treatment can be explained with different absorption length.

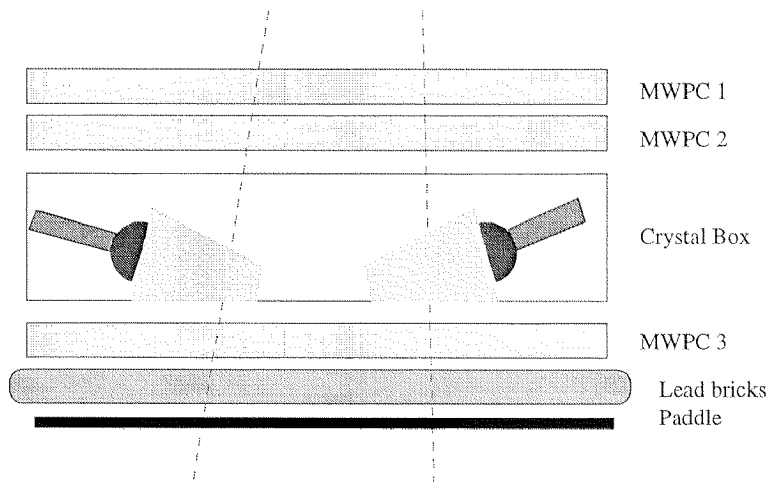


Figure 3-9 Cut through the Crystal Tomography Apparatus. The path of the cosmic muons is indicated by the dashed line.

The cosmic ray tomography apparatus consisted of three drift chambers, two above and one below the crystals. For the trigger two plastic scintillators were positioned on the floor, separated from the lower drift chamber by 5 cm of lead bricks, to allow the selection of minimum ionizing cosmic particles. The drift chambers have two orthogonal x-y-planes surrounded by three ground plates. The chambers allow cuts on cosmic muons that penetrated the crystals almost vertically ($>85^\circ$). Hence, a correlation between the light output per unit pathlength and the position can be set up, which results in a mapping of the position dependence of the crystal's light output. A typical result can be seen in Figure 3-10.

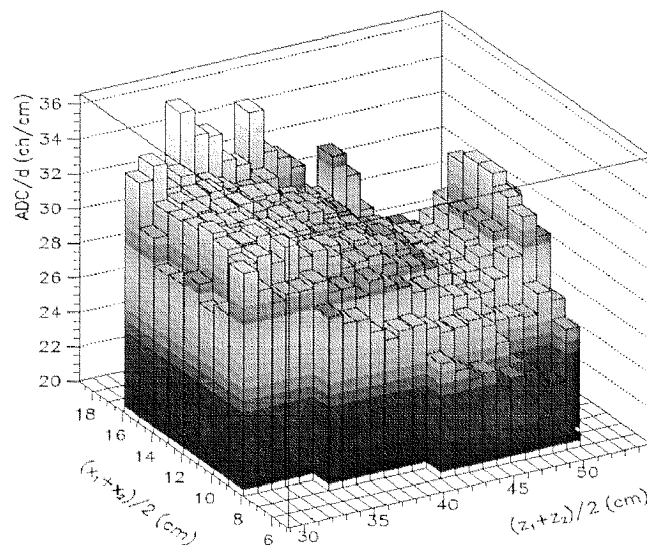


Figure 3-10 Two dimensional tomography pictures of a crystal's light output (#S122). The surface of the crystals was subdivided into rectangles of $2 \times 1 \text{ cm}^2$. The y-axis is showing the relative light output of each segment.

3.2.4.4 CsI Crystal Uniformity Tests with a ^{137}Cs Source

Due to difficulties with the wire chambers of the tomography apparatus and the forthcoming disassembly an alternative method had to be found. Encouraged by the work of other groups (e.g. [Bro95]) a study using a ^{137}Cs source was carried out. It was found that this method is consistent with our 3D tomography and well suited for uniformity tests.

A ^{137}Cs source was mounted on a 5cm x 10cm x 20cm lead brick collimator with a 6 mm hole. A frame of 15 mm plywood was built to accommodate a CsI crystal with its PMT and to move the lead collimator on top of the crystal. Two PENT and one HEX C crystal were covered with a light tight cardboard enclosure of 2 mm thickness. The PMT and the voltage divider were the same as for the final set-up. While one output of the base was terminated, the other output was fed into an Ortec 454 timing amplifier with a gain of 30 and time constants of 50 ns for both integration and differentiation. The same signal was discriminated at 60 mV to produce a trigger. The signal was digitized with a peak sensing Ortec AD811 ADC and histogrammed. The source produced triggers at roughly 3kHz. Several background runs were taken without the source but with the lead brick and subtracted from the spectra that were obtained with source. It was found that the background spectra were not sensitive to the exact position of the lead brick. ADC pedestal runs were taken with a clock trigger and used to correct the spectra. During the measurements for one crystal, the temperature variation was less than 0.3 Kelvin.

After background subtraction, the spectra were fitted with a Gaussian function. In order to take account of the Compton edge of the ^{137}Cs spectrum, an additional exponential background term was fitted. The centre and FWHM of a Gaussian distribution fitted to each spectrum was evaluated. The obtained centre then was corrected by subtracting the measured ADC pedestal. The statistical error at about 90000 counts was less than 0.3% for each source position. For each crystal, five points along the central axis were taken plus some points off-axis.

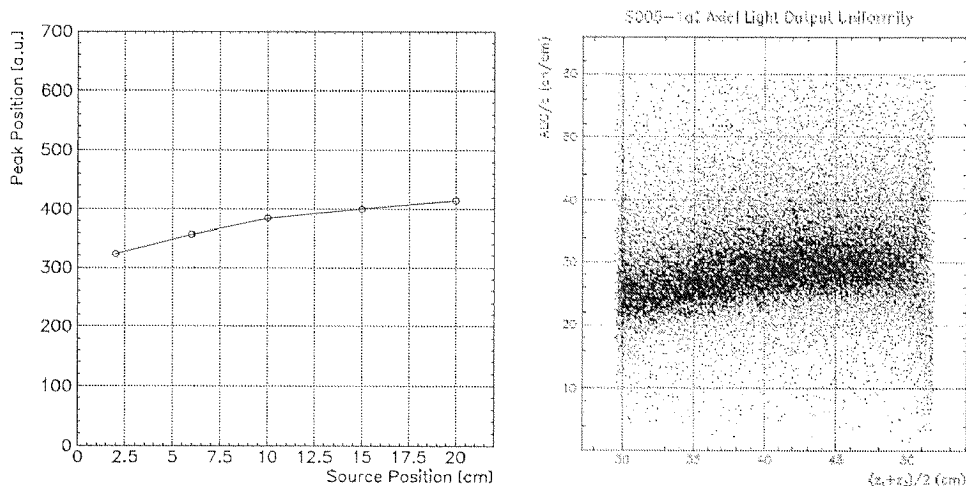


Figure 3-11 The pictures show the peak centres along the centre axis for one example CsI crystal (S005). The result of the ^{137}Cs measurement (left part) is compared with the corresponding data from the tomography (right part).

Figure 3-11 shows the equivalence between the peak position of a 662 keV photon (left side) and the tomography result using cosmic muons. The FWHM of the source measurement increases near the PMT where the light output is highly non-uniform due to the optical geometry. As a conclusion, the uniformity results obtained with a ^{137}Cs source are clearly correlated to the tomography data. Not only the general trend was reproduced, but also the quantitative uniformity obtained for the central axis was measured reliably. Since the photon energy of the ^{137}Cs source is sufficient to penetrate on average several centimetres of CsI, not just the surface but the interior of the crystal was probed. As it was impossible to track individual photons, the edge regions of the CsI could not be probed.

Since it was found that this faster and simpler method is consistent with our 3D tomography and well suited for uniformity tests an automated measuring apparatus was designed. It was called RAdioactive Source Tomography Apparatus, abbreviated as RASTA. It relies on a PC to control a stepping motor, collect information for each position and analyze the data.

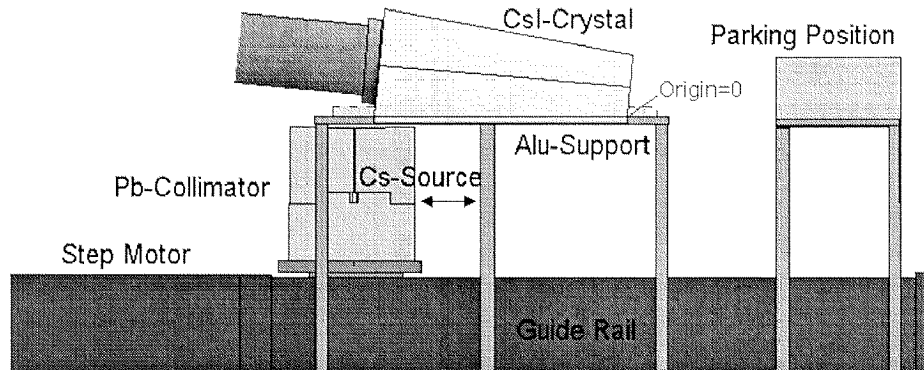


Figure 3–12 Layout of the RASTA apparatus for the automated light yield measurements using a ^{137}Cs source.

The ^{137}Cs -source is embedded in a Pb-collimator with an opening of 6 mm diameter. It has a thickness of 5 cm; thus the probability to penetrate the lead is $<1\%$ for the 0.66 MeV photons. The collimator, which is mounted on a plate, can be moved by an ISEL stepping motor with a precision of ~ 12.5 microns (the crystal itself is can be placed with ~ 0.3 mm precision). An RS232 interface is used to control the stepping motor by PC.

3.2.5 Calibration of the Light Yield

The statistical term in the expression for a detector's energy resolution (Eq. 3.a) is directly proportional to the light yield of the scintillating crystal. The relevant quantity that accounts for possible inefficiencies of the scintillator-phototube system is N_{ph} , the overall number of photoelectrons per MeV energy deposition. N_{ph} was measured in the RASTA-apparatus described above. The light yield of each CsI crystal was determined by a light emitting diode(LED)-based system, since LED light generates a fast 20 ns PMT anode signal. The LED was mounted on the back of the crystal to probe. It was pulsed at 1 kHz rate with adjustable driving voltage and the split output from the driver generated a 100 ns wide ADC gate. (In a separate measurement the ADC pedestal values were established.) The integrated number of photoelectrons from the LED corresponds to energy depositions between 10 and 100 MeV, depending on the LED voltage. From simulation one knows the average energy deposition of cosmic muons in the different CsI crystal shapes which lies between 39 and 51 MeV. Hence, an absolute energy scale was established and the LED light output was precisely cross-calibrated against the cosmic muon events in the crystals.

A total of 9 different LED amplitudes were used in data collection with each CsI crystal, since the variance (σ_T) of the photodiode peak depends on the number of photoelectrons created for unit energy deposition. Hence

$$\sigma_T^2 = \sum_i \sigma_i^2 + \frac{E}{N_{\text{ph}}},$$

where E is the LED spectrum peak position, N_{ph} represents number of created photoelectrons per unit deposited energy, and σ_i are assorted variances, such as instabilities of the LED driving voltage,

temporal pedestal variations, etc¹. The measured points are fitted with a linear function and such the number of photoelectrons per MeV for each CsI crystal was established. That number varies from 40 to 110 photoelectrons/MeV.

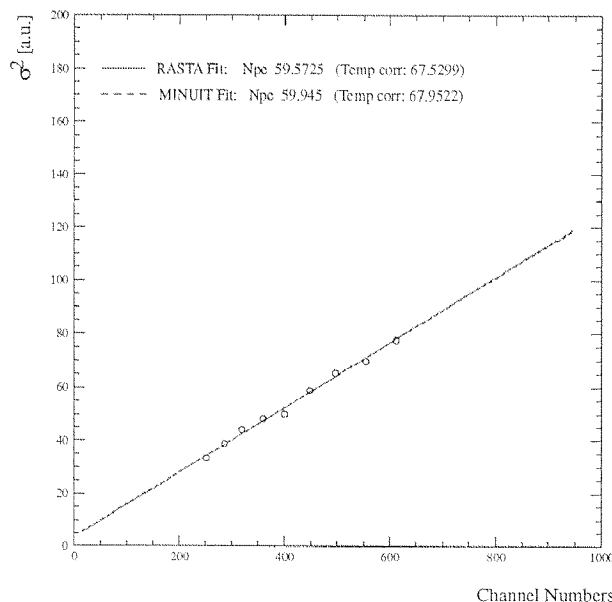


Figure 3–13 Obtaining the number of photoelectrons by the slope of LED amplitude variances. The offset from zero is caused by noise sources different from Poisson statistics.

3.2.5.1 Photomultiplier and Optical Coupling

The use of quartz window PMTs is mandatory due to the low emission wavelength of the scintillator crystals. In order to accomplish linearity and gain-stability 3 inch EMI 9822QKB and 2 inch EMI 9211QKA phototubes are used for the readout of the CsI crystals. They offer good quantum efficiency and linearity over the full dynamic range of the calorimeter using a properly designed voltage divider². SbCs dynodes have been chosen to reduce rate dependent effects of secondary electronemission. These effects can be caused by ion migration or direct impact heating [Smi95].

We used Dow Corning's Sylgard 184 for the permanent attachment of the PMT to the crystal. Sylgard 184 is an Polydimethylsiloxane (PDMS) elastomer that is cured by an organometallic crosslinking reaction. After curing it provides a hydrophobe rubber film with good transmission of UV light. The siloxane base oligomers contain vinyl groups. The cross-linking oligomers contain at least 3 silicon hydride bonds each. The curing agent contains a proprietary platinum-based catalyst that catalyses the addition of the SiH bond across the vinyl groups, forming Si-CH₂-CH₂-Si linkages. The multiple reaction sites on both the base and crosslinking oligomers allow for three-dimensional crosslinking [Cam97]. One advantage of this type of addition reaction is that no waste products, such as water, are generated. Curing agent and Sylgard were mixed for the application in a weight ratio 1:8 and pre-processed in vacuum. The yet bubble-free viscous mixture was poured on the PMT. Then in a dedicated frame the PMT was slightly pressed onto the rear face of the crystals. Due to adhesion it couples the quartz-glass to CsI; hence the phototube can be removed by applying strong shear forces. After ca. 24 hours of hardening the film offers mechanical and optical properties that are stable over time.

¹ The presence of the so-called excess noise would add a linear term to this formula (the 'Fano factor' F). For a LED the assumption $F-1=0$ is sufficiently accurate.

² The voltage dividers are designed and built by B. Stephens from UVA

4. Performance of the CsI-Calorimeter

In the previous chapters we have reviewed the properties of the scintillating material, the requirements on the individual modules and the idea behind the calorimeter construction. This chapter focuses on the design, simulations and studies of the Calorimeter and its various parts.

Prior to the construction of the detector Monte Carlo simulations have been studied in order to specify the requirements for the individual detector modules, study background processes, trigger layout, etc. The concept for the detector was approved by comparing results from the simulation codes GEANT, EGS4 and ITS [Poc89].

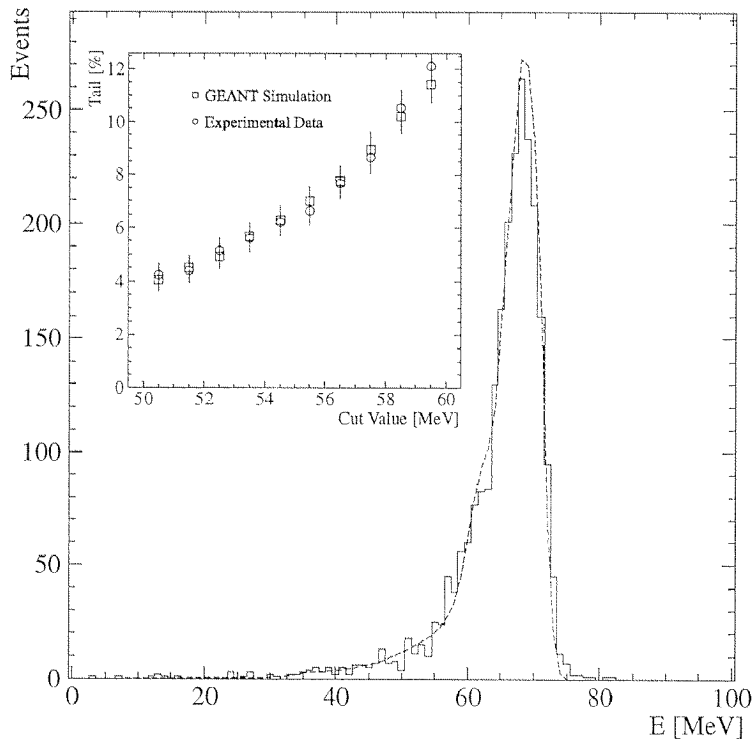


Figure 4-1 Comparison of data (histogram) and simulation (dashed curve). The insert emphasizes the fraction of the integral below the cut value divided by the total integral. Picture taken from [Bro96].

With the delivery of the first CsI crystals measurements and simulations could be compared and modifications of the simulation were included in the study. Results from test-beam periods and crystal tomography data have been implemented. The calorimeter simulation also includes wrapping materials, photon statistics and the position dependence of the light yield. Very good agreement between measured and simulated results, especially in the tail region, was obtained [Ass95]. As a conclusion, simulations assist reliably in data analysis, including calibration of the individual modules and determination of correction factors (as will be seen in ch.7).

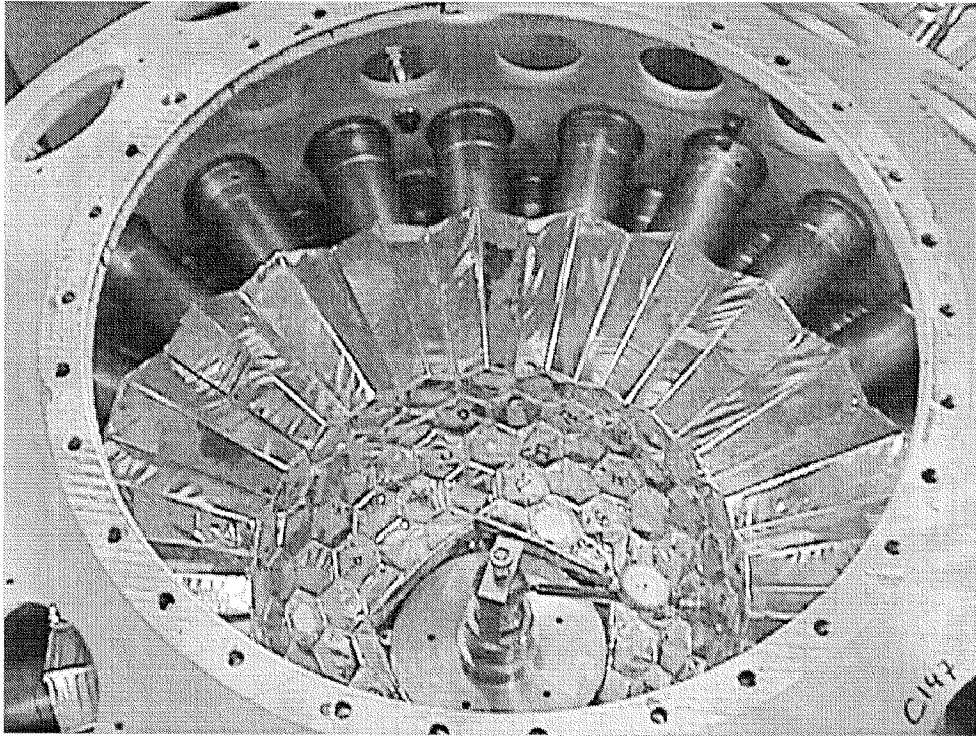


Figure 4-2 Photograph taken during the CsI assembly of the sphere showing radial adjustment.

The electromagnetic calorimeter was optimized for similar response to both ~ 68 MeV photons and ~ 69 MeV positrons, for compactness, high granularity and high stopping power. This is best accomplished by a sphere consisting entirely of sensitive material. In order to approach an optimal detector as close as possible the entire support structure is located on the periphery of the calorimeter. Hence, apart from $200 \mu\text{m}$ of wrapping between the crystals, all of the calorimeter volume is sensitive and no heavy material is placed between the target and the CsI crystals. This minimizes energy degradation - or even showering - in front of the calorimeter. Photons or positrons leave the target, pass the wire chamber and the hodoscope and start showering after some centimetres within the calorimeter. The positrons also can lose up to 6.4 MeV in the target and generate a signal in the wire chamber and the hodoscope.

The processes involved in the energy loss in the calorimeter for both kinds of particles are similar. Both particles initiate a repetitive pair-production and bremsstrahlung process. Positrons are likely to start the shower earlier due to scattering and bremsstrahlung losses in the heavy CsI medium. This affects the acceptance, the angular resolution and the low-energy tail due to leakage.

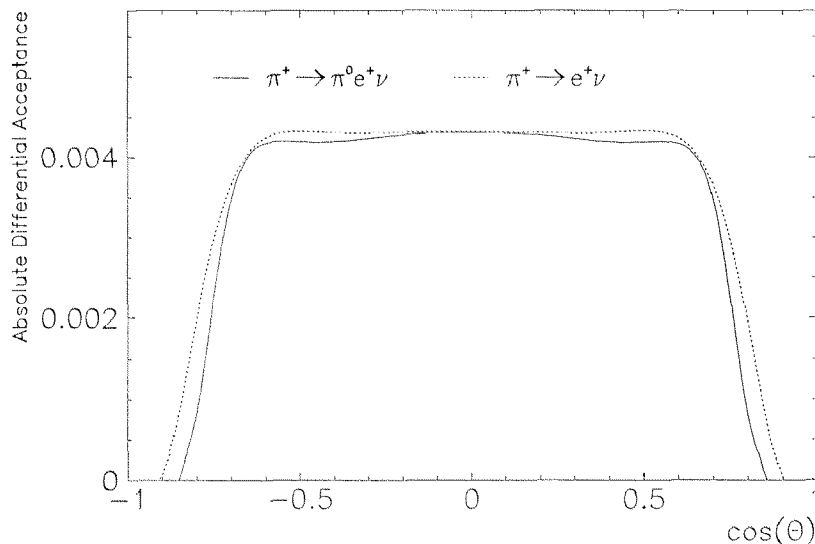


Figure 4-3 Absolute differential acceptances of the CsI calorimeter. The small deviation will be one source of corrections in the determination of the pion beta decay rate. Close to the CsI Veto-rings the deviations are due to shower leakage. At smaller angles the finite size the target causes differences in the transport of photons and positrons.

The acceptances for obtaining the pion beta decay and the calibration process $\pi^+ \rightarrow e^+ \nu_e$ will differ slightly. One reason is a lower probability to detect both photons from the π^0 decay as opposed to a single positron close to the veto crystals. Another source of deviations is the slightly different shower development for positrons and for photons that affects the acceptance after energy cuts; this again enhances the positron acceptance. Positrons lose energy during their passage through matter. This energy is dependent on the emission angle, therefore the acceptance will slightly decrease at larger angles. The absolute differential acceptance obtained from simulations, which include the above mentioned points, can be viewed in Figure 4-3.

4.1 Refinements to the GEANT Simulation

In a reliable simulation all detector module materials, intrinsic properties of the calorimeter, as well as details pertaining the trigger and readout have to be accurately described. This includes for example electronic noise, photoelectron statistics and the individual crystal non-uniformities. The electronic noise was included after fitting a Gaussian distribution to the pedestal of all channels under consideration. After fitting, the averaged position and width was implemented into the simulation code. To this end a randomly generated number - within the parameters of the obtained Gaussian - becomes added to the energy deposited in a crystal volume.

As reported in sect. 3.2.4, the optical non-uniformity as well as the light output of each crystal was measured. The photoelectron statistics is taken into account in the simulation in the following way. The measured number of photoelectrons per MeV for each crystal is used to generate a normalized Poisson distribution in the simulation code for the detector module. The calculated energy deposited in the crystal is then multiplied for each step with the corresponding Poisson distribution.

The optical non-uniformity that maps the average energy deposition of minimum ionizing particle per volume unit cells of each crystal resulted in a characteristic response function reflecting the measured axial and transverse non-uniformities. This function is convolved with the GEANT shower energy distributions of positrons and photons in the PiBeta detector. This requires some adaptation for the simulation, since the light output per MeV now depends on the shower depths inside the crystal. Although most of the crystals show positive non-uniformity, which indicates an increase of luminosity

towards the readout device, some have a negative coefficient. A CsI crystal with a positive non-uniformity would 'gain' energy, while a crystal with negative non-uniformity would lose energy. The gains of the 240 CsI modules have to be unified, therefore.

The gain matching procedure requires two sets of simulations. In one set perfect scintillators are assumed, while in the other non-uniformity is included in the simulations. 240 sum spectra are created for the comparison of both cases. A 'sum' histogram corresponding to a given crystal is incremented only for those events in which this crystal receives at least 50% of the total energy deposited in the calorimeter. The histogrammed variable is the summed energy of all crystals that received more than 0.5 MeV of energy above the noise threshold. The use of single spectra was not practical due to the great lineshape differences for different crystals. The resulting individual sum spectra show scaleable differences in their peak position. Software gain factors are obtained through repetitive comparison of the ideal and 'real' spectra. Both Kolmogorov-¹ and χ^2 -test were applied for comparison. After about four passes a final set of software gains was found. Table 4-1 is showing a sample of 37 out of 44 crystals that were used during the 1996 beamtime. Here 70 MeV positrons were emitted uniformly onto an array of 44 crystals. This table indicates that both methods result in similar values.

Channel #	Zero Non-uniformity		Unmatched		Kolmogorov-Test		χ^2 -Method	
	Peak Position	FWHM	Peak Position	FWHM	Peak Position	FWHM	Peak Position	FWHM
1	67.02	3.94	64.99	4.86	66.34	4.86	66.29	4.43
2	67.21	3.50	65.63	3.79	66.86	3.85	66.81	3.65
3	67.43	3.30	65.80	3.66	66.76	3.93	66.76	3.89
4	67.20	3.60	64.67	4.53	66.86	3.83	66.10	4.46
5	66.97	4.35	63.95	5.31	66.62	5.50	65.94	5.40
6	67.18	3.73	66.92	4.32	67.11	4.01	67.04	4.08
7	66.44	4.63	62.53	5.56	66.16	5.90	64.86	5.79
8, 9								
10	66.30	4.46	67.01	4.33	65.88	4.45	66.40	4.56
11	67.82	3.54	65.27	3.92	67.68	3.93	67.28	3.76
12	68.02	3.10	67.45	3.32	67.48	3.52	67.95	3.32
13	67.97	3.16	67.69	3.03	67.85	3.13	67.87	3.27
14	67.90	3.22	67.93	3.30	67.46	3.25	68.10	3.18
15	67.84	3.35	69.75	4.04	67.19	4.00	67.82	3.87
16	67.46	3.65	66.56	4.01	67.47	3.65	67.18	3.68
17	67.61	3.24	67.41	3.42	67.19	3.26	67.30	3.09
18, 19								
20	66.55	3.99	67.37	4.35	66.53	3.95	66.77	4.36
21	67.44	3.44	68.35	3.29	67.13	3.52	67.65	3.30
22	67.82	3.29	67.76	3.13	67.81	3.04	68.16	2.99
23	67.84	3.04	68.48	2.99	67.64	2.69	67.97	2.95
24	67.97	2.71	68.30	2.76	68.09	2.69	67.37	3.29
25	67.79	3.10	67.17	3.36	67.85	3.02	67.51	3.56
26	68.02	2.90	67.06	3.21	67.74	2.99	67.56	2.90
27	66.89	3.72	66.78	3.51	66.78	3.44	66.87	3.63
28, 29								
30	66.97	3.57	68.06	3.65	67.09	3.29	67.24	3.27
31	67.67	3.15	67.90	2.91	67.40	2.94	67.75	2.98
32	67.83	3.06	67.52	2.92	67.78	2.79	67.81	2.80
33	67.37	3.17	67.43	3.21	67.25	3.24	67.37	2.99
34	66.91	3.82	67.21	3.75	66.88	3.63	67.04	3.70
35								

¹ For a description see [Hbo95]

36	64.03	6.89	62.43	9.28	64.56	6.47	64.30	7.46
37	66.65	4.46	64.06	5.78	65.80	4.93	65.13	5.25
38	67.50	2.95	66.36	3.35	67.54	3.12	67.11	3.29
39	66.81	3.99	67.82	5.90	66.52	4.71	67.29	4.78
40	64.77	5.64	57.94	9.69	64.30	5.55	63.00	6.80
41	68.88	2.94			68.98	3.11	69.03	3.23
42	60.57	4.01			59.39	4.01	58.70	4.02
43	60.82	3.96			60.96	4.08	60.67	
44	67.49	3.50			67.46	3.32	67.50	3.56
Average	67.19±0.9	3.69±0.8	66.41±2.3	4.20±1.6	66.96±0.9	3.85±1.0	66.90±1.2	3.96±1.1
Inner Six	67.86±0.1	3.08±0.2	68.19±0.9	3.23±0.5	67.67±0.3	3.07±0.5	67.76±0.3	3.28±0.4

Table 4-1 Table demonstrating the influence of crystal non-uniformity to peak position and resolution. The first two rows refer to a simulation run without compensation for the non-uniformity of the individual crystals. The others include a gain correction factor obtained by comparing single spectra without non-uniformity and with non-uniformity.

The gain matching has been repeated with several energies in order to check consistency. Thus it was carried out for 129 MeV photons and for both 70 MeV positrons and photons. Following the gain matching routine as described above one settles with a set of software gain factors. Beside the consistency among those three simulated energies the accuracy of the final set of software gains can be cross checked by looking at the energy resolution.

4.2 Angular Resolution and Track Reconstruction

For a reliable kinematic analysis a good angular resolution is desirable, since the decay angles are directly related to the particle energies. It is helpful to reconstruct the particle track which for photons is only accessible through the energy distribution within the calorimeter. The principle of photon track reconstruction was cross checked with the wire chamber information for positrons, which will be shown in Figure 4-7.

The theoretical angular resolution was obtained by comparing the reconstructed tracks with the coordinates of the thrown particle in simulation. The shower reconstruction routine simply is looking for the mean of the shower distribution in order to determine the point of incidence and compare it with the thrown angle in the simulation. Positrons, as well as photons, were thrown uniformly over the detector array of 44 crystals; then a cut that required the shower maximum to be within the innermost crystals was applied. This cut notably reduced the low energy tail - due to shower leakage - notably (see Figure 7-10 and sect.7.5). Since a shower normally develops in a cone, besides the crystal containing the largest fraction of energy some neighbouring truncated pyramids are affected as well. Thus the portion of contributed energy of each affected crystal has to be weighted with an exponent $\alpha < 1$. Consequently the formula to reconstruct the point of incidence becomes

$$\Theta_{rec} = \frac{\sum_i \Theta_i q_i^\alpha}{\sum_i q_i^\alpha},$$

where q_i is the fraction of deposited energy in the i -th crystal E_i/E_{tot} . The same applies for the ϕ -direction.

Now the proper weighting factor α had to be found: An angle ω was defined describing the deviation of the reconstructed position from the thrown position. It is given by

$$\cos \omega = \cos \theta_{rec} \cos \theta_{thrown} + \sin \theta_{rec} \sin \theta_{thrown} \cos(\phi_{rec} - \phi_{thrown}) \quad (4.a)$$

This angle was minimized by varying α which resulted in a value of 0.71 for α at an angular resolution of 3.6°.

<i>Weighting factor α</i>	<i>Angular Resolution</i>
0.35	$4.2^\circ \pm 0.3^\circ$
0.71	$3.63^\circ \pm 0.2^\circ$
1.00	$3.77^\circ \pm 0.2^\circ$

Since electromagnetic showers develop as a symmetrical cone with definite radius only in average, an investigation of accounting for non-uniform shower distributions by applying a dipole-like correction with an additional weighting of the angular distance to the shower centre has been studied. Since the distance s of the two vectors \vec{r}_1 and \vec{r}_2 in spherical coordinates is given by

$$s = |\vec{r}_1 - \vec{r}_2| = R\sqrt{2(1 - \cos\omega)} \quad \text{one writes } \theta_{rec} = \frac{\sum_i \theta_i q_i^\alpha (1 - \cos\omega_i)^\beta}{\sum_i q_i^\alpha (1 - \cos\omega_i)^\beta},$$

where q_i is the fraction of energy and $\cos(\omega_i)$ the angular distance between the i^{th} crystal and the mean shower depth.

The improvement was marginal (3.61° angular resolution with $\alpha=0.53$ and $\beta=1.9$) and thus the initial method has been retained unchanged.

T. Noble [Nob90], working with rectangular NaI(Tl)-crystals, reports a weighting factor α of 0.55. This can be understood by the geometry of an electromagnetic shower. A hexagonal pyramid that contains the largest energy fraction of the shower is more likely to be the crystal which first was hit by the initial particle than for the case of a rectangular crystal. Consequently, for a planar geometry, neighbouring crystals are playing a more important role and, hence, the weighting factor must be lower.

Ideally one would expect a uniform distribution of the reconstructed positions as the thrown particles are distributed uniformly. But, due to the considerable size of the crystals, showers that are distributing energy over a large fraction of the detector cannot be reconstructed precisely. The average angle between two crystal centres is about 12° .

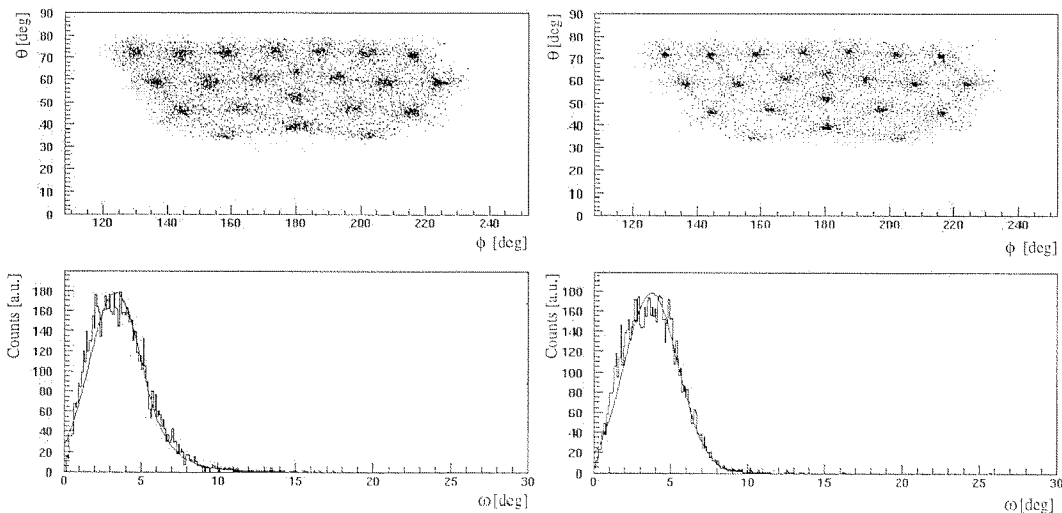


Figure 4-4 Comparison of the position reconstruction (above) and angular resolution respectively (below), for the found optimal weighting factor (left) and weighting factor 1 (right).

The main limitations for obtaining a better angular resolution (besides the granularity) are shower fluctuations that lead to a large uncertainty of the reconstructed position of incidence. This can be demonstrated by trying to reconstruct a pencil-like photon, or positron, beam. If those simulated tracks are off a crystal's centre, without applying weighting the distribution is small, but the reconstructed point of incidence deviates considerably. With a weighting factor the error for the reconstructed incidence is lower, but the distribution gets wider, because neighbouring crystals occasionally are

receiving a major fraction of the total energy. Hence, in the θ - ϕ -plot the crystal positions are still recognizable (Figure 4-4). The tail to higher angular differences is due to shower fluctuations. Better results can be obtained if one restricts to showers starting close to a crystal centre, but this compares to a too restrictive cut that requires more than 80 per cent of the shower energy in a designated crystal.

Differences between the shower distributions of photons and positrons can also be found in studying the angular resolution. Therefore the theoretical angular resolution for positrons and photons of 10, 30, 50 and 70 MeV was determined. This is summarized in Figures 24 and 25. There the angular resolution, defined as the angle between the thrown and the reconstructed trajectory, for positrons and photons is plotted for ten values of α .

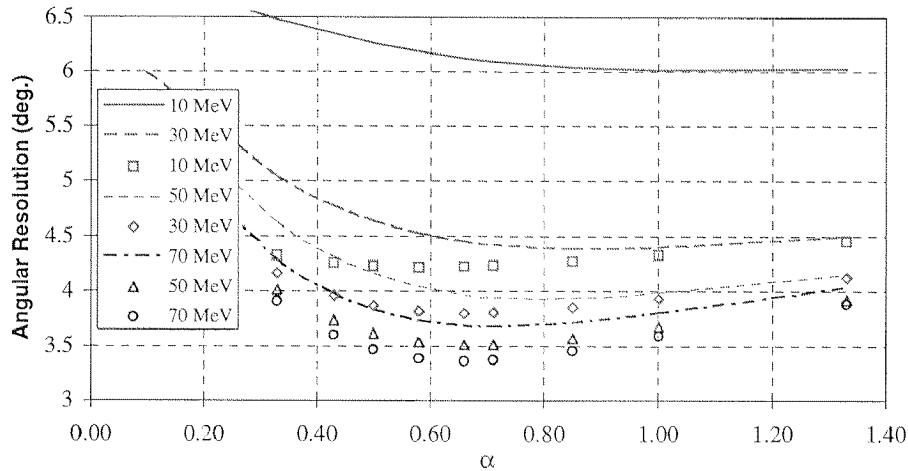


Figure 4-5 Comparison of the angular resolution for photon (symbols) and positron (lines) induced showers obtained using different weighting factors.

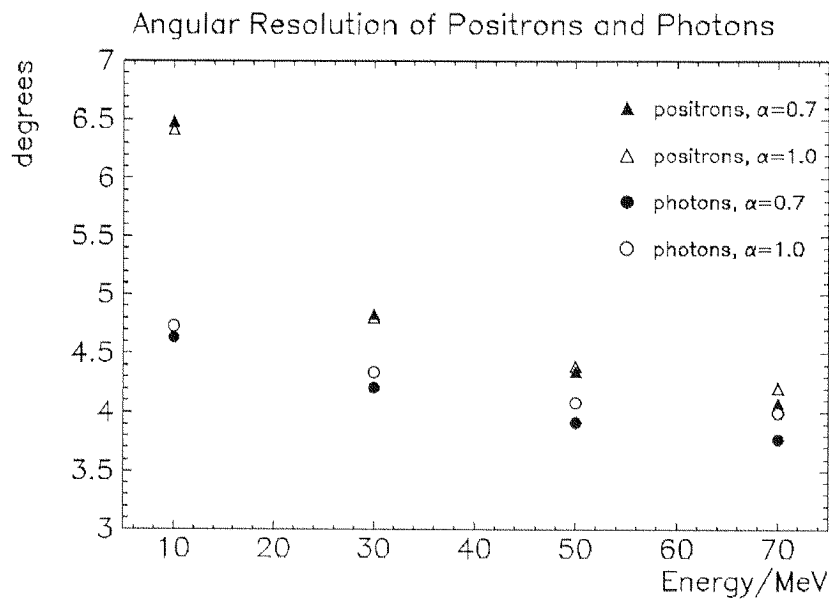


Figure 4-6 Comparison of the angular resolution of photons and positrons at different energies. See text for a detailed interpretation.

The comparison reveals two obvious results. For both types of particles the resolution improves with higher energy, which even is more pronounced with positrons. At higher energies the showers will start deeper inside the crystal volume and due to its shape the shower energy is spread over a lesser number of crystals. Furthermore the shower cone becomes smaller. Positrons have a lower angular resolution in comparison with photons for the same reasons; they initiate showers earlier. Another difference,

regarding photon and positron induced showers, is the optimal value for the weighting factor α . For photons its value varies slightly from 0.58 at 10 MeV to 0.66 at 70 MeV while for photons at 10 MeV $\alpha=1$ seems to be best. The optimum factor for photons then decreases to 0.71 for 70 MeV. The factor α is considered to be directly proportional to the shower cone radius divided by the angle between the crystal's front face and its sides. If the shower would develop in the same way as the crystal becomes wider α should be 1. This means that low energy positrons must have a larger shower cone than more energetic positrons. The converse change for photons can be explained with a deeper penetration of the crystals in general (see also Table 7-2).

During the 1996 beam time two small wire chambers were used for beam monitoring. They also acted as an interface between data and simulation. So the theoretical angular resolution could be compared with the measured one. Using positrons the wire chambers allowed to determine the intersection point with a precision of 0.2 mm, approximately. With a 70 MeV positron beam of 1 cm diameter impinging the array perpendicularly an angular resolution of $3.8^\circ \pm 0.2^\circ$ was obtained. This result cannot be compared directly to the simulated value given above, since the array was illuminated uniformly there. Trying to simulate the conditions during data taking the reconstruction of the impact point peaked at the same position as for the data. The slower fall-off of the tail can be explained with a non-uniform beam distribution due to an allowed beam divergency of 2° .

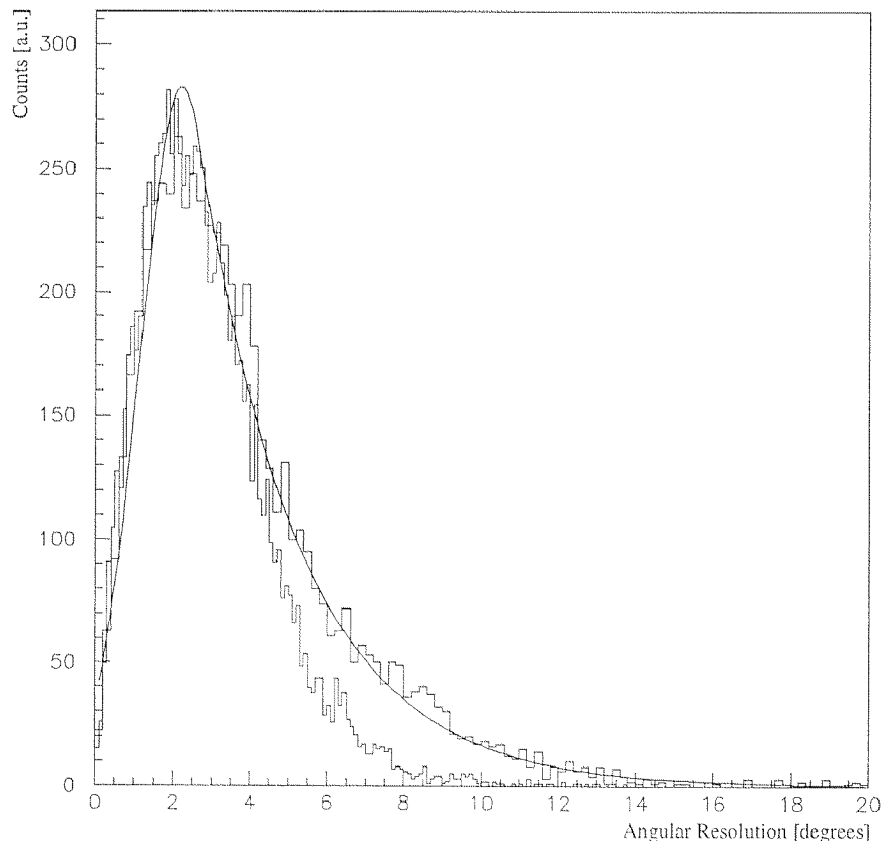


Figure 4-7 Comparison of measured and simulated angular resolution. The histogram obtained from 1996 beamtime period was superimposed by a Gauss-exponential curve to guide the eye. For the tail difference see text.

4.3 Detector Performance in Beam

In 1996 and 1997 the detector performance and trigger set-up were tested with an array of 44 CsI crystals mounted on the steel cone piece that is also foreseen to be used in our final assembly. The 44

crystals comprise a fifth of the final detector. The horizontal axis of the support structure coincided with the equator of the sphere and therefore allowed position setting in θ -direction. The whole assembly sat on a pivot that was positioned exactly under the centre of the sphere. The pivot enabled detector positioning in ϕ -direction. Eight hodoscope modules were placed inside the conical support piece. The length of the hodoscope detectors was one half of the final design length (see Figure 4-8). Everything was mounted on the detector platform and surrounded with a thermal-house that was made light tight.

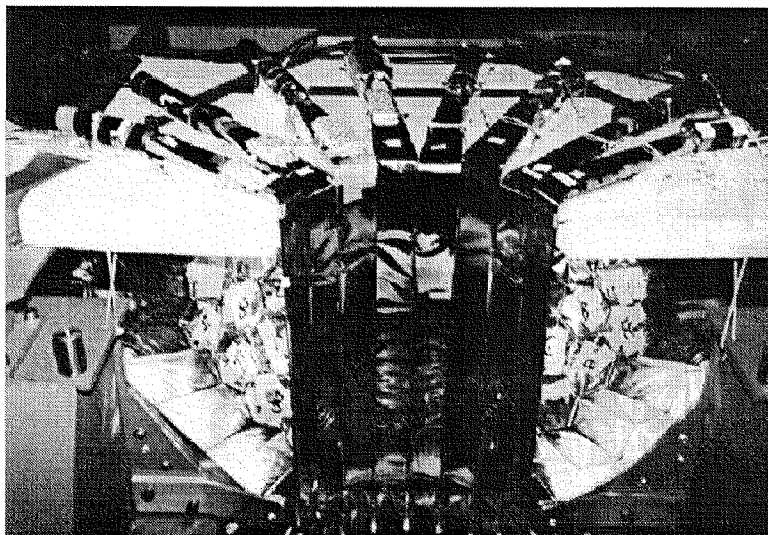


Figure 4-8 Photograph of the detector array used for the test beam periods in 1996 and 1997. The plastic scintillator strips are mounted on the ring for the final assembly, but have only half of the final design length. For this reason the lightguides and phototubes have been mounted perpendicular to the scintillation plane (upper third of the picture). The crystals are placed underneath and form a fifth of a sphere.

This apparatus was used in the $\pi E1$ -beam line of PSI, the same as for the planned experiment. Several set-ups have been studied for these tests. A plastic scintillator target (with the same dimensions as described in ch. 2) was used to set-up the triggers and to provide on-line calibration using the Michel decay endpoint at 52.8 MeV. Later $\pi^+ \rightarrow e^+ \nu_e$ events have been recorded. (The determination of the radiative pion decay rate will be reported in ch. 5.) Then the obtained calibration and resolution were cross-checked with a 70 MeV positron beam. The energy resolution was determined and the low energy tail due to shower energy losses. In 1997 also a liquid H_2 -target was used to produce photons (through charge exchange reaction) in this energy region. The 1997 beam period emphasizing the Panofsky ratio determination will be reported from chapter 6 onwards.

Between the 1996 and 1997 beam period the surface treatment of the CsI crystal was changed with the use of the WLS lacquer. The test with the tomography set-up has shown an improvement in the number of photoelectrons as well as in the uniformity of light collection. The overall improvement has been established by comparing the results of both beam periods. Figure 4-9 shows a result of the 1997 measurement of the PiBeta calorimeter resolution using a 44-detector subset directly illuminated by 70 MeV positrons, and compares it with 1996 data. The energy resolution has clearly improved.

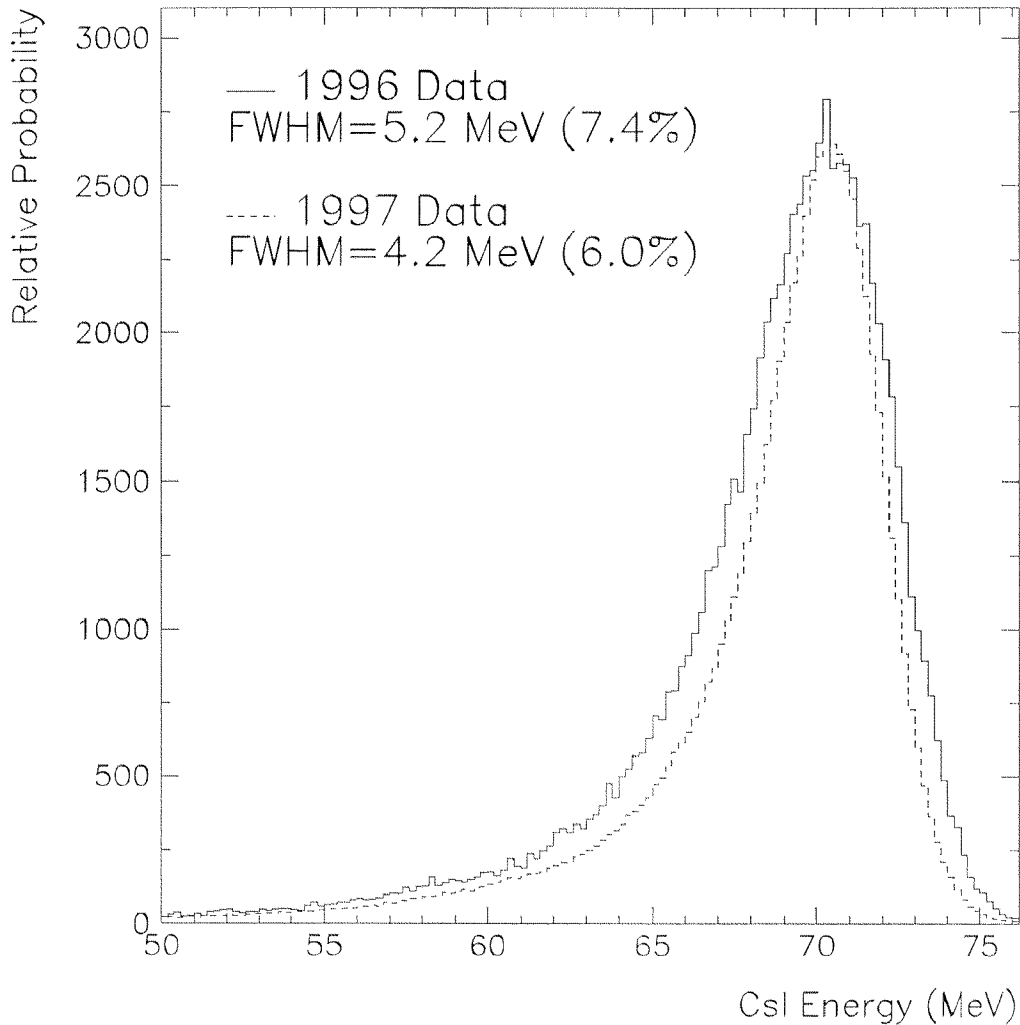


Figure 4-9 Energy response of a 44-detector pure CsI array to 70 MeV/c positrons measured in 1996, before the WLS lacquer surface treatment (full line), and after the treatment (1997, dashed line).

4.3.1 On-line Calibration

The well-defined endpoint in the Michel positron spectrum at 52.83 MeV allows an on-line calibration of the detector between data taking runs. Here a set of reference histograms, which can be either a set of previously calibrated data or simulation generated histograms, is compared to the actual data using the minimum χ^2 -method. The histograms are taken during data runs using the Master Trigger Unit (MTU) pattern of the prescaled Michel events. When a significant gain drift would be noted, a change in the HV setting accordingly to the formula¹ $HV_{new} = \sqrt[10]{g} \cdot HV_{old}$, where g is the necessary gain factor, was applied. During the test beam run in 1996 it could be shown that 44 PMT readout channels worked stable for a period of a week [Rit96]. The average deviation of one channel was about $(0.5 \pm 1)\%$ per week. This also demonstrates the stability of the temperature control system.

¹ This formula is valid for a 10 stage PMT.

4.3.2 On-line Results

After equalizing the gains of the 44 CsI-modules the energy resolution was determined using a 70 MeV positron beam. Two plane MWPCs were used to accept only positrons of proper momentum by excluding beam divergencies of more than 2%. Sum histograms were generated for the innermost 18 crystals by adding all CsI modules whenever the crystal of interest got the main fraction of the shower energy. The differences in the obtained energy resolutions reflect the measured number of photoelectrons and non-uniformities. The average contribution from the noise of approximately 0.1 MeV is negligible.

Crystal Channel	Crystal Name	N_{ph}	Uniformity [%/cm]	FWHM %	in σ [MeV]	calculated σ
C11	S161	78	0.055	5.4	1.6	1.4
C12	S064	78	-0.035	5.5	1.6	1.4
C13	S028	71	0.660	5.9	1.8	2.4
C14	S035	81	-0.175	5.2	1.5	1.4
C15	S068	50	0.045	6.9	2.1	1.7
C20	S115	66	0.065	5.3	1.6	1.5
C21	S112	69	0.355	5.8	1.7	1.8
C22	S029	79	0.075	5.7	1.7	1.4
C23	S002	116	0.370	5.3	1.6	1.6
C24	S021	79	-0.145	5.3	1.6	1.4
C25	S114	81	0.320	6.3	1.9	1.6
C26	S117	70	0.190	6.0	1.8	1.5
C29	S165	89	0.585	7.5	2.2	2.1
C30	S062	83	0.055	6.3	1.9	1.3
C31	S031	51	0.050	5.8	1.7	1.7
C32	S061	93	0.135	5.9	1.8	1.3
C33	S162	70	-0.015	5.4	1.6	1.4
C37	S130	64	0.025	5.9	1.8	1.5

Table 4-2 Summary of the obtained energy resolutions of the inner CsI modules during the 1997 beam period obtained with 70 MeV positrons directly impinging the array. The figures are obtained by summing over the whole array, when the crystal of interest achieves the main fraction of an electromagnetic shower.

The average energy resolution (FWHM) of the inner part of the array for 70 MeV positrons was determined to be 4.2 MeV. Most of that amount can be directly attributed to the optical properties of the individual modules. A major contribution comes from shower spread over several modules with different uniformities and intercalibration uncertainties. Minor contributions are due to electronic noise.

5. Radiative Decays of Pions and Muons

Pion and muon decay processes are often associated with additional photons (see Table 2-3). The main source of radiative decays is 'inner bremsstrahlung' of either the pion or muon in motion or of a daughter particle, as there is the muon or the electron, respectively. Most of those processes are indistinguishable from non-radiative decays, since the photon energy is low and the angle relative to the charged decay product small. More interesting regarding the physical relevance of their origin are processes that emit photons as the result of the finite size of the pions or due to QED corrections for the muons. These structure dependent radiative decays allow the determination of pion form factors or the strength of axial vector coupling in the case of the muon. (See [Bry82] and [Cri61] for a comprehensive introduction into the theory of radiative decays of pions and muons, respectively.) The measurement of the probability of radiative decays will also be a feature of the PiBeta detector. An additional test of the standard model can be achieved this way in addition to a reduction of the systematical error for the determination of the pion beta decay rate.

In general all measured or calculated decay rates do include radiative decays - regardless of the origin of the emitted photon. Their relevance for the upcoming measurement of the pion beta decay rate are twofold: i) Neglected radiative $\pi^+ \rightarrow e^+ \nu_\mu$ decays would result in an additional uncertainty due to an underdetermined calibration process and ii) four-fold coincidences of pairs of $\mu^+ \rightarrow e^+ \nu_e \bar{\nu}_\mu (\gamma)$ decays could fake a $\pi\beta$ event. For both cases the relative strength and the emission angle between photon and charged particle have to be recorded. Hence, the calorimeter acceptances and a possible cluster recognition algorithm had to be studied.

In order to measure the exact $\pi^+ \rightarrow e^+ \nu_e$ decay rate also the radiative mode has to be included. This requires an identification of the actual decay process and a determination of radiative decays. The most likely process is the $\pi \rightarrow \mu \rightarrow e$ chain with a 14% probability for the radiative decay $\mu^+ \rightarrow e^+ \nu_e \bar{\nu}_\mu \gamma$ (at a γ threshold energy of 10 MeV [Cri61]). This is identified by the presence of a charged particle and a total energy of at most half the muon mass¹. Since the signature of the $\pi\beta$ event is determined by the presence of two photons with nearly identical energies, the $\pi^+ \rightarrow e^+ \nu_e$ peak clearly can be identified by an energy exceeding 55 MeV [Law98, Ass95]. Furthermore the difference in lifetime will give different signatures in the target.

There are two major concerns regarding the decay $\pi^+ \rightarrow e^+ \nu_e \gamma$. In the unlikely case of a low energy neutrino it contributes to the background of the $\pi\beta$ event. Due to the high chamber efficiency, the probability to have two clumps in opposite clusters without a charged particle identification calculates² to be $1.91 \cdot 10^{-13}$. From kinematics it can be seen that only large emission angles, and therefore high photon energies, can be problematic. For lower angles a cluster summing algorithm, which will be explained in the subsequent section, will take care of radiative decays. The relative emission angle between positron and photon in the following is denoted as ϕ .

¹ The so-called Michel edge at 52.83 MeV

² Here a cut on 50 MeV positrons and muons at a relative angle of $>170^\circ$ is assumed (this was chosen due the trigger thresholds and the kinematics of the $\pi\beta$ -decay assuming 3 deg angular resolution). This leads to a BR of $0.47 \cdot 10^{-8}$ for $\pi^+ \rightarrow e^+ \nu_e \gamma$. For the parametrization of this calculation see [Bry82]. The charged particle tracking inefficiency comprises MWPCs and PV hodoscope and, hence, is about $4.0 \cdot 10^{-5}$.

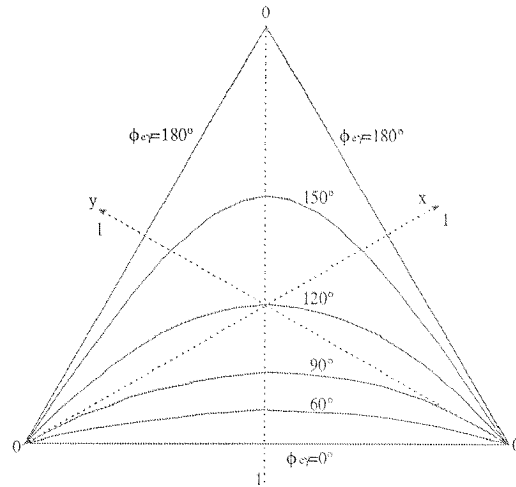


Figure 5-1 The kinematics of the decay $\pi^+ \rightarrow e^+ \nu_e \gamma$. The calculation follows 3 body decay kinematics. The allowed region here is bound by the dotted lines (x, y or $z=1$); where x corresponds to the photon energy defined by $x = 2E_\gamma / m_\pi$ (in the rest frame of the pion); y and z are equally defined for the electron and the neutrino, respectively.

Regarding a simulation of the entire PiBeta calorimeter the relative acceptance for a $\pi^+ \rightarrow e^+ \nu_e \gamma$ decay, for instance, with $\phi > 0^\circ$ is at 86.2% while it reduces to 14.63% for $\phi > 30^\circ$. Since the $\mu^+ \rightarrow e^+ \nu_e \nu_\mu \gamma$ process is generated with a much higher probability by bremsstrahlung processes the relative acceptance for $\phi > 30^\circ$ reduces to 0.032%. A similar reduction can be observed for cuts on the photon energy. The acceptances for radiative decays, relative to the correspondent non-radiative decays, are plotted below in Figure 5-2.

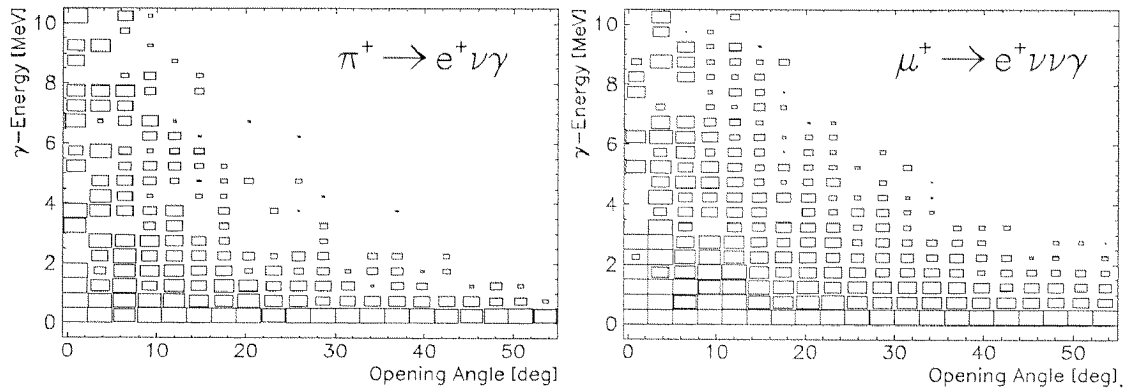


Figure 5-2 Photon energy plotted against the relative emission angle. The acceptance of the calorimeter then is plotted logarithmically in the projection of the z -axis. The plot for $\mu^+ \rightarrow e^+ \nu_e \nu_\mu \gamma$ (lower plot) looks similar; but is more pronounced at lower energies and angles. The acceptances are listed in Table 5-1 down below.

From this figure one can extract the relative calorimeter acceptances after applying kinematic cuts. It shall be summarized in Table 5-1.

Kinematic Cut	Acceptance in per cent relative to $\pi^+ \rightarrow e^+ \nu_e$	Acceptance in per cent relative to $\mu^+ \rightarrow e^+ \nu_e \bar{\nu}_\mu$
ϕ greater than	$\pi^+ \rightarrow e^+ \nu_e \gamma$	$\mu^+ \rightarrow e^+ \nu_e \bar{\nu}_\mu \gamma$
0°	86.2	99.97
5°	65.9	0.18
10°	54.5	0.16
20°	36.4	0.11
30°	27.0	0.09
40°	19.7	0.08
50°	14.6	0.03
E_γ greater than		
0 MeV	81.1	0.124
0.5 MeV	58.3	0.069
1 MeV	52.4	0.059
2 MeV	43.1	0.044
3.5 MeV	36.7	0.033
5 MeV	31.7	0.028
7 MeV	27.3	0.022
10 MeV	22.1	0.017

Table 5-1 Acceptances for radiative pion and muon decay modes for two kinematic cuts at different thresholds.

5.1 Clump Finding Algorithm

The clear relation between the photon energy and its emission angle with respect to the positron gave rise to the idea to trace radiative decays. An algorithm has been developed in order to identify energy distribution within the calorimeter to be deposited from either one or two particles. The energy distributions are referred to as 'clumps'. As observed in the simulations reported above, determination of separated clumps is possible only for certain kinematic regions, i.e. higher photon energies or higher opening angles, or both.

The clump finding routine combines two aspects. One is the identification of radiative decays and the other to accomplish an efficient energy summing. (The latter case is described in detail in chapter 7.)

In brevity: The routine shall be capable to decide about the number of tracks and its energies rather than blindly sum over modules that contains energy deposition.

The principles of the algorithm are as follows:

1. The fraction of the total calorimeter energy for each crystal exceeding the minimum energy threshold as well as the position are stored in a four-dimensional array.
2. The array is sorted with the highest energy placed first.
3. The first entry defines the centre and energy of the first cluster. Each succeeding entry joins this cluster if its angular distance from the cluster centroid is lower than the a chosen threshold value and the cluster centroid is recalculated. When the entry has a sufficient distance from the first cluster a new cluster is generated.
4. All remaining entries now either join the first or second cluster. The generation of further clusters is possible according to the threshold conditions.
5. In a second pass the generated clusters must be approved by repeating steps 1 to 4 with the cluster variables replacing the crystal variables. Here also additional criteria are defined, such as a threshold energy for a cluster or the requirement that a cluster must consist of two crystals at least. A cluster that fails the test is associated with the nearest cluster.

6. Finally, the routine saves the information on the cluster's energies, positions (θ, ϕ) and the allocation of the crystals contained in these clusters.

The free parameters have been adjusted using a simulation of $\pi^+ \rightarrow e^+ \nu_e \gamma$ in order to obtain a highly efficient clump identification. Despite the relatively good angular resolution of better than 4° it was found that the centres of two clumps have to be more than 15° apart to be distinguishable which is just above the average angular distance between two crystal midpoints. The clump finding efficiency is defined by the fraction of double tracks that were identified with the specified thresholds. Requiring a 'clump distance' of 20° and at least 10% of the deposited energy in the second cluster an efficiency of 99.8% is achieved. But, this high efficiency emerges at the cost of misinterpreted single tracks. This was found by a simulation of 70 MeV positrons that were distributed uniformly over the sphere, whereby an unacceptable misidentification of 19% was stated.

During the development process the simple approach of a distance threshold has been replaced by a threshold function. This function models the energy-angle relation. Interestingly, the curves of constant acceptance are similar to the energy deposition plot for monoenergetic positrons or photons. This plot presents the energy of a certain crystal divided by the overall energy deposition as a function of the angular distance¹ of that crystal to the shower centre is drawn (Figure 7-11). Now a function can be obtained which includes, for instance, 98% of the shower energy under the graph. The function

$$a \cos \left(\frac{\ln(q/1.394)}{18.85} + 1 \right)$$

gives the threshold constraint for a given value of q , where q is the fraction of deposited energy in the crystal of interest. A value above that threshold then indicates the presence of another clump. According to Oreglia [Ore88] the parameters of the threshold function can be related to the shower profile dimensions and the material dependent critical energy² E_c . The obtained parameters are a compromise of high efficiency for radiative decays, low contribution of misinterpreted single particle induced showers and good accuracy. An overall efficiency of 95.6% with a misidentification rate for single particle showers of 9.1% was the best compromise that could be reached.

With the above discrimination function and additional cuts for an energy fraction of 2% and an angle of 20° the applicability of the algorithm was tested by trying to resolve radiative events. During the 1996 beam period a 116 MeV/c π^+ beam was stopped in the above described plastic target. The $\pi^+ \rightarrow e^+ \nu_e$ trigger was investigated using an array of 44 crystals and a part of the hodoscope. Michel events were prescaled by a factor of 100 for a reduction of the count rate to an acceptable level.

In summing over the calorimeter modules it was required that a large fraction of energy was deposited within the innermost 18 crystals. In addition a positron signal in the hodoscope was required. The systematical errors due to the cuts are expressed through the determination of the acceptance, since the same computer code was used to analyze both data and simulation. The efficiency corrections and rounding errors are assumed to be precise to ± 2 counts.

¹ Angular distance means the angle between the crystal centre and the shower centroid obtained accordingly to Eq. 4.a.

² see section 7.4 for the definition

RUN	good Events	$\pi^+ \rightarrow e^+ \nu_e$ events	Photons >5 MeV	$\pi^+ \rightarrow e^+ \nu_e \gamma$ events	Misidentification correction -9.11%	Efficiency correction +(100-95.6)%	Total
200	159667	2928	868	52.4	-79.3	37.9	827
201	158828	2916	870	48.6	-79.5	38.0	829
202	157803	2794	878	61.0	-80.2	38.4	836
203	157771	2754	902	40.0	-82.4	39.4	859
204	159975	2727	920	48.6	-84.1	40.2	876
205	159545	2944	919	59.0	-84.0	40.2	875
206	157866	2909	893	37.1	-81.6	39.0	850
207	157257	2911	915	58.1	-83.6	40.0	871
208	158077	2823	894	51.4	-81.7	39.1	851
209	159097	2535	816	29.5	-74.6	35.7	777
210	159463	2613	892	33.3	-81.5	39.0	849
211	159100	2990	971	49.5	-88.7	42.4	924
212	158691	2757	926	38.1	-84.6	40.5	882
213	158547	2679	839	34.3	-76.7	36.7	799
214	159292	2723	926	41.9	-84.6	40.5	882
215	159684	2612	953	30.5	-87.1	41.6	908
216	159259	2651	961	30.5	-87.8	42.0	915
217	158481	2731	956	35.2	-87.4	41.8	910
218	158383	2749	897	36.2	-82.0	39.2	854
219	158638	2699	866	33.3	-79.2	37.8	824
220	158950	2611	947	30.5	-86.6	41.4	902
221	102242	1682	574	12.4	-52.5	25.1	547
Total	3436616	59738	19583	891.4±12.1	-1789.7	855.8	18649±15

Table 5-2 Listing of the $\pi^+ \rightarrow e^+ \nu_e$ runs of the 1996 beam period.

Out of 3.4×10^6 recorded events 18649 contained a well separated second cluster exceeding 5 MeV deposited energy. A correction for positron conversion in target and hodoscope was not applied, since the conversion probabilities for the positrons from $\pi^+ \rightarrow e^+ \nu_e$ and $\pi^+ \rightarrow e^+ \nu_e \gamma$ are nearly identical. A small difference due to the lower positron energy in the case of radiative decay does not contribute significantly to the overall error.

After applying cuts in order to select $\pi^+ \rightarrow e^+ \nu_e$ events [Law98] one finds the a total number of 59738 from which 891 were identified to be radiative. Using a simulation of radiative $\pi^+ \rightarrow e^+ \nu_e$ with the weightings accordingly to [Bry82], for the given detector geometry and used cuts an acceptance of 0.0393 for >5 MeV photons was determined. This has to be compared with the $\pi^+ \rightarrow e^+ \nu_e$ acceptance of 0.0622. An error of 12% comprising the statistics of accepted events and cut inefficiencies was determined. So one settles at a $\pi^+ \rightarrow e^+ \nu_e \gamma$ decay rate for photons larger than 5 MeV of $(2.90 \pm 1.2) \times 10^{-6}$. A calculation (Figure 5-3) gives 2.7×10^{-6} and therefore shows good agreement. This numerical calculation was successfully cross-checked with the results given in the publications listed in Table 5-3. The error of 1.2×10^{-6} comprises a statistical error of 0.9% and a systematical error (which also includes the uncertainty of the $\pi^+ \rightarrow e^+ \nu_e$ decay ratio of 4×10^{-7}) of about 40%. The relatively high number is to be explained due to the uncertainties in the determination of the acceptances and the number of normalization events; the systematical A notable reduction of the overall error is to expected with the PiBeta detector due to its large acceptance and a planned high number of events. Then a detailed comparison of simulated and measured events, especially in a kinematic region with lower probability, can be achieved. Additionally, the presence of the entire charge tracking modules in combination with an accurate determination of the number of $\pi^+ \rightarrow e^+ \nu_e$ events will reduce the systematic error.

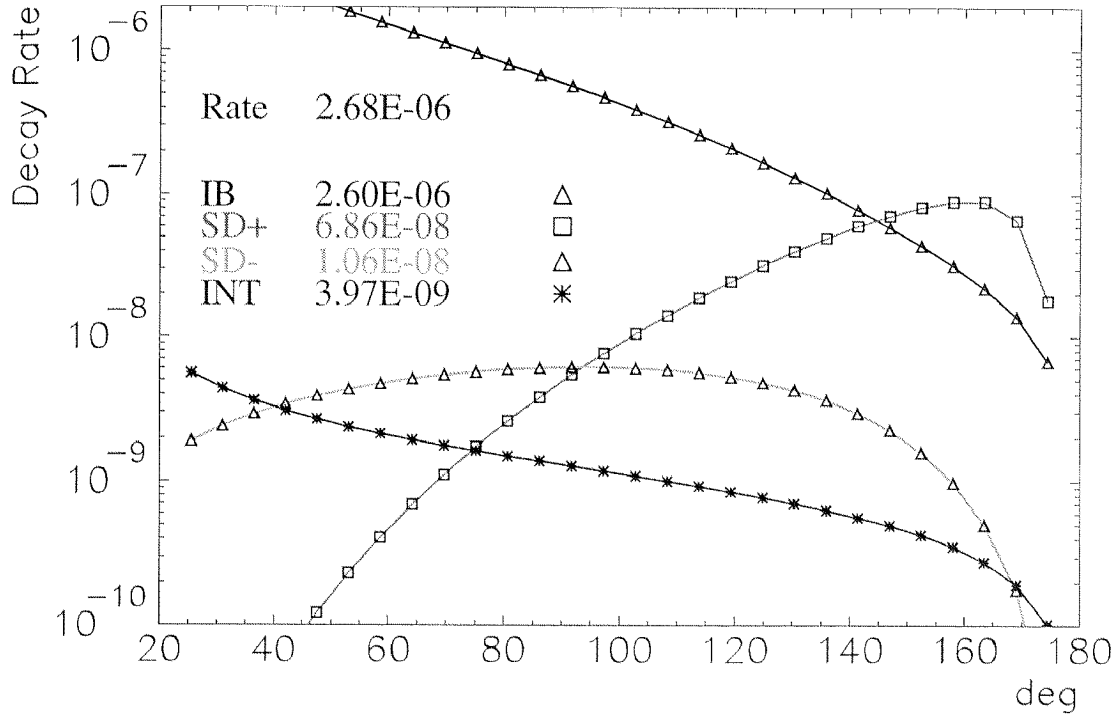


Figure 5-3 Plot of the terms contributing to the $\pi^+ \rightarrow e^+ \nu_e \gamma$ decay rate. (See [Bry82] for the formulas.) At lower emission angles mainly inner bremsstrahlung (IB) contributes to the decay rate. At higher photon energies or higher angles, respectively, structure dependent terms (SD) become more important. This source of radiative decay is attributed to pion form factors (F) which are divided into an axial term (F_A) and a vector term (F_V). The ratio of both terms is abbreviated as $\gamma = F_A/F_V$. Due to the undetermined sign of γ , SD splits into a positive (SD+) and negative (SD-) part. The values $\gamma=0.44$, $E_{\gamma, \min}=5$ MeV and relative angle $\theta_{e\gamma} > 20^\circ$ have been used. The numerical integration was verified by comparisons to the published values available (see Table 5-3 below). The interactive term (INT) which describes the correlation of SD and IB often can be neglected. (The PAW macro for the calculation of these terms is given in the Appendix.)

Publication	Decay Rate	limit 1	limit 2	$\gamma+$	$\gamma-$
[Dep63]	$(3 \pm 0.5) \cdot 10^{-8}$	$E_\gamma > 48$ MeV	$E_e > 48$ MeV	0.4	-2.1
[Ste78]	$(5.6 \pm 0.7) \cdot 10^{-8}$	$E_e > 56$ MeV	$\theta_{e\gamma} > 132^\circ$	0.44 ± 0.12	-2.36 ± 0.12
[Bay86]	not given	$E_\gamma > 36$ MeV	$170^\circ > \theta_{e\gamma} > 135^\circ$	0.52 ± 0.06	-2.48 ± 0.06
[Pob89] [Bol90]	$(16.1 \pm 2.3) \cdot 10^{-8}$	$E_\gamma > 21$ MeV	$\theta_{e\gamma} > 60^\circ$	0.41 ± 0.23	proposing F_T - term instead
this work	$(290 \pm 120) \cdot 10^{-8}$	$E_\gamma > 5$ MeV	$\theta_{e\gamma} > 20^\circ$	not determined	not determined

Table 5-3 Compilation of measurements of the radiative pion decay rate. The values cited for $\gamma+$ and $\gamma-$ are optional. Theory does not determine the sign of F_A/F_V .

After subtracting the of $\pi^+ \rightarrow e^+ \nu_e(\gamma)$ events, mainly $\mu^+ \rightarrow e^+ \nu_e \bar{\nu}_\mu(\gamma)$ remain in the data sample. Using a normalization to the number of ordinary Michel decay events¹, one obtains a rate of $(1.3 \pm 0.46)\%$ for $\mu^+ \rightarrow e^+ \nu_e \bar{\nu}_\mu \gamma$ for photons exceeding 5 MeV. Owing the high number of counts the statistical error is at 0.9%. The error in determine the acceptance was determined to be 12% by recording the number of weighted accepted events from a GEANT simulation. Rather than increasing the number of simulated events, the presence of a large acceptance calorimeter will decrease this source of uncertainty. Eckstein and Pratt [Eck50] give a BR for $\mu^+ \rightarrow e^+ \nu_e \bar{\nu}_\mu \gamma / \mu^+ \rightarrow e^+ \nu_e \bar{\nu}_\mu$ of 1.9% for photons exceeding the energy of 10

¹ The Michel trigger was prescaled by a factor of 100.

electron masses. We conclude that the right order of magnitude was obtained by simply applying the clump finding routine to our data. The main source contributing to a discrepancy is likely the presence of unsuppressed background, i.e., $\pi^+ \rightarrow \mu^+ \nu_\mu \gamma$.

With the application of the clump finding routine to the problem of radiative decays it was shown that a reconstruction of trajectories can be done reliably. The interesting physics behind the radiative decays can not be treated due to the low event statistics and the kinematic limitations of the 44-crystal apparatus. As can be seen in Figure 5-3 the structure dependent terms become prominent only at higher relative angles - and thus lower probability -, which would allow the determination of pion form factors or $\gamma = F_A/F_V$, respectively.

Further development is necessary to exclude more of the ambiguous events, labelled 'misidentified', because this results in a relatively high correction factor. A neural network algorithm is considered. Nevertheless, the obtained results lead to the conclusion that the PiBeta detector will be an excellent tool for a more precise determination of the $\pi^+ \rightarrow e^+ \nu_e \gamma$ decay rate, the more so since high statistics planned. The use of the full sphere furthermore enables a cut on the proper kinematic region and thus a more precise determination of F_A is possible¹. The vector form factor F_V accordingly to CVC Hypothesis is 0.0259 ± 0.0005 [PDG98]; in a PSI experiment [EGL89] it was determined to be $0.023^{+0.012}_{-0.013}$.

¹ The actual value is quoted as 0.0116 ± 0.0060 [PDG98].

6. The Panofsky Ratio

There are two main purposes in a measurement of the Panofsky Ratio (P). An accurate value of P allows the determination of the detector acceptance for photons in the energy regime of $m_{\pi^0}/2$ and, furthermore, P is directly related to the isovector pion-nucleon scattering length b_1 which is an important parameter for pion photoproduction cross sections. To motivate a re-measurement of P , in the first place the theory of πN scattering shall be introduced followed by the experimental set-up and the kinematics. Finally, the analysis of the Panofsky ratio measurement will be given in the subsequent chapter.

6.1 Theory

Ever since the days Yukawa described the nuclear forces with π exchange, in analogy to the photon exchange in EM interaction, pion studies have received major attention in nuclear physics. Early πN scattering experiments in the 1950s provided information about the unknown and poorly understood particle. For example Panofsky et al. [Pan50] obtained the π^- -mass¹ as a result of their πH scattering experiment. Furthermore they showed that only two reactions take place for a negative pion that comes to rest in hydrogen. The third allowed reaction $\pi^- p \rightarrow n\gamma\gamma$ is suppressed by the more favoured reactions with only two particles in the final state.

Panofsky et al. stopped low energy π^- in a high-pressure liquid hydrogen target and detected the resulting photons in a Geiger counter array. Knowing the pions to be bosons and considering conservation laws, the $\pi^- p$ system can result in either $n\gamma$ (radiative capture) or $n\pi^0$ – followed by $\pi^0 \rightarrow \gamma\gamma$ – (single charge exchange reaction). Since the stopped pions are temporarily bound in a hydrogen electron shell, they form pionic hydrogen. The original excited state loses energy through the emission of Auger electrons until the pion reaches the K-shell and finally react with the proton. The relative strength of both reactions thus is proportional to the lifetime of the 1s state of pionic hydrogen [Ras76]. The Panofsky ratio then is defined as

$$P = \frac{\sigma(\pi^- p \rightarrow \pi^0 n)}{\sigma(\pi^- p \rightarrow \gamma n)}.$$

Charge independence and time-reversal symmetry are required to allow a comparison of πN -scattering and pion photoproduction ($\gamma p \rightarrow \pi^+ n$ or $\gamma n \rightarrow \pi^- p$) data. Anderson and Fermi [And52] gave a theoretical calculation of the cross sections but could not match Panofsky's result ($P=0.94\pm 0.20$) [Pan50] with Steinberger's [Bis50] value for the pion photoproduction cross section σ_γ . They suggested a different value for P , therefore, and acknowledged the difficulties in the extrapolation of the σ_γ value to the threshold of vanishing kinetic energy.

With better statistics and improved detector resolution later experiments established the value $1.546(\pm 0.009)$ [Spu77] for P , which is in remarkable agreement with theoretical predictions [Ras76]. Besides the πN scattering length, P also gives information about the $s\bar{s}$ -quark contribution of the proton, the so-called Σ -term [Gas91]. The field of pion photoproduction is still highly active, since basic symmetries such as time reversal invariance, parity conservation and isospin invariance of the strong interaction can be tested [Mat97, Sig96].

¹ Their result was 140.6 ± 1.3 MeV.

6.1.1 Pion Nucleon Scattering

For the derivation of the relation between b_1 and P it is useful to describe SCX and radiative caption (RC) separately and make use of partial wave decomposition.

The pion-nucleon system represents a linear combination of isospin $T=3/2$ and $T=1/2$ isospin states, since nucleons form an isospin $1/2$ doublet and pions an isospin 1 triplet, which are broken by electric charge. The third isospin component T_z is attributed to the discussed particles as follows:

T_z	$T = 1/2$	$T = 1$
1		π^+
$1/2$	p	
0		π^0
$-1/2$	n	
-1		π^-

In combination they form either one of four $T_{3/2}$ or two $T_{1/2}$ states, where only the $T_z = \pm 3/2$ orientation directly can be attributed to

$$|\pi^+ p\rangle \text{ or } |\pi^- n\rangle, \text{ respectively.}$$

Looking at the two states of interest one finds

$$|\pi^- p\rangle = \sqrt{\frac{1}{3}}|T_{3/2}\rangle + \sqrt{\frac{2}{3}}|T_{1/2}\rangle$$

and

$$|\pi^0 n\rangle = \sqrt{\frac{2}{3}}|T_{3/2}\rangle - \sqrt{\frac{1}{3}}|T_{1/2}\rangle,$$

where the coefficients are the familiar Clebsch Gordan coefficients following the Condon-Shortley sign convention (see [Mat97] for example).

6.1.1.1 SCX s-wave Scattering

The SCX process can be well defined by elastic scattering at πN - threshold, where a pion plane wave e^{ikz} is scattered by a solid body with the scattering amplitude $f(\theta)$ and transforms into the deflected wave e^{ikr}/r

$$f(r) = e^{ikz} + F(\theta) \frac{e^{ikr}}{r},$$

where θ represents the scattering angle. Or in a different form (following [Che57]), when the pion wavefunction is denoted as $\pi(q)$:

$$F(\mathbf{q}', \mathbf{q}) = \langle \pi(\mathbf{q}') | f | \pi(\mathbf{q}) \rangle,$$

where f contains the phase shift δ via

$$f = \frac{1}{|q|} \exp(i\delta_l) \sin(\delta_l).$$

Here q and q' represent the pion momenta before and after scattering.

As is well known the differential cross section is given by $d\sigma/d\Omega = F(\mathbf{q}', \mathbf{q})^2$. It is useful to perform a partial wave decomposition. Then F becomes

$$\sum_{l=0}^{\infty} (2l+1) \left[f_{l^+} \hat{Q}_{l^+} + f_{l^-} \hat{Q}_{l^-} \right] P_l(\cos\theta), \text{ where } \hat{Q}_{l^\pm}$$

are the angular momentum $J=l\pm\frac{1}{2}$ projection operators for a given orbital momentum l and $P_l \cos(\theta)$ Legendre polynomials.

Since the pion is captured at rest we can neglect all orbital momenta other than $l=0$ (s-waves). So

$$\hat{Q}_{l^+} = \frac{l+1+l\cdot\sigma}{2l+1} \text{ becomes 1 and } \hat{Q}_{l^-} = \frac{l-l\cdot\sigma}{2l+1} \text{ 0;}$$

σ is the pion spin position.

In addition one should take the isospin decomposition into account and make use of the isospin projection operators

$$\hat{P}_{3/2} = \frac{1}{3}(2 + \tilde{t} \cdot \tilde{\tau}) \text{ and } \hat{P}_{1/2} = \frac{1}{3}(1 - \tilde{t} \cdot \tilde{\tau}) \text{ with } \tilde{t} \cdot \tilde{\tau} = t_1\tau_1 + t_2\tau_2 + t_3\tau_3,$$

where t represents the nucleon isospin and τ the pion isospin.

Thus, \hat{P} projects the total isospin $T=1/2$ and $T=3/2$ states out of the πN system. For example:

$$\begin{aligned} \hat{P}_{1/2} |p\pi^- \rangle &= \frac{1}{3} (1 - \tilde{t} \cdot \tilde{\tau}) |p\pi^- \rangle \\ &= \frac{1}{3} \left(|p\pi^- \rangle - \left[\frac{1}{\sqrt{2}} |n\pi^0 \rangle + \frac{-i}{\sqrt{2}} |n\pi^0 \rangle - |p\pi^- \rangle \right] \right) \\ &= \sqrt{\frac{2}{3}} \left(\sqrt{\frac{2}{3}} |p\pi^- \rangle - \sqrt{\frac{1}{3}} |n\pi^0 \rangle \right) \\ &= \sqrt{\frac{2}{3}} |T_{1/2}, T_Z = -\frac{1}{2} \rangle \\ \hat{P}_{3/2} |p\pi^- \rangle &= \sqrt{\frac{1}{3}} \left(\sqrt{\frac{1}{3}} |p\pi^- \rangle + \sqrt{\frac{2}{3}} |n\pi^0 \rangle \right) \\ &= \sqrt{\frac{1}{3}} |T_{3/2}, T_Z = -\frac{1}{2} \rangle \end{aligned}$$

The scattering amplitude now simplifies to

$$\sum_{T=\frac{1}{2}, \frac{3}{2}} \hat{P}_T f_{0^+}, \text{ since } P_0(\cos\theta) = 1.$$

Finally, one can calculate the cross section σ for πN scattering.

In the case of $\pi p - \pi p$ elastic scattering one obtains

$$\sigma_0 = 4\pi \left\langle p\pi^- \left| \lim_{q \rightarrow 0} \left(\hat{P}_{1/2} f_{\frac{1}{2}, 0^+} + \hat{P}_{3/2} f_{\frac{3}{2}, 0^+} \right) \right| p\pi^- \right\rangle^2 = 4\pi \frac{1}{9} (2a_1 + a_3)^2$$

and analogous for SCX

$$\sigma_{0, \text{SCX}} = \sigma(p\pi^- \rightarrow n\pi^0) = 8\pi \frac{1}{9} \frac{(a_3 - a_1)^2}{2},$$

having denoted the scattering lengths a_1 for $T=1/2$ and a_3 for $T=3/2$. Often $b_1 = \frac{1}{3}(a_3 - a_1)$ is used, as well.

6.1.1.2 Pion Photoproduction

Usually RC is characterized by its time reversed process: photoproduction of pions ($\gamma N \rightarrow \pi N$). This process can be described successfully by a partial wave decomposition of the photon wave function. In Dirac notation the matrix element T_{fi} , which represents the transition operator for the final (pion-nucleon) and the initial (photon-nucleon) state, can be written as

$$\langle f | \sum_{i=1}^N F_i \Theta_i | i \rangle,$$

where F consists of a linear combination of the photon multipole amplitudes and Θ contains kinematic and spin information. At threshold¹ only

$$F_1 = \sum_{l=0}^{\infty} (lM_{l^+} + E_{l^+}) P'_{l+1}(x) + [(l+1)M_{l^-} + E_{l^-}] P'_{l-1}(x)$$

contributes [Che57]. With l representing orbital angular momentum M_l and E_l are the magnetic and electric transition amplitudes, respectively. Then the differential cross section becomes

$$\frac{d\sigma}{d\Omega} = \frac{q}{k} |F_1|^2,$$

where $\frac{q}{k}$ is the ratio of the absolute photon over pion momentum.

Due to the p^3 momentum dependence of the p-wave amplitudes (p^5 for E_{2^-} , respectively) only the s-wave term is significant in our case, since the π^- is captured at rest. This leads to

$$F_1 = 4\pi E_{0^+}.$$

Then $E_{0^+}^{\text{thr}}$, the threshold amplitude of pion photoproduction, is defined via

$$\frac{k}{q} \sigma_{0,\text{RC}} = 4\pi (E_{0^+}^{\text{thr}})^2 \quad [\text{Kov97}].$$

Hence, the electric dipole amplitude $E_{0^+}^{\text{thr}}$ with $l_{\pi}=0$ and total spin $j=1/2$ fully describes the pion photoproduction cross section (and therefore the radiative capture, as well).

The ratio of the fundamental processes for a π^- stopping in a H-nucleus then consistently is given through s-wave pion scattering at threshold and calculates to

$$\frac{\sigma_{0,\text{SCX}}}{\sigma_{0,\text{RC}}} = \frac{1}{9} \frac{k}{q} \frac{(a_3 - a_1)^2}{|E_{0^+}^{\text{thr}}|^2} = P.$$

Hence, knowing $E_{0^+}^{\text{thr}}$, the πN scattering length b_1 can be obtained directly by measuring the Panofsky ratio.

Using

$$9 \frac{q}{k} = 9 \frac{p_{\gamma}}{p_{\pi^0}} = \frac{E_{\gamma}}{\sqrt{E_{\pi^0}^2 - m_{\pi^0}^2}} = 9 \frac{M^2 - m_{\pi}^2}{\sqrt{(M^2 + m_{\pi^0}^2 - m_{\pi}^2)^2 - 4M^2 m_{\pi^0}^2}} = 41.535$$

and $P=1.546$ [Spu77], the actual value is $-0.253/m_{\pi}$. $M = m_{\pi^-} + m_p - B_{1s}$ has been used with the correction for the binding energy of pionic hydrogen $B_{1s}=0.00324$ MeV.

6.2 Experimental Set-up

The goals of the 1997 beam period with a subset of the PiBeta detector were threefold: i) an energy calibration with ~ 70 MeV photons and positrons, ii) the determination of the overall acceptance of photons of this energy and iii) a precise measurement of the Panofsky ratio. The following shall concentrate on the measurement of the Panofsky ratio. With a π^- -beam impinging a liquid hydrogen target (LH2) the πN reactions results in the above described final states through either charge exchange

¹ Threshold here means vanishing kinetic energy, namely $p_{\gamma} \equiv m_{\pi}c$, where p_{γ} is the photon momentum.

reaction or radiative capture. The resulting photons of particular energy are to be detected in the CsI array. In order to select a certain photon energy out of the distribution that results from the π^0 decay into two photons, one photon has to be tagged. An array of 64 NaI crystals therefore was placed opposite to the CsI array.

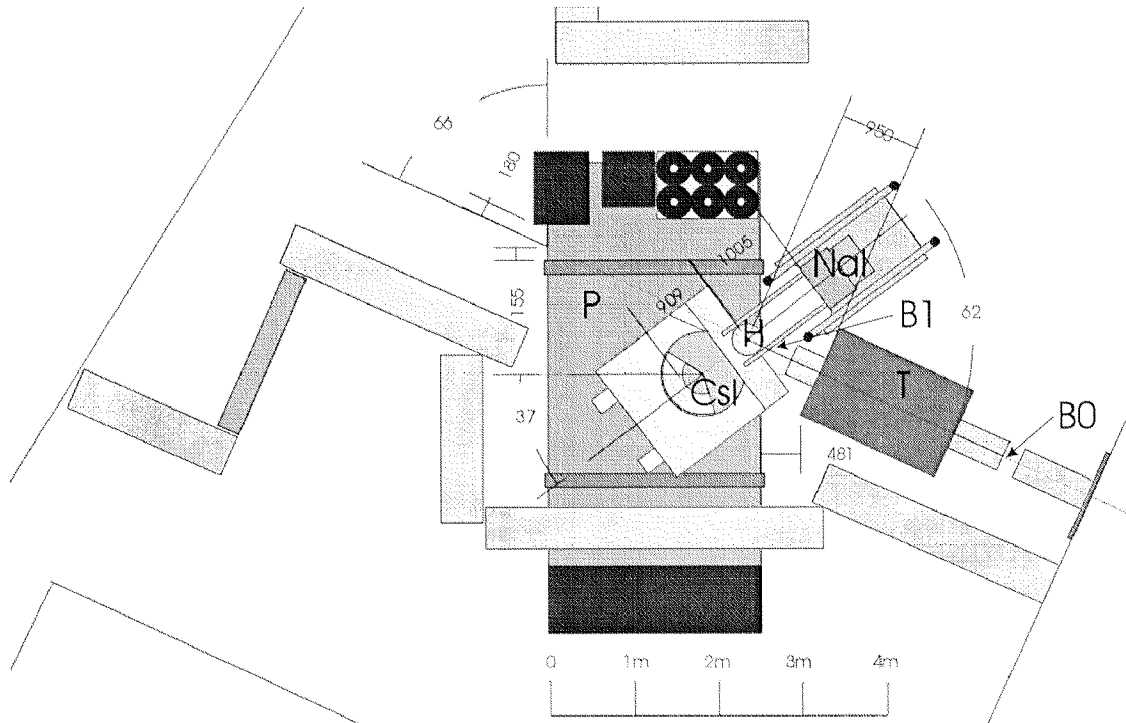


Figure 6-1 Pictures of the area layout for the measurements with the LH2 target. The target including cryostat and support is located at "H" directly followed by the NaI-wall. At "T" the set of three quadrupole lenses is shown. Beam up, in the gap between the vacuum pipes, the beam counter B0 was located. On the platform ("P") one sees the CsI array ('swing') mounted on a pivot.

The negative pion beam was optimized for high rate and low contamination of leptons. As in the final set-up, also to be located in the $\pi E1$, a momentum of 116 MeV/c, was chosen (see chapter 2). In the first focus directly after the beam enters the area a 0.1 cm thick plastic scintillator was located to register beam particles. It was followed by a quadrupole triplet that imaged the focus onto the target. A second beam counter (B1) of 1 cm thickness was placed right in front of the LH2-target vacuum housing to provide timing information before the pions stop in the target. The combination of both counters was used for beam particle discrimination and as a veto detector for scattered particles and in-flight-decays. We achieved a π^- stop rate in the target of $10^5 \pi^-/s$.

The target consisted of a LH2 vessel plus a surrounding vacuum cylinder. The target vessel was a 150 μ m capton foil cylinder, 10 cm long and 4 cm in diameter. Liquid hydrogen was filled in the vessel through an iron pipe that entered the flange on which the capton vessel was mounted. In front of the vessel 2 cm of CH_2 was inserted to degrade the pions such, that they entirely stopped within the liquid hydrogen. Another 6 mm of carbon was added as a degrader in front of B1. The optimal thickness for the degrader was obtained by checking the trigger rate using different degrader thicknesses. The stopping distribution of the pions in the target was modelled using a GEANT simulation of the target (section 7.5.1). The vacuum housing had a diameter of 120 mm and was made of 1 mm thick aluminium. It was enclosed in a 190 μ m mylar foil to allow the presence of two windows facing the calorimeters. These windows minimized absorption, pair conversion and scattering of the photons.

6.2.1 The Calorimeters

6.2.1.1 The CsI Array

The CsI-array used in the measurement was a subset of the final PiBeta detector holding 44 CsI crystals, which defined a fifth of the whole CsI calorimeter. It covered 72° in polar (θ) and 144° in azimuthal (ϕ) angle. The goal of the measurement was to get a reliable test of the performance of the sphere. The mounting procedure used was the same as planned for the final assembly. The alignment of the crystals was critical, because gaps between crystal sides would decrease the energy resolution and increase the error in the determination of the detector acceptance. The steel cone piece (see sect. 2.3.7 and Figure 6–2) defined the alignment in both θ and ϕ direction. For the radial alignment a ball with a rod was used defining the centre of the calorimeter and the 260 mm distance of the crystal's surface to the centre (see Figure 4–2). The choice for the 44 out of 240 crystals was arbitrary in order to allow a realistic prediction of the overall energy resolution for both 68 MeV positrons and 69 MeV photons.

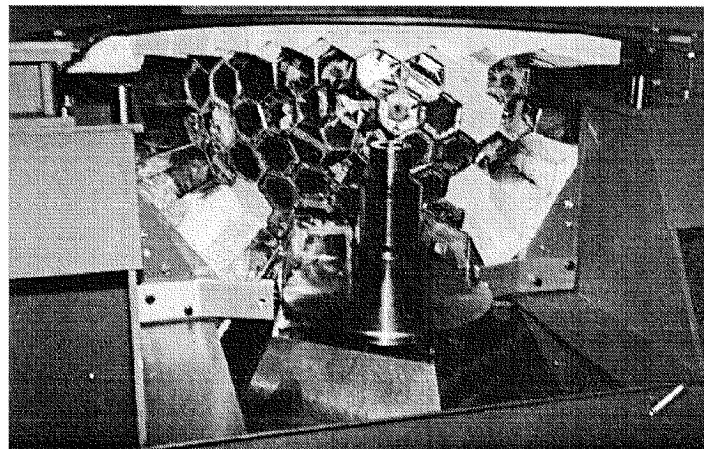


Figure 6–2 Array of 40 CsI crystals on the 'swing' forming a fifth of a sphere. 44 crystals were used in the 1997 beamtime period.

The CsI array with the swing was surrounded by a thermal house made of 4 cm thick styrofoam. In order to limit pion beam absorption the front shielding only consisted of two cardboard sheets of 300 μm thickness each.

In order to probe several parts of the CsI array it was mounted on a swing that was mobile in theta- and phi-direction. The pivot coincided with the centre of the sphere and with the reaction centre. The array had to be moved out of the central point for measurements involving the LH2-target to allow the mechanical support structure to fit in.

6.2.1.2 The NaI-Wall

The photon-tagging detector consisted of 64 rectangular ($406 \times 63 \times 63 \text{ mm}^3$) NaI Polyscin[®] modules [Bay88]. It was designed for high efficiency detection of intermediate energy photons. The 406 mm of NaI represents 15.7 radiation lengths. The NaI-modules are assembled to form an 8x8 array that is encased in an air-tight container. Each module is optically isolated against the others with one layer of reflecting material surrounded by aluminized mylar foil. They are read out by Philips PM2202 photomultipliers that are coupled through 60 mm long light guides. Each side is enclosed in 19 mm of aluminium except for the front face. In order to limit absorption the front face is made of a 0.5 mm steel sheet that is glued on 20 mm of styrofoam for insulation. Bay et al. could achieve a resolution of 7% FWHM at 70 MeV.

In order to veto against lateral shower losses, the NaI-wall was electronically subdivided in two parts. An array of the central 6x6 crystals formed NaI_{inner} and a ring of the 28 outermost modules formed NaI_{outer}.

6.2.1.3 Trigger

A coincidence of the signals of the beam counters B0 and B1 was used to discriminate against beam electrons, since pions and electrons are well separated by a time-of-flight difference of 6 ns. The B0*B1 coincidence then was fed into the MTU.

The CsI calorimeter trigger scheme follows the description of superclusters in chapter 2. Groups of 6 to 9 crystals were generated and the correspondent analog signals from the PMT voltage divider were added using the UVA 125 summing modules. The 10 resulting clusters built the supercluster logic, which also was fed into the MTU. The so-called 'high' threshold was set at about 2 MeV.

In order to build the NaI trigger, the linear sum for the NaI_{inner} and NaI_{outer}-branch was generated separately with the UVA 125 summing modules. A valid event required a signal from the NaI_{inner}-Sum which was vetoed if NaI_{outer}-Sum exceeded the chosen threshold.

The trigger during the runs with the LH2 target was threefold to allow two tasks at the same time. A coincidence between B0,B1, NaI- and CsI-calorimeter (see Figure 6-3) was built to detect simultaneously the two photons from the π^0 -decay in both calorimeters. In addition, the so-called 'single-arm' trigger was generated. It required the presence of one photon in either detector and thus registered the two competitive πN reactions. This trigger mode was prescaled to allow a high counting rate for the coincidence mode. The main trigger consisted of a coincidence between the two beam counters and the two arms of the detector. In order to avoid RC events in the coincidence mode, the thresholds for both detectors were set well above 10 MeV. The coincidence between both detectors also was used for calibration, since the π^0 -energy adds up to 137.86 MeV.

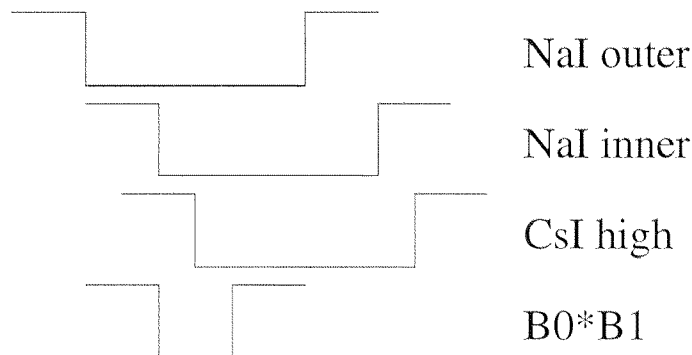


Figure 6-3 Trigger logic for the measurement of the Panofsky ratio (CsI high defines the timing)

The selection of the trigger of interest for data analysis was available through the output pattern of the MTU which was stored along with the energy and timing information. Furthermore the temperature was monitored continuously at six positions within the CsI thermal house.

6.3 Kinematics

The π^- , when entering the LH2-target, loses energy due to collisions with orbital electrons. It then can be captured in an outer orbit which leads to an excited π^- -H state. The system deexcites by the emission of Auger electrons until the lowest quantum state is reached. While it takes approximately 10^{-10} - 10^{-9} s to form a K-shell pionic hydrogen, after another $\sim 10^{-14}$ s either $n+\pi^0$ (SCX) or $n+\gamma$ (RC) results.

The invariant mass of the π^- -H system amounts to¹

$$M = m(\pi^-) + m(p) - B_{1s} = 1077.8390.$$

For RC one obtains the energies $E(\gamma) = 129.404$ MeV and $E_{\text{kin}}(n) = 8.8695$ MeV. For SCX the neutron has no more than 0.4183 MeV kinetic energy while the π^0 has a total energy of $E(\pi^0) = 137.8562$ MeV. The π^0 with a velocity β of 0.20333 instantaneously decays into 2 photons. The photon energy has to be calculated in the laboratory frame using

$$E_\gamma = \frac{m_{\pi^0}}{2} \gamma (1 + \beta \cos(\varphi_{\pi^0})),$$

where φ_{π^0} is the angle between the π^0 -direction and a fixed z-axis. Since the probability for each angle φ_{π^0} is equal because pions are spinless, this results in a box distribution with photon energies between 54.91 MeV and 82.94 MeV. When both photons share the same energy $E_{\pi^0}/2 = 68.928$ MeV they have the lowest possible opening angle of $\varphi_{\gamma,\text{min}} = 156.537^\circ$ as seen in Figure 6-4. Since the differential solid angle $d\Omega = -2\pi d(\cos(\varphi))$ is proportional to the number of emitted particles the frequency of emitting angles can be computed using $d\cos(\varphi)/d\cos(\varphi') = \sin(\varphi')/(d\varphi'/d\varphi)$, where φ is the angle of the neutral pion with respect to the z-axis and φ' the relative angle of the two photons. φ' and φ are related using the kinematic formulas for emitting angles of the individual photons, hence

$$\varphi' = \text{atan}\left(\frac{\sin\varphi}{\gamma(\beta + \cos\varphi)}\right) + \text{atan}\left(\frac{\sin\varphi}{\gamma(\beta - \cos\varphi)}\right).$$

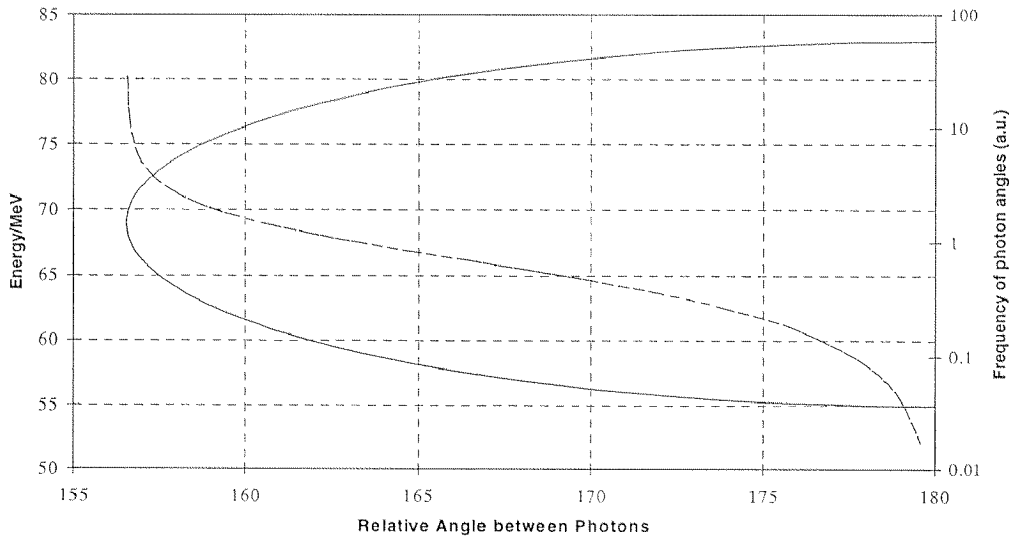


Figure 6-4 Kinematics and frequencies for the π^0 -decay in charge exchange reaction at rest. The solid line shows the photon energies as a function of their relative angle while the dashed curve reflects the probability for a distinct relative emitting angle. See text for details.

Since the photon energies of the two reactions of interest are well separated, one can clearly distinguish SCX and RC with an electromagnetic calorimeter of high energy resolution. The counts under the π^0 distribution divided by the counts under the RC peak then will give twice the Panofsky ratio (since the probability for detecting one of the two photons from π^0 -decay is twice as large as for a single photon from RC).

¹ B_{1s} , the binding energy of pionic Hydrogen, contributes with 0.00324 MeV

6.4 Background Processes

Several background processes could limit a precise determination of the Panofsky ratio. In order to obtain the ratio of events that originates from either SCX or RC the absence of other particles in the eligible energy region is mandatory. The following list summarizes possible sources of background and the methods of discrimination.

- High energy neutrons of about 70 MeV would be produced when a π^- is captured by aluminium or other material. They can be identified by the time-of-flight of the particles entering the calorimeter. In the present experiment π^- beam particles pass only through low Z material, mylar for instance. Hence, only scattered π^- that would be captured by the LH2-target housing or the cryostat rods would contribute to that background
- The presence of deuterium in the LH2-target would result into an excess of RC-events and low energy neutrons. For this reason high purity hydrogen was used in the target.
- A low energy background resulting from pair conversion in the target vessel or in air can not be avoided entirely. The electrons and positrons are vetoed by using the plastic scintillator hodoscope array. Since they also can undergo bremsstrahlung low energy photons could enter the calorimeters. This source of background can only be reduced by comparing the low-energy lineshape with the simulation.
- After the magnet triplet the π^- travels about 30 cm through air. This can give rise to in-flight SCX. The contribution of in-flight reactions would result in an error for the determination of the detector acceptances, since the reaction points are unknown. Hence, the B1-counter was positioned directly in front of the target's entrance window¹.
- Conversion can take place resulting in the modified reactions $\pi^-p \rightarrow e^-e^+n$, $\pi^0 \rightarrow e^-e^+\gamma$, respectively. Whether this results from structural effects or photo reaction with H_2 is indistinguishable; however this leads to a multiplicative correction of 0.999 for both reactions [Coc61].
- Scattered beam pions have a chance to enter the CsI array with a kinetic energy of 40 MeV at most.
- Background from decaying muons succeeding $\pi^- \rightarrow \mu^- \nu_\mu$ decay can be neglected, since the slowdown and capture process of the π^- in H_2 is three orders of magnitudes faster (see section 6.3 and [Pan50]).

¹ The LH2-target vessel is evacuated

7. Analysis of the Panofsky runs

The Panofsky ratio measures the relative probability of the two fundamental processes in pion capture of the nucleon. An efficient calorimeter will detect either the 129.4 MeV photon from RC or one of the photons from the π^0 decay that follows SCX. In order to achieve good energy resolution and low background contamination a number of steps have been carried out.

For each channel its offset or 'pedestal'-value was determined continuously during the beam period by applying a random trigger. The pedestal value had to be subtracted for each channel separately. The width of the pedestal peak is determined by the amount of electronic noise present. Most of the noise was coherent regarding several channels. The subtraction of coherent noise is referred to as secondary pedestal correction. After applying this correction a threshold value was obtained to separate electronic noise from valuable energy information.

As mentioned above, intercalibration effects contribute to the constant term of the energy resolution. Since an electromagnetic shower develops over several crystals, the crystals have to be cross-calibrated against each other. The so-called gain matching was applied in a two step approach. In the first place the sum of both calorimeters defined the invariant mass of the decaying π^0 . For each crystal this energy information was adapted such, that the peak position for each channel was equalized. In a second step, shower leakage also was taken into account. To this end the individual spectra for each crystal were obtained by simulation and compared with the measured spectrum.

Shower leakage also causes the presence of a tail to the left side of a peak. In order to reduce the extension of that tail, that is to minimize the contribution of the tail of the 129 MeV peak under the SCX distribution, a cut limiting the deposited energy in the outermost crystals was implemented.

Further background reduction had to be achieved off-line. Due to a high rate some 8 MeV neutrons from radiative capture fell into the time window of the photons. Furthermore scattered beam pions reached the CsI-calorimeter. A cut on the timing spectrum of the beam counter reduced these sources of background notably.

The background and the implications of the cuts were studied using a GEANT simulation of the LH2 target. Furthermore the detector acceptances for photons of different energies were determined using the same simulation.

Finally, a clean photon spectrum with two well-separated photon distributions was obtained. Applying fit functions to these distributions the integrals were calculated and such the Panofsky ratio was obtained.

7.1 Secondary Pedestal Correction

The ADC pedestals were evaluated during and recorded after each data taking run. To this end a clocking device started periodically the ADC gated readout during the data runs. A continuous control of the electronic noise was ensured by this. The pedestal values were written into a database along with other run information such as temperature, detector high voltage values, trigger rates, etc.

Experience from earlier beam periods [Bro96] showed that there occurs coherent noise between calorimeter channels (and among other modules, as well). Possible sources of common noise are induced currents in flat ribbon cables, commonly used NIM and CAMAC modules or patch panels. The on-line pedestal information was used in the common subtraction of that noise. For this 'secondary pedestal subtraction'(SPS) the minimum value of an ADC entry was evaluated. (This was done separately for the combined modules, as there are the CsI-array, the Hodoscope strips and the NaI-wall.) Then the average secondary pedestal position of all channels not exceeding 10 ADC channel numbers (20 for the NaI) above the minimum was computed and subtracted from all ADC values.

Rather than using all channels of a detector, a division into subgroups was more suitable. For a reliable common noise suppression the correlation coefficient r between two channels at a time was calculated using

$$r = \frac{\sum_{i=1}^N x_i y_i}{\sqrt{\sum_{i=1}^N x_i^2 \sum_{i=1}^N y_i^2}},$$

where N is the number of entries under the pedestal peak and x_i and y_i , the i -th pedestal entries for crystals x and y , respectively. Since this led to some ambiguous results, the idea to group together all channels with high r was not feasible. Instead, initially groups of 16 were generated because of the fact that a LeCroy Fastbus ADC holds 5 groups of 16 channels. Then members of these groups with a poor r concerning other group members or with suspicious looking pedestal peaks (double peaks for instance) were excluded. For those channels the correlation coefficient r helped again to find the appropriate members to group with. The minimum number of members in a group was set to six. Too few members in a group do not allow reliable SPS anymore, since no average common noise level could be calculated if all members of a group had reported a valid hit.

After applying SPS, the average noise contribution to the CsI-array was 0.1 ± 1.44 ch. (4 ± 62 keV) and for the NaI-wall -0.31 ± 4.23 ch. (13 ± 179 keV). The higher noise level for the NaI channel results from a wider ADC-gate due to the slower decay time of the scintillation light. (Those values were also implemented in the GEANT simulation.)

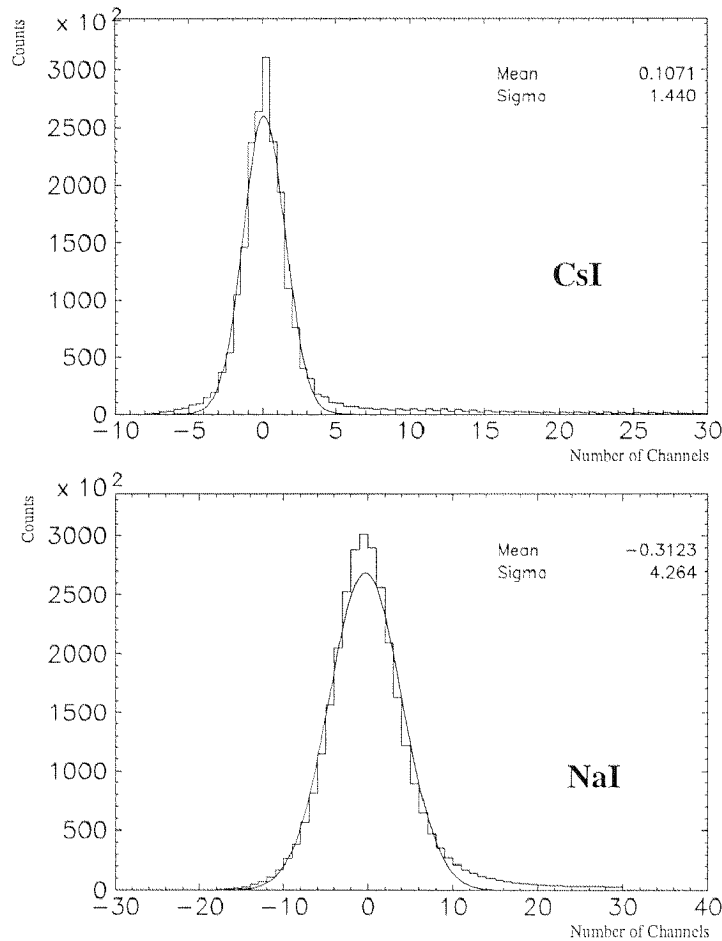


Figure 7-1 The upper plot shows the logical OR of the CsI modules with a content of less than 30 channels, while the lower plot shows the same for the NaI array. The width of the pedestal peaks reflects the noise distribution to the array. A noise threshold of 3.5 sigma then gives a cut at 5 ch. for the CsI and 15 ch. for the NaI array. This can be additionally confirmed by looking at the energy resolution as a function of noise threshold energy.

With these pedestals the necessary noise threshold was established, needed for energy summing and gain calibration. To this end the peak position of the sum of all CsI-modules exposed to 70 MeV positrons was plotted against the noise threshold; the secondary axis of Figure 7–2 shows the same for the FWHM. Theoretically the value of the peak position should reach a plateau as soon as the threshold value excludes fluctuations due to noise. When low energy contribution becomes excluded, the peak-position will drop continuously.

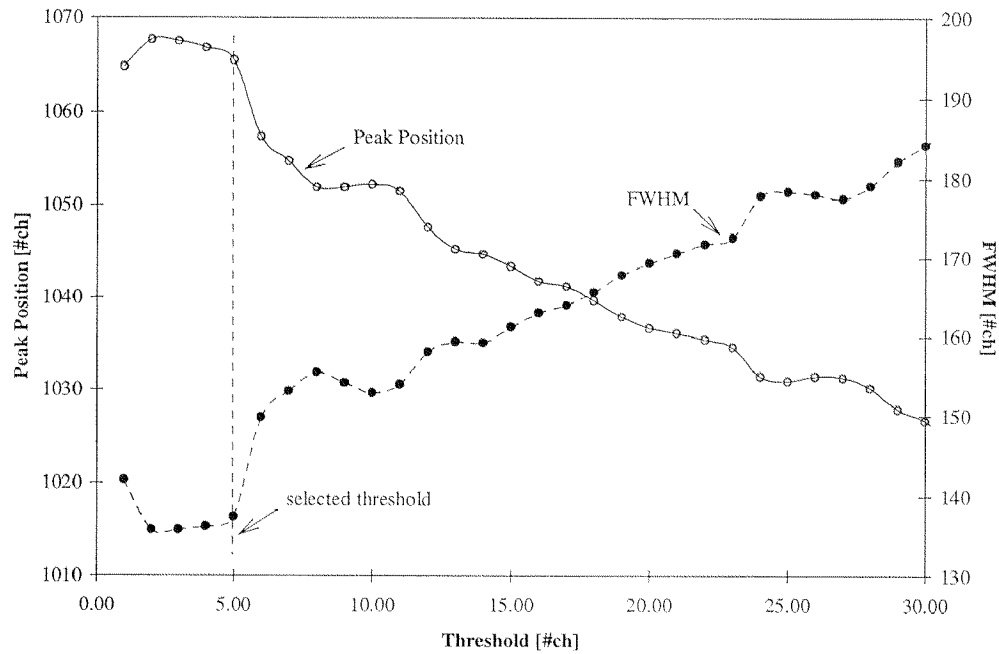


Figure 7–2 Evaluations of the Noise Threshold. (See text for explanations.)

A distinct maximum for the peak-position was found at a threshold of 3 channels, where the peak width also is at minimum, which corresponds to 2σ of the averaged noise peak. To be on the safe side a threshold of 3.5σ was chosen which leads to 5 channel numbers for the CsI and 15 for the NaI. Additionally, individual thresholds were implemented for each channel, but no further improvement could be reached.

7.2 Gain Matching

Since an electromagnetic shower will spread beyond the dimensions of an individual CsI crystal, intercalibration effects and energy losses play an important role for the energy resolution. Optimizing the energy resolution requires a precise gain matching and proper cluster summation. On top of this the knowledge of the differences between positron initiated showers and photon initiated showers - and hence the response function of the calorimeter - is critical for the accuracy of our experiment.

7.2.1 On-line Gain Matching

Prior to data taking the gains of the individual channels of both calorimeters were equalized. This was done in an iterative way using the 129.4 MeV photon peak. With a 12-bit ADC channel full scale of 4096, a position at 3000 was chosen to provide sufficient dynamic range. The actual peak position of the i -th detector module when $x_i = \max(x_j)$ was determined by building the sums

$$\sum_{j=1}^N x_j - p_j; 1 \leq j \leq i \leq N, (7.a)$$

where N is the number of modules (44 in the case of the CsI-array and 64 in the case of NaI-wall), x_j the channel number of the j -th module and p_j the pedestal value. The obtained peak was fitted using a Gaussian curve with an exponential tail. For each channel the necessary decrease or increase for the supply voltage was calculated and applied on demand. After about five iterations, a similar peak position for each channel was achieved, as well as an improved energy resolution.

7.2.2 Off-line Gain Matching

Although the gains were matched on-line, a refined gain matching method was applied off-line to achieve a correct calibration of both calorimeters and to account for slight gain changes over time. Off-line gain matching was done in two steps. First, each channel of both arrays was adjusted to the same peak position by adding the energy of the photons detected coincidentally in both detectors. Then individual spectra were generated with the help of GEANT simulations (see below) and used as a reference. This step was necessary to take into account energy losses at the outermost modules.

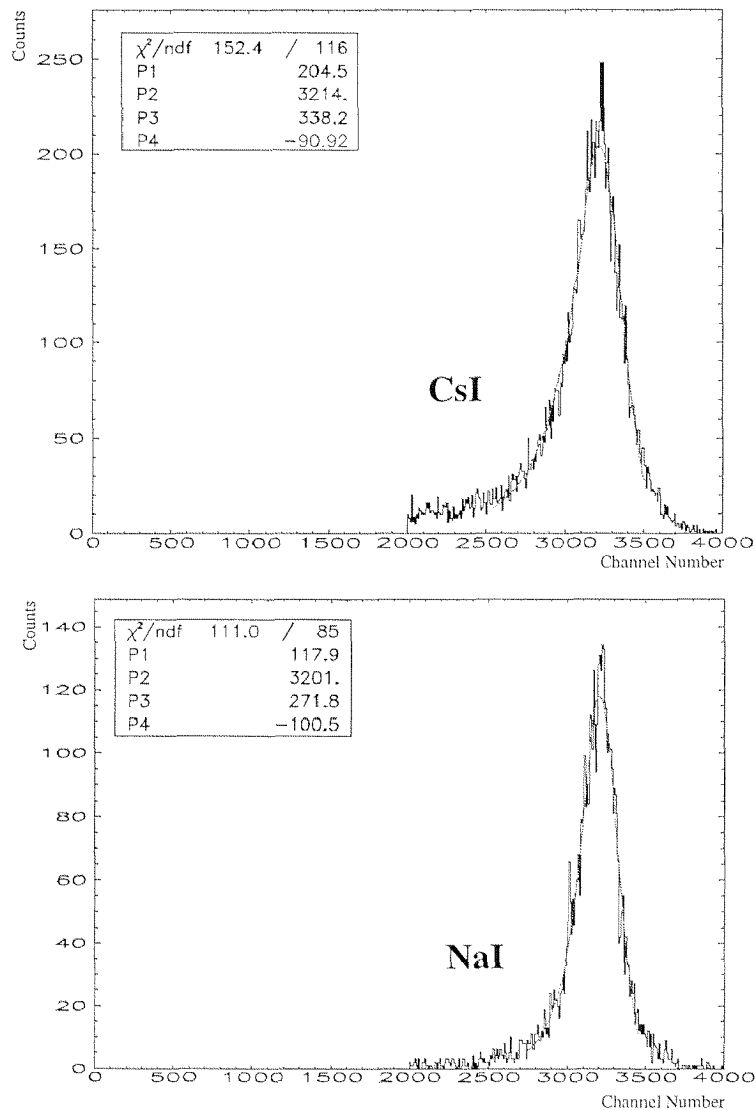


Figure 7-3 Typical π^0 spectrum (max. in CsI#24); cut-off at # 2000, correspondingly to 86 MeV.

Figure 7-4 Typical π^0 spectrum (max in NaI #100); cut-off at # 2000.

The gain matching routine was programmed to shift the i -th sum spectrum to channel 3206, the equivalent to the energy of the π^0 (137.8 MeV). Then summing accomplished in using equation 7.a, but having $N=108$. The spectrum was cut arbitrarily at channel 2000, since the peak position was the only

relevant information. Due to the high numbers of channels to add up, more iteration compared to the on-line gain matching was necessary. The actual values of the π^0 -peak were determined in the first pass and a software gain factor was calculated. In addition the pedestals were fitted with a Gaussian and then readjusted in the database, if necessary. In subsequent iterations the software gains of individual modules were adjusted.

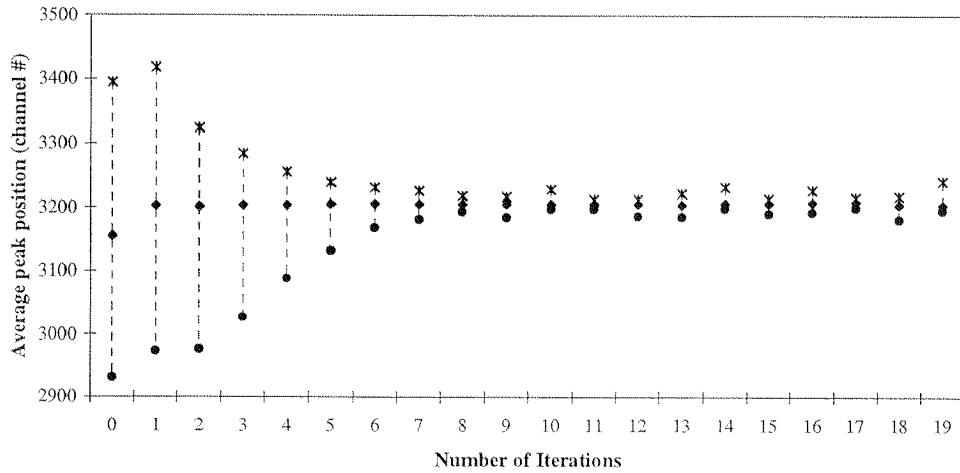


Figure 7-5 Average peak position and high-low lines for all (CsI and NaI) channels.

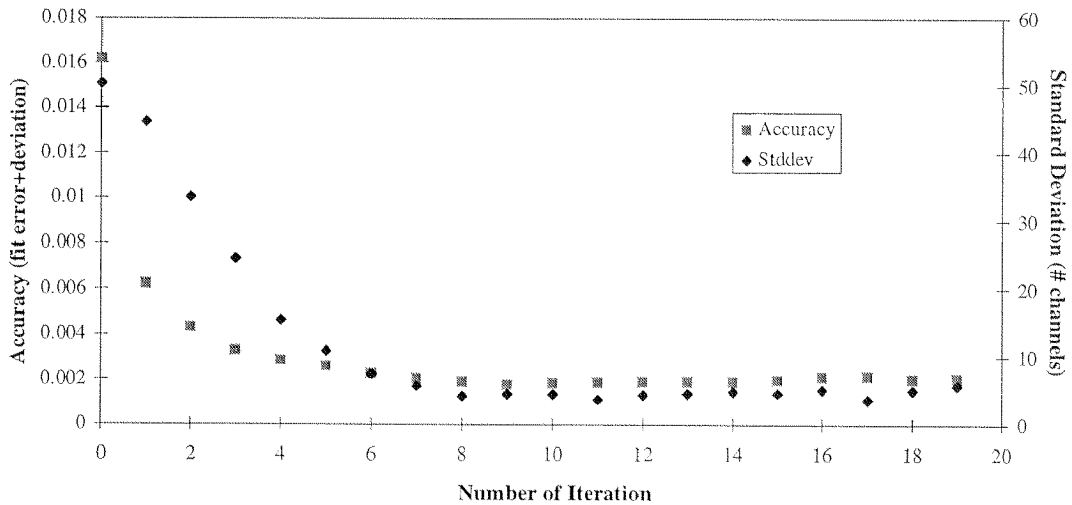


Figure 7-6 Convergence behaviour of the truncation condition. The accuracy was defined as the sum of standard deviation and the error of the fit.

Finally, the procedures converged after about a dozen iterations, as seen in the preceding figures. The iteration was continued until either all channels were matched with the required accuracy or neither the average peak-position nor the total error could be improved. For the case of results floating around a minimum, the iterative process was ended after 32 iterations. Then the best obtained result was written to the database file. An average peak position at channel 3206 with a standard deviation of better than 5 channels (or 0.2 MeV) was obtained for all relevant runs.

A set of reference histograms was established for the second step with the above mentioned GEANT code. The objective was a direct comparison of the simulated and measured crystal responses. To this end the RC events were selected by allowing only events, when the sums of all crystal channels exceeded

86.3 MeV. In the simulation 129 MeV photons were thrown uniformly onto the detector arrays. Histograms for each channel were established with the same energy constraint as for the data reference and stored as ASCII files. After the data histograms were generated, they were compared with the reference histograms using the minimum χ^2 method. Software gains in ranging from 0.85 to 1.2 were applied to the data histogram until the best match to the reference histogram was achieved. The obtained software gains for each run were stored in database files for further use in analysis. Repetitive runs with the obtained software gains showed that the spectra would not need further adjustment as a visual inspection can demonstrate (Figure 7-7). The outermost NaI modules were not included in this procedure because they had to act as a veto if their sum energy exceeded about 2 MeV.

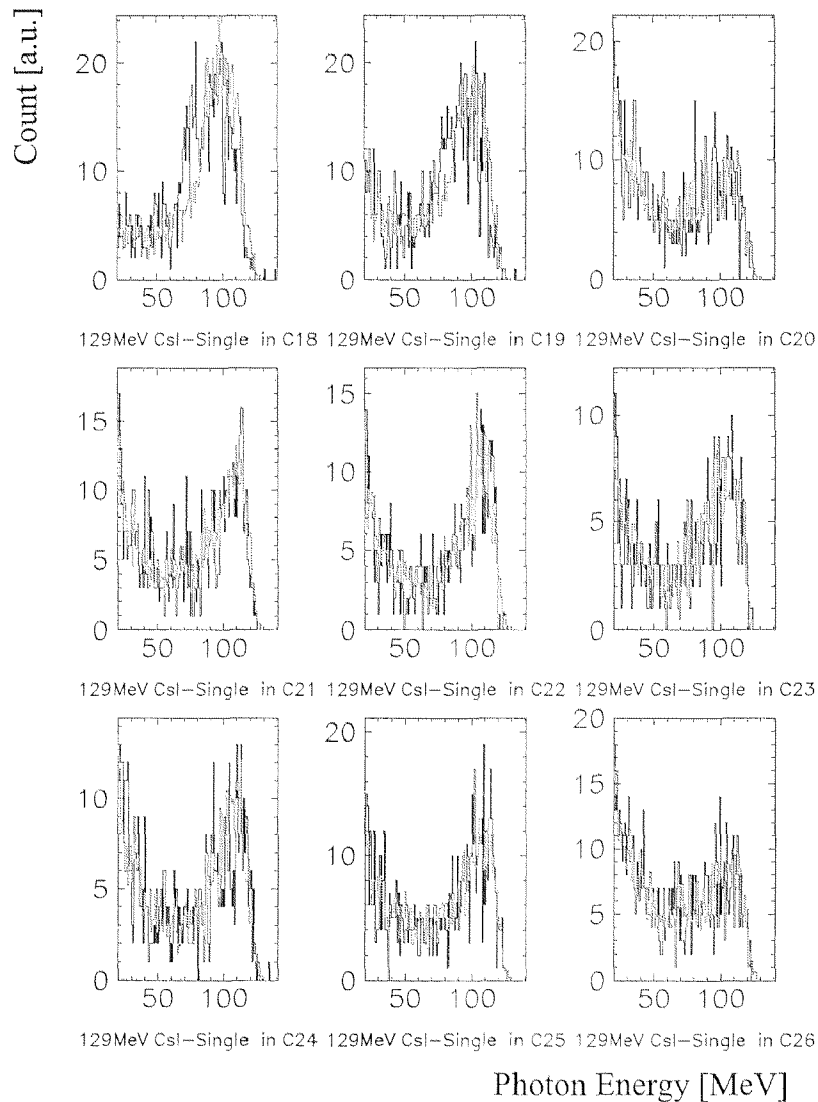


Figure 7-7 Direct comparison of individual spectra (9 out of 44). The number of counts is plotted against the photon energy. The black graphs represent the data, while the grey was obtained from simulation. Differences in the peak form are due to the position within the array. For example C26 and C20 are suffering similar losses due to a position close to an edge of the array.

Finally, the sum of the energy deposited in the array was built and consequently the simulated 129.4 MeV peak was used for calibration, because the individual spectra could be matched that well. In order to test for gain linearity a second energy reference was considered. This was the centre of the photon distribution from the π^0 -decay, which is positioned at 68.9 MeV. In order to obtain this centre the edges of the distribution were used. Since the theoretical box distribution is smeared in the same way as a

monoenergetic peak, the left side was fitted with an exponential curve and the right with a Gaussian. Then the midpoints of the two edges were defined as the position where the functions reached the value of half the distribution maximum. Finally, the centre was calculated as the arithmetic mean of the two midpoints. For an example of this fit see section 7.5 .

7.3 Geometric Corrections for Position Recognition

In chapter 4 the idea of position recognition was described, but this scheme had to be revised for the Panofsky ratio measurement, because the centre of the sphere no longer coincided with the reaction centre. As a result, the average shower propagation no longer follows the symmetry axis of the crystals and therefore corrections had to be applied.

The goal was the reconstruction of the impact point while the computed shower centroid would determine a point at most 10 cm within the calorimeter. The shower centroid only will have the same angular coordinates as the point of incidence when the shower develops parallel to the main crystal axis. Hence, this point has to be calculated where a connection line between the reaction centre and the shower centroid intersect with a crystal surface.

For a box-shaped crystal, as the used NaI, the relevant equation to calculate the point of incidence x would be $x=l*\sin(\phi)$, where l is the shower depth and ϕ the angle of incidence. In order to keep the computing time short rather than applying corrections for each obtained centroid, the crystal coordinates were transformed. Now instead of a crystal's front face the prospected mean shower depth for each crystal was used. This means that the crystal virtually was shifted such that a point s within each crystal had the same distance to the reaction centre as demonstrated in Figure 7-8.

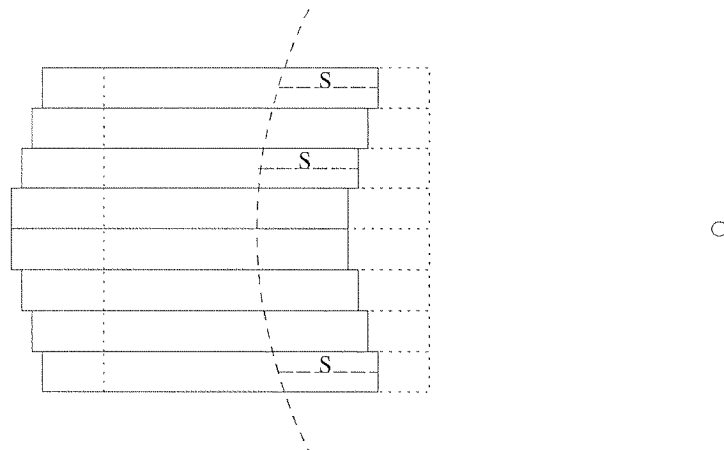


Figure 7-8 Sketch of the position reconstruction correction. The dashed lines represent the physical position of the crystals while the solid lines show the position corrected for the prospected shower mean. The shift was done such that a point s from the surface has the same distance to the shower centre (indicated by the arc).

After applying the position correction the angular resolution for 129 MeV photons uniformly impinging the NaI-wall improved from 1.22° to 1.09° (with an accuracy of $\pm 0.1^\circ$). The earlier mentioned weighting factor α was determined by optimizing the angular resolution. The optimal value was 1.0 in both cases.

A similar correction was calculated for the CsI array, which was necessary especially since the CsI sphere centre did not coincide with the centre of the target. This caused errors in the calculation of the incident point as can be seen in Figure 7-9.

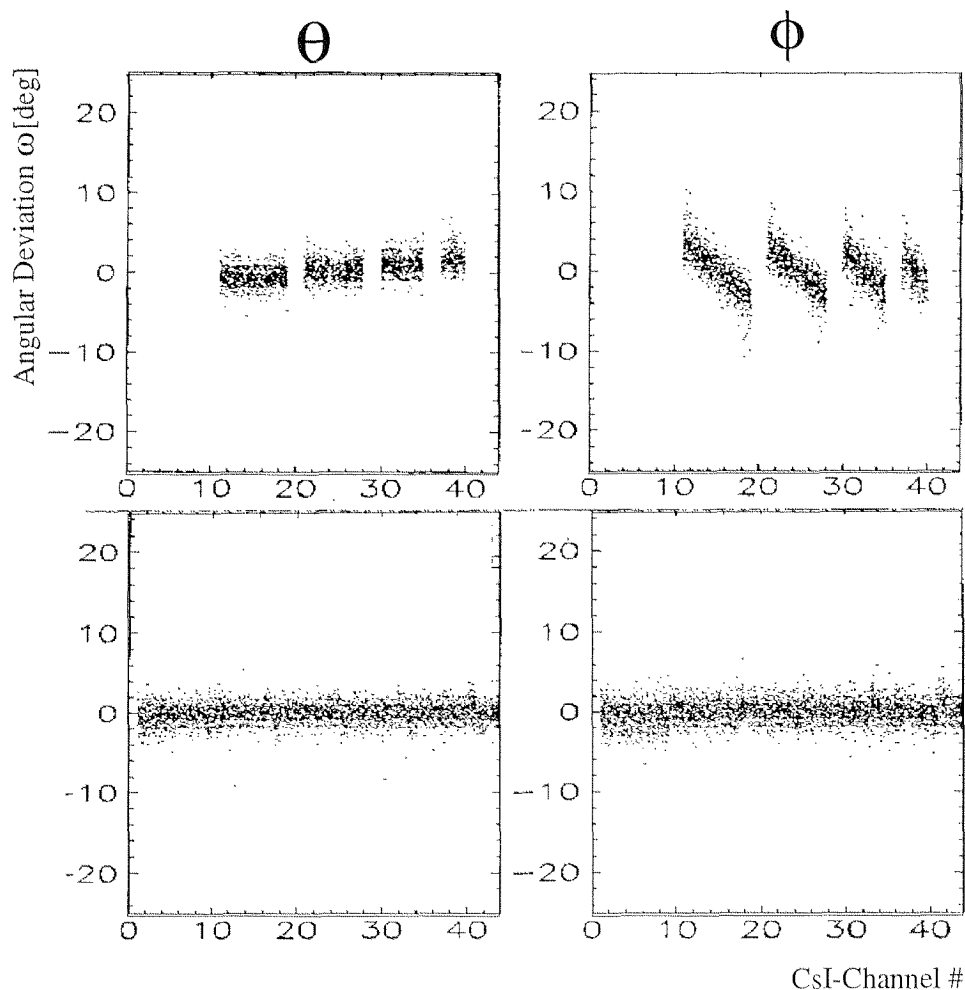


Figure 7-9 Reconstruction of the angle of incidence in θ and ϕ direction before and after correction. The deviation of the reconstructed angle is plotted for each CsI channel (1 through 44); for the definition of this angle ω see Equation 4.a.

A correction for the actual angle of incidence therefore was applied. As in the case of the NaI-wall all CsI coordinates were shifted to reach an identical radius such that each crystal front face was about 8 cm from the shower centroid. In order to obtain the correction, the calculation of the virtual crystal positions was optimized for angular resolution. By this the angular resolution after corrections was $1.28^\circ \pm 0.1^\circ$ compared to $2.05^\circ \pm 0.2^\circ$ for 129 MeV photons without the correction. Table 7-1 summarizes the results¹. There the angular resolution and the obtained position corrections are given for three energies for both calorimeters. These values are correlated with the obtained shower depths for the given energies. The positions of the calorimeters to the LH2-target centre were 100.2 cm for the NaI-wall and 55.9 cm for the centre of the CsI sphere.

¹ The better angular resolution in comparison with ch. 4 is due to the larger distance from the centre

γ -Energy		54.9 MeV	83 MeV	129 MeV
CsI	angular resolution	1.46 deg	1.37 deg	1.28 deg
	centre of the sphere	49.5 cm	49.3 cm	48.5 cm
NaI	angular resolution	1.24 deg	1.17deg	1.09deg
	centre of the wall	100.0 cm	100.5 cm	102.0 cm

Table 7-1 Angular resolutions of NaI-wall and CsI array. The accuracies amount 0.1° and 0.2 cm, respectively.

The distance corrections develop similarly for CsI and NaI. The direction for NaI is opposite because the correction factor has a different impact with respect to the given calorimeter positions: In the case of NaI the correction reflects the position of the centre of the wall that virtually moves back for higher penetration depths. In the case of CsI the difference between the physical position and the virtual position reflects the penetration depth of the shower.

These results demonstrate two facts that have been noted before.

- I) The angular resolution improves with higher energies. Due to a higher momentum secondary shower particles are more likely to follow the direction of incidence of the initial particle.
- II) The smaller difference of the corrections between 129 MeV and 55 MeV photons for CsI is due to a shorter radiation length compared to NaI.

The shower centroid and radial spread in NaI and CsI have been studied using GEANT. To this end the vector of each track has been histogrammed after the angle of incidence was calculated. With elementary trigonometrical relations the propagation along the crystal axis, along the position of incidence and perpendicular hereto can be computed. The obtained mean values for the three energies of interest are shown in Table 7-2. The results are in agreement with the obtained position correction and thus support the above interpretations.

	Energy	Photons			Positrons		
		55 MeV	83 MeV	129 MeV	55 MeV	83 MeV	129 MeV
CsI	shower depth	7.4 cm	7.8 cm	8.4 cm	5.0 cm	5.8 cm	6.6 cm
	shower cone radius	2.6 cm	2.5 cm	2.4 cm	2.8 cm	2.6 cm	2.4 cm
NaI	shower depth	10.8 cm	11.7 cm	12.6 cm	12.3 cm	12.0 cm	12.2 cm
	shower cone radius	4.1 cm	4.0 cm	3.9 cm	4.2 cm	4.1 cm	4.0 cm

Table 7-2 Shower parameters for photons and positrons. The accuracy (obtained from the r.m.s. of the simulated distribution) is about 0.2 cm.

7.4 Summing

Since the electromagnetic shower is distributing energy over several crystals, care has to be taken in the summing. So far the determination of electronic noise and the minimization of intercalibration effects have been treated. Consequently, a noise discrimination threshold for the summing and software gains for each calorimeter module were established. In this section an energy threshold for shower losses and an algorithm for building clusters will be introduced.

The most direct approach to form a cluster would be a sum of the overall energy content of the crystals. But then, whenever a shower develops close to the edge of the array, also events that do not deposit a

major fraction of energy within the detector would contribute. This results in an exponential tail to the left side of a peak. In order to cure that problem the outermost crystals should veto shower losses. This has to be achieved without omitting energy if the outermost crystals only contain a small fraction of the deposited energy while the major contribution comes from inner crystals. Hence, the vetoing requires an energy threshold to decide when to sum and when to drop. A plot of peak position and FWHM against the energy threshold gave a clear result for the needed threshold values. This was shown using simulations of different energy photons that were uniformly distributed over the array of 44 CsI crystals. Figure 7–10 shows the result for 129 MeV photons.

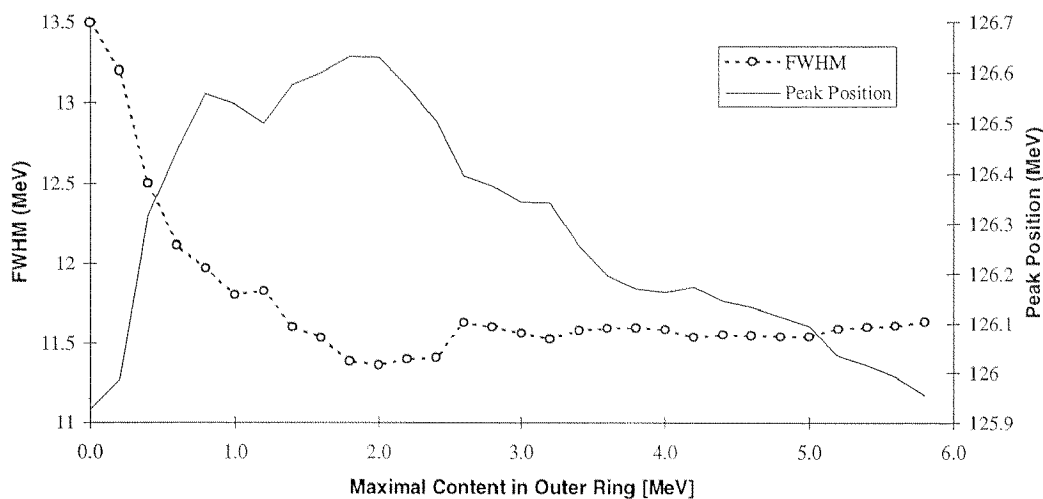


Figure 7–10 This figure illustrates the effect of a cut on the energy deposition in the outer ring of CsI crystals. The ordinate is showing the cut value, which is the maximum energy that is allowed in the outermost crystals. For 129 MeV photons uniformly distributed over the CsI array (simulation) the fitted peak position raises due to a higher total energy, but is falling again when energy loss makes an effect. The same can be observed for lower energies, but then the graph peaks at lower threshold energies. While the optimum energy resolution for a 129 MeV photon can be reached for a 2 MeV threshold this is 1.4 MeV for 83 MeV photons. The reason that it does not exactly scale with energy is that 129 MeV photons are causing a larger shower spread than 83 MeV photons.

Finally, a criterion is needed to determine whether the deposited energy in the calorimeter originates from a single particle, radiative decays or arbitrary coincidences. To this end a software algorithm should find the optimum set of crystals to add for each event rather than establishing fixed clusters. This routine needs to determine which crystals will be included in the sum accordingly to the shower maximum and the shower spread and, furthermore, if an event should be neglected. It would work similar to the clump finding algorithm described in section 5.1. In order to make a decision, knowledge about the normal shower spread within the calorimeter is needed.

Energy loss in matter (dE/dx) comes along with two elementary processes, ionization and radiation loss. The critical energy E_c ¹ of a material usually is defined by the energy where both processes have the same magnitude, hence

$$\left. \frac{dE}{dx} \right|_{ion} \Big|_{E=E_c} = \left. \frac{dE}{dx} \right|_{rad} \Big|_{E=E_c}$$

Then the position of the shower maximum can be modelled to be $\ln(E_0/E_c)X_0$, where E_0 is the shower energy and X_0 the radiation length [Ore88].

An energy distribution function $df(\phi)/d\cos(\phi)$ can be defined in analogy to the energy loss where $f(\phi)$ represents the energy function and ϕ the distance of a point within the array to the trajectory of the incident particle in spherical coordinates. In order to obtain f a simulation with 70 MeV photons that

¹ For NaI E_c is 17.4 MeV and 10.2 MeV for CsI; calculated using [PDG98]

were thrown uniformly onto the array of CsI crystals was carried out. Then the position of incidence was recorded as well as the total deposited energy. For each crystal the angular distance to the point of incidence was plotted against the fraction of deposited energy. This results in a 2-dimensional plot representing the energy distribution of electromagnetic showers, shown in Figure 7-11.

The discrimination function f has a range of values among (0,1). Then the decisions are as follows: if $f < 0$ the energy belongs to main shower, if $f > 0$ radiative decay or two particle detection is considered. A fit function with three free parameters was selected in order to contain 98% of the distribution¹, which is indicated by the line in Figure 7-11. This function turned out to be

$$f = 0.0246 \left\{ (1 + 30.15) e^{-30.15(1 - \cos(q))} + 3.4 \right\}.$$

It is used to allow summing over the appropriate set of crystals.

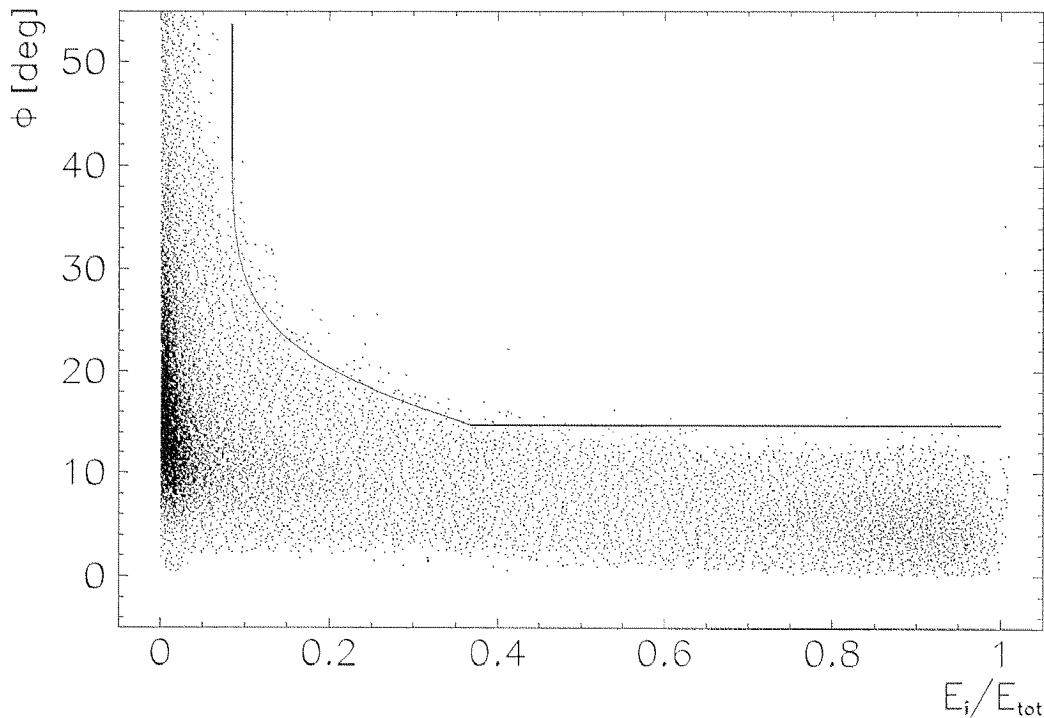


Figure 7-11 Scatter plot of the relative energy spread within the calorimeter. Plotted is the frequency of a certain distribution of angular distance ϕ of the i -th crystal to the shower centroid against the relative energy content $q_i = E_i/E_{tot}$. The solid line indicates the given threshold function with the additional constraints: q lower than 0.85 and ϕ less than 14.7° . One can notice that the majority of crystals close to the incidence point (near 10) contribute only with a few percentage of energy. The points with E_i/E_{tot} between 0.75 and 0.95 originate from individual crystals that carry the major fraction of total energy.

The algorithm for the summing follows the steps given in the description of the clump finding routine (section 5.1.1). The input to this routine is the energy deposited in the entire detector plus the individual energies and the coordinates of each crystal. With this information the routine sorts all crystals according to the energy content, starting from the one with the highest fraction. This crystal defines the initial cluster with its position and energy. All other crystals that are inside the area defined by the discrimination function are added to this cluster. The cluster's energy and position then are recalculated. By this, unlikely shower distributions, e.g. due to pair conversion in flight, and accidentals² can be excluded which also results in a slightly improved energy resolution. The summing routine led to a

¹ The application of the obtained threshold function to simulated positrons of the same energy resulted in an efficiency of 97%, which can be explained by the somewhat larger shower spread.

² For this measurement accidentals includes simultaneously detected photons and neutrons within the same region of the CsI array.

reduction of 6.3% FWHM before and 5.2% FWHM after cuts for 129 MeV photons and 7.6% and 5.8%, respectively, for 70 MeV photons. The determination of the detector acceptance takes care of that difference.

7.5 Data Analysis and Software Cuts

Although a relatively clean spectrum was achieved using gainmatching and the summing algorithm, sources of background and ambiguities had to be removed by software cuts. A major cut, which affected energy summing, was introduced in the previous section. The notable reduction of the tail was essential for a clean separation of the RC-peak and the SCX-distribution on one hand, and a separation of the SCX-distribution to low-energy background, on the other. The cut on the tail has different implication for both distributions of interests since the shower develops differently. The idea of two threshold values to account for the different energies, as introduced in the previous section, was not followed in order to avoid (uncorrectable) ambiguities. Consequently, 2 MeV was the allowed maximum contribution of the outermost crystals to the summed energy - as obtained accordingly to Figure 7–10. This restriction led to a reduction to 42% of the events in the case of SCX and to 37.5% in the case of RC. (These relations are uncorrected for background contributions and therefore an error is not given.) The benefits are a reduction of the systematical error. The error for the fit was reduced from 0.11% to 0.22% due to lower statistics. At the same time the contribution of the RC-peak tail under the π^0 -photons decreased from 0.95% to 0.27%.

The uncertainty of the result due to the applied cuts was determined by a variation of the cut parameters around the applied value. Then the fractional change of the obtained result for P beyond the change of the statistical error was recorded. Since the cuts are influencing one another also the covariance term was calculated to account for the correlation. This way the systematical error due to the applied cuts was obtained to be 0.44%. Hereby the contributions of the subsequently reported cuts are of the same order of magnitude. The main contribution to this error is due to differences in the simulated and measured distribution of the π^0 -photons. While the 129.4 MeV peak agrees well, the simulated photon distribution appears to be broader (Figure 7–12). The FWHM was determined to be 6.6% at 129.4 MeV obtained with a fit of the complete CsI-array sum comprising 4 days of beam time¹.

7.5.1 Simulation and Background Discussion

All of the steps concerning the cuts were included in the GEANT simulation. A beam of negative pions with 40 MeV kinematical energy was impinging the liquid hydrogen target after degradation. Having a nearly uniform beam profile of about 1 cm diameter, the stopping distribution within the target was obtained to be of Gaussian shape. The values for sigma amounted 0.86 cm, 0.74 cm and 0.92 cm in the x, y, and z direction, respectively. SCX or RC events were initiated from within this stopping distribution. In addition, possible background contributions due to pion interactions with matter were simulated. The main purpose of this simulation was the evaluation of the fit functions and the determination of the acceptance correction factor.

A target-empty run in a previous beam period did not lead to a notable count rate. This was confirmed by simulation. The percentage of beam pions and beam muons, as well, hitting the calorimeter either directly or after scattering amounted to $8.4 \cdot 10^{-3} \%$. After including plastic scintillator hodoscope and timing cut, the contribution of beam particles to the final data sample could be neglected.

¹ Without the applied gain matching the resolution would be 7.7%.

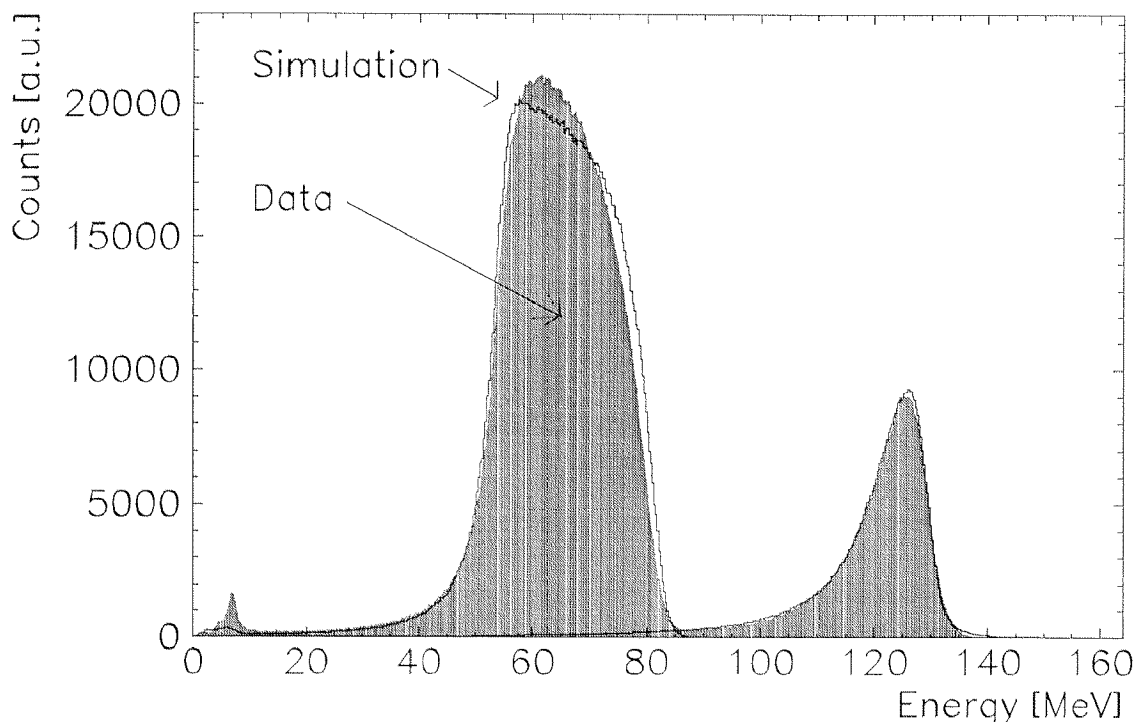


Figure 7-12 Overlay of data and simulation. In contrast to the well-matched RC peak, the SCX contribution could not be matched exactly by using the considered sources contributing to the energy resolution. This difference is reflected in the systematical error as described in the sections below.

The low energy background that is considered to be caused by bremsstrahlung of positrons or electrons, generated by photon conversion at the target walls, is disappearing thanks to the use of mylar windows in the target vessel. This is proved by the tail of the fit function smoothly following the data (see Figure 7-15).

7.5.2 Neutron Cut

The trigger gates could not be made with sufficiently small width to exclude all neutrons from RC to enter the detector accidentally with the opened calorimeter gate. Timing was determined by a hit of the CsI array exceeding 2 MeV of deposited energy. The flight distance and the timing resolution are sufficient to discriminate neutrons and photons. The time of flight (TOF) of the photons between the LH2 target and the CsI array amounts to 2.9 ns, while 8.9 MeV neutrons pass the 86 cm within 21.0 ns. Plotting the deposited energy in the calorimeter against the timing of B0- or B1-counter one observes the neutrons coming before the photons. As can be seen in Figure 7-13 the TDC spectrum of the B1-counter, for instance, clearly distinguishes photon and neutron response, together with beam related background.

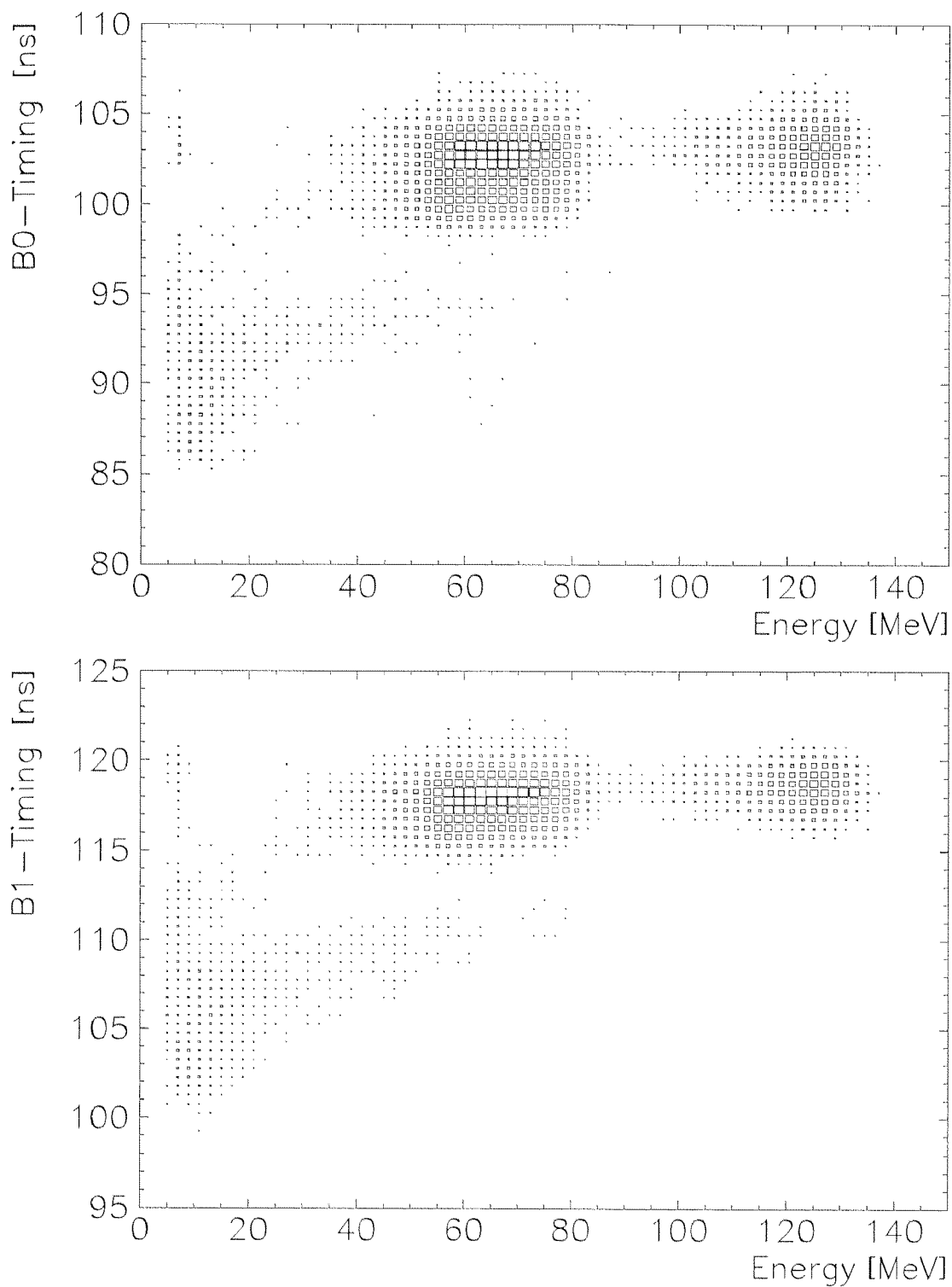


Figure 7-13. The timing of the B0 and B1 counters, triggered by a hit in the CsI calorimeter, is plotted against the energy deposition in the Calorimeter. Due to the time of flight difference most of the neutron background (see text for details).

In order to gain dynamic range the sum of the TDC values of B0 and B1 was used to cut out the neutron background ($225.3 \text{ ns} > T(B0)+T(B1) > 214.9 \text{ ns}$). This procedure additionally yielded a proper timing of the photons relative to the beam particles; the timing difference of the TDC peaks of B0 and B1 was

(15.5 ± 1) ns. 82% of the data passed this cut. As a result remaining neutrons¹ are well separated from the photons and do not contribute to the systematical error.

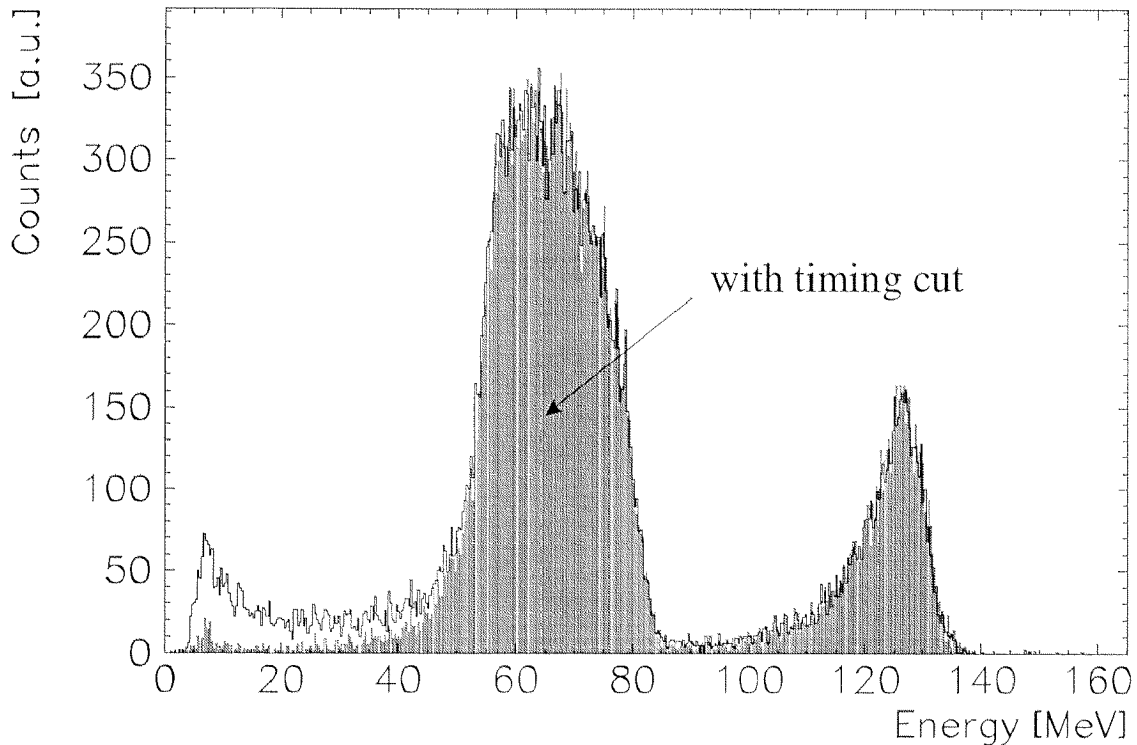


Figure 7-14 Demonstration of the effect of the timing cut. The low energy background disappears besides some well-separated neutrons.

The background in the energy range of the photons can be identified as coming from scattered beam pions (below 40 MeV) and - as shown in sect. 6.4 - bremsstrahlung photons, also in-flight SCX and RC on top of a neutron pulse would be possible. The ambiguity of the interpretation of the background below the SCX distribution contributes to the systematical error with 0.2%.

7.5.3 Hodoscope Cut

The CsI array, as well as the NaI-wall, was equipped with plastic scintillators at the front. This allows to cut out charged tracks. A charged particle here might have been generated by either scattered beam particles or converted photons. A cut requiring the energy deposition not to be above 0.51 MeV takes care of both sources. A multiplicative correction of 0.999 [Spu77] for suppressed electrons and positrons that originated either directly from RC and SCX or pair conversion of photons was applied for the final calculation of the Panofsky rate.

7.6 Photon Spectrum and Fit

After applying the above described cuts, a clean spectrum with two well-separated distributions emerged. The two peaks were fitted separately and the area under the peak was calculated as seen in Figure 7-15. The local minimum at 80.9 MeV was chosen as the separation limit between RC- and SCX- events. The RC-peak follows a Gaussian+exponential shape due to a $(1-e)$ like energy loss, as experienced in

¹ Some neutrons from a previous beam bucket happen to have nearly the timing - (21-19.75) ns - of the photons.

previous measurements using beam positrons and tagged photons [Bro96]. The theoretical distribution for SCX photons would be a box graph. Thus the left tail also was approximated by an exponential curve, while the right tail follows a Gaussian shape. This has been visualized by adding the simulated response to monoenergetic photons between 55 MeV and 83 MeV. This intermediate section best could be fitted with a parabola.

Finally, for the fit of both measured and simulated response to SCX photons, three subsections were pre-fitted using the above reported functions to obtain the starting values for the final fit. Then a function comprising the exponential curve, parabola and Gaussian with a total of 8 parameters was generated and fitted to the spectra using the MINUIT routine [PAW96]. The accuracy of this fit was determined with the fit errors calculated by MINUIT. The precision for the determination of the area under the fit function was 0.2%.

The tails of the fit functions also were used to estimate the RC content under the SCX distribution. Thanks to the clean cuts using the outer ring the low energy tail of the RC-peak has no more than 0.3% of its entries below 90 MeV. Due to the good energy resolution and the cut on the neutrons, the SCX distribution's right tail only contributes with $4 \cdot 10^{-4}$ per cent to the RC peak. As the left tail is concerned, unidentified low energy background, i.e. due to cut inefficiencies, was excluded owing to the fit function.

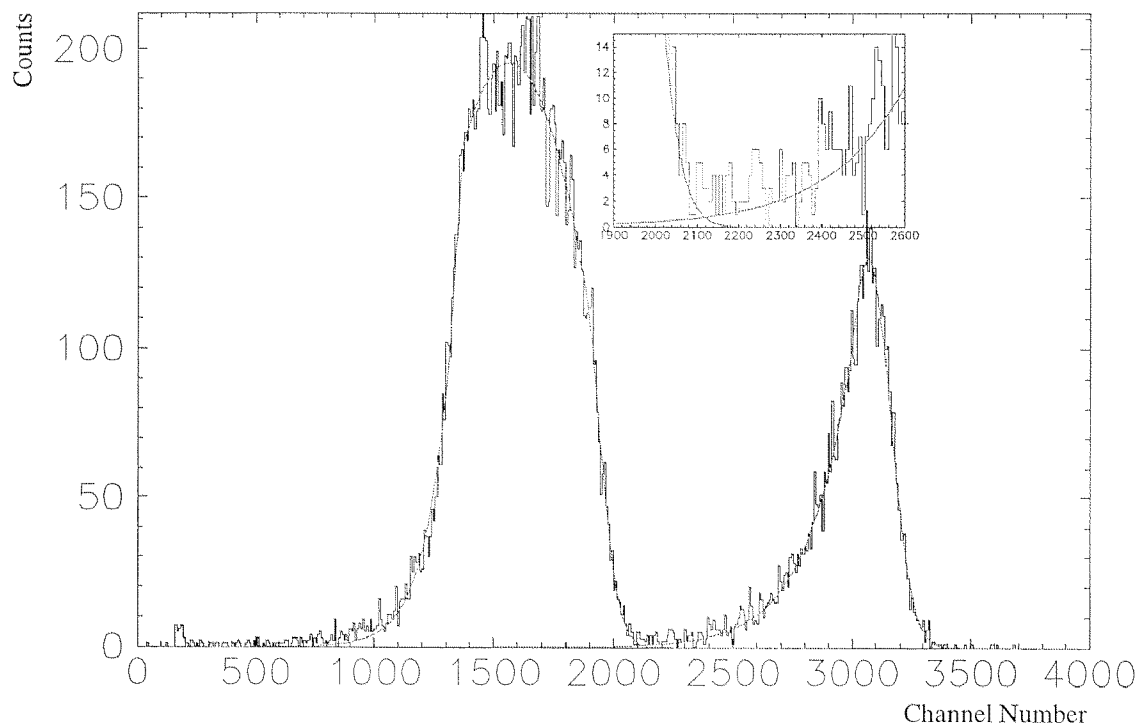


Figure 7-15 Typical data sample (from Run403) superimposed by the individual fit-functions (see text). The excerpt focuses the overlapping region and demonstrates a low contribution of each peak to the other.

In order to account for the influence of detector geometry and cuts for the determination of the Panofsky rate the detector acceptance was determined using the GEANT simulation and fit functions described above. An acceptance correction of $1.0327 \pm 0.42\%$ was obtained.

The final result after summing the individual data runs amounts to

$$1.5986/1.0327 \cdot 0.999 \pm (0.27\% \oplus 0.65\%) = 1.546 \pm 0.010.$$

The statistical error of 0.27% comprises 0.17% error from data and 0.10% from simulation. The systematical error is mainly caused by the uncertainty due the cuts and differences between simulated and measured spectra. Thus an improved accuracy for Panofsky ratio could not be achieved. Nevertheless the obtained value for P is in good agreement with the previous measurements [Spu77] and theory [Pan76]. A further discussion of the result will be given in the subsequent section.

7.7 Discussion of the Result and Calculation of the Scattering Length $a_1 - a_3$

Since the main topic of the measurements with the LH2 target was the calibration of the calorimeter with photons [Slo98] an optimal setup for a more precise determination of the Panofsky ratio was not achieved. In order to reduce the error due to acceptance correction and software cuts, the use of a properly designed collimator in front of the calorimeter seems to be preferable. Furthermore the response function of photons must be examined in more detail, despite the fact that the energy resolution and shower parameters could be matched well by the simulation. The shape of the distribution of SCX-photons is very sensitive to an assumed energy resolution function. Thus even a small deviation between the simulated response and the ‘real’ response function (which is not significant for monoenergetic photons) resulted in a relatively high systematical error for this measurement. Although major effort was put into the understanding of the shower distribution of photons at different energies a large contribution to the measurement error could not be avoided.

Author	Year, Reference	P	error
Panofsky et al.	[Pan50]	(0.94)	(0.30)
Sargent et al.	1955 ¹	1.10	0.50
Cassels et al.	1957 ¹	1.50	0.15
Fischer et al.	1958 ¹	(1.87)	(0.10)
Kuehner et al.	1959 ¹	1.60	0.17
Koller	1959 ¹	1.46	0.10
Dunaitsev et al.	1960 ¹	(1.40)	(0.08)
Derrick et al.	1960 ¹	1.47	0.1
Samios	1960 ¹	(1.62)	(0.06)
Jones et al.	1961 ¹	1.56	0.05
Cocconi et al.	[Coc61]	1.533	0.021
Ryan	[Rya63]	1.51	0.04
Spuller et al.	[Spu77]	1.546	0.009
This work		1.546	0.010

Table 7-3 Compilation of all published determinations of the Panofsky ratio. The values in brackets have not been used to calculate the weighted average.

A weighted average of all the measurements of P (listed in Table 7-3) which are in good agreement gives 1.543 ± 0.006 . For the calculation of the s-wave pion-nuclear cross-section b_1 , the transition amplitude at threshold $E_{0^+}^{\text{thr}}$ contributes the largest uncertainty. This uncertainty is limited by the extrapolation to the threshold; but is expected to be reduced by further measurements with energies closer to the πN threshold and electron-deuteron scattering [Han97]. However a more accurate P value can reduce ambiguities in the determination of either $E_{0^+}^{\text{thr}}$ or b_1 . Since the theoretical calculation of $E_{0^+}^{\text{thr}}$ is model dependent, we have taken the most actual determination of $E_{0^+}^{\text{thr}}$ by the E643 collaboration [Kov97]. Their value² of $-31.5 \pm 0.8 \cdot 10^{-3} / m_\pi$ coincides with the theoretical prediction using either low

¹ Quoted accordingly to [Rya63]

² So far, only the statistical error is given; a more detailed analysis is to be expected in 1999

energy theorem [Bae70] or chiral perturbation theory [Ber96]. The s-wave scattering length also is available through spectroscopy of pionic atoms [Sig96]. Nevertheless, the determined value for a_1 - a_3 differs for both approaches. A recent value from pionic-atom spectroscopy is at -0.2760 ± 0.0125 [Sch97] as opposed to -0.253^1 , both in units of m_π^{-1} . A refined calculation of the πN s-wave scattering length following Weinberg's current algebra [Ber96] puts the limits between -0.288 and -0.264 . On the other hand a calculation of the SCX scattering amplitude f based on a compilation of all available πN scattering data at low energies gives -0.0248 ± 0.0045 [Mat97] for the extrapolation to the threshold.

However, the latest analysis of the width of the $3p$ - $1s$ line of pionic Hydrogen and Deuterium including Doppler-shift corrections determined -0.2604 ± 0.0043 (preliminary) [Bad98]. Taking P from this work one obtains -0.252 ± 0.006 for a_1 - a_3 that translates into -0.085 ± 0.002 for b_1 . Thus there is evidence that the systematical discrepancy in the obtained scattering length disappears; although a further reduction of the measurement errors is needed. In fact, this calls for further studies of the s-wave scattering amplitude at threshold.

¹ No error given [Han97], but typically of about 3%

8. Conclusion

This work has introduced the physics of the study of the decay $\pi^+ \rightarrow \pi^0 e^+ \nu_e$ which is a fundamental manifestation of the weak interaction. With the use of the just assembled PiBeta detector the determination of its decay rate should be achievable to 0.5% precision. Such a result will produce a critical test of the standard model, since the theoretical calculation of the pion beta decay rate relies on the hypothesis of the universality of the weak interaction and unitarity of the CKM matrix. Also the detector and the considerations for its layout have been reported.

The steps necessary to achieve good energy resolution, namely optimization of the light yield and making the scintillator crystals uniform, as well as their quality control have been discussed. Results obtained with a Monte-Carlo simulation of the detector and their comparison to measurements were reported. The angular resolution of the detector was found to be $3.6^\circ \pm 0.2^\circ$. On top of a track reconstruction an algorithm was developed in order to decide about the origin of the particle(s) producing the shower(s). With the help of this algorithm the branching ratio for radiative pion decays in the low energy region was determined. For photons of 5 MeV emitted with an angle of at least 20° relative to the positron the probability was found to be $(2.9 \pm 1.2) \cdot 10^{-6}$ which is in good agreement with the calculated value of $2.7 \cdot 10^{-6}$.

After another beam period, where a liquid hydrogen target was used to produce photons via πN -interactions, the Panofsky ratio P was obtained. The analysis of the after necessary cuts well-separated photon distributions resulted in 1.546 ± 0.010 for P . Using the weighted average of the published Panofsky ratio values, the isovector πN scattering length b_1 amounts to -0.085 ± 0.002 inverse pion masses.

Appendix

Numerical Calculation of the rate of the radiative pion decay $\pi^+ \rightarrow e^+ \nu_e \gamma$

plot_pienug_x.kumac

Parameter:

- 1 γ
- 2 Threshold Energy
- 3 Threshold Angle

macro plot_pienug_x 1=0. 2=5. 3=55

* Macro to plot the terms, contributing to the radiative decay

* Formula from A.Stetz

* factorization after Bryman, units 10e-6

hi/del *

ve/del *

Application comis quit

```
subroutine calc_terms(gamma,x_thresh,Y_THRESH)
```

```
IMPLICIT NONE
```

```
int i,j,k,n_max,s,t
```

```
real x,y,l,ix,sum_y,y_thresh,gamma,y_energ,x_thresh,r_all
```

```
real hx,hy,xstart,ystart
```

```
REAL SD_p(30,30),SD_n(30,30),IB(30,30),INT_p(30,30),INT_n(30,30)
```

```
vector rate_IB(1),rate_SD_P(1),rate_SD_N(1),rate_INT(1)
```

```
VECTOR rINT_SD_p(30),rINT_SD_n(30),rINT_IB(30),
```

```
& rINT_INT(30)
```

```
data N_MAX,s,t /30,0,0/
```

```
xstart=x_thresh/139.57 *2.
```

```
ystart=y_thresh/139.57 *2.
```

```
hx=(1-xstart)/(n_max *1.-2.)
```

```
hy=(1-ystart)/(n_max *1.-2.)
```

```
print *,gamma,hx,hy
```

```
do i=1,N_MAX-1
```

```
x=xstart+(i-1)*hx
```

```
do j=1,N_MAX-1
```

```
y=ystart+(j-1)*hy
```

```
l=x+y-1.
```

```
ix=(y-1.)/x
```

```
if (l.gt.0.) then
```

```
IB(i,j)=(1.-y)/x/x*((x-1.)*(x-1.)+1.)/l
```

```
SD_p(i,j)=(1.-x)*l*(1.+gamma)**2
```

```
SD_n(i,j)=(1.-x)*(1.-y)*(1.-y)*(1.-gamma)**2
```

```
INT_p(i,j)=lx*(1.-x)*(1.+gamma)
```

```
INT_n(i,j)=lx*(x-1.-x*x/l)/x*(1.-gamma)
```

```
endif
```

```
enddo
```

```
enddo
```



```

rate_IB(1)=0.
    rate_sd_p(1)=0.
rate_sd_n(1)=0.
rate_int(1)=0.
DO i=1,N_MAX-1 ! threshold
rINT_IB(i)=0.
rINT_SD_p(i)=0.
rINT_SD_n(i)=0.
RINT_INT(I)=0.

do j=1,n_max-1

if (s.ne.4) then
s=4
else
s=2
endif
if (j.eq.1.or.j.eq.n_max-1) then
s=1
endif

rINT_IB(i)=rint_IB(i)+s *ib(i,j)
rINT_SD_p(i)=rint_SD_p(i)+s *SD_p(i,j)
rINT_SD_n(i)=rint_SD_n(i)+s *SD_n(i,j)
rint_int(I)=rint_INT(i)+s *INT_n(i,j)+s*INT_P(I,J)
enddo

if (t.ne.4) then
t=4
else
t=2
endif
if (i.eq.1.or.i.eq.n_max-1) then
t=1
endif
rate_IB(1)=rate_IB(1)+t *rint_IB(i)*hy/3.
rate_SD_P(1)=rate_SD_P(1)+t *rint_SD_P(i)*hy/3.
rate_SD_N(1)=rate_SD_N(1)+t *rint_SD_N(i)*hy/3.
rate_INT(1)=rate_INT(1)+t *rint_INT(i)*hy/3.

enddo

rate_IB(1)=.1436 *rate_IB(1)*hx/3.*1.e-6
rate_SD_P(1)=.2106 *rate_SD_P(1)*hx/3.*1.e-5
rate_SD_N(1)=.2106 *rate_SD_N(1)*hx/3.*1.e-5
rate_INT(1)=.004 *rate_INT(1)*hx/3.*1.e-6

r_all=rate_IB(1)+rate_SD_P(1)+rate_SD_N(1)+rate_int(1)
print *,r_all,rate_IB,rate_SD_P,rate_SD_N,rate_int

```

```

do i=1,30
  rINT_IB(i)=.1436 *rint_IB(i)*1.e-6*hy/3.
  rINT_SD_p(i)=2.106 *rint_SD_P(i)*1.e-6*hy/3.
  rINT_SD_n(i)=2.106 *rint_SD_n(i)*1.e-6*hy/3.
*   rint_INT_p(i)=0.004 *rint_INT_p(i)*hy/3.
*   rint_int_n(i)=0.004 *rint_INT_n(i)
  rint_INT(I)=0.004 *rint_INT(I)*1.e-6*hy/3.
enddo
end

quit

call calc_terms($RSIGMA([1]),$RSIGMA([2]),$RSIGMA([3]))
ve/cr gam_en(29) R
do i=1,29
  rtemp=[2]+[i]/29.*(139.57/2.-[2])
  ve/in gam_en([i]) [rtemp]
enddo
t= Limits [1], [2]MeV, [3]MeV
null [2] 70. 1.e-10 2.e-6
atitle E[g] 'Decay Rate'
itx 10 3.e-6 $quote([t])
RETURN

```

Bibliography

- [Aba95] S. Abachi et al., the D0 Collaboration: *Observation of the Top Quark*, Phys. Rev. Lett. 74,14 (1995) 2632
- [Abe95] S. Abe et al., the CDF Collaboration: *Observation of the Top Quark Production in $p\bar{p}$ Collisions*, Phys. Rev. Lett. 74,14 (1995) 2626
- [And52] H.L. Anderson, E. Fermi: *Scattering and Capture of Pions by Hydrogen*, Phys. Rev. 86 (1952) 794
- [Ass94] K. Assamagan et al.: *Measurement of the muon momentum in pion decay at rest using a surface muon beam*, Phys. Lett. B 335 231-236
- [Ass95] K. Assamagan et al.: *A precise determination of the pion beta decay rate: design and calibration*, Thesis (Univ. of Virginia), May 1995 (unpublished)
- [Bad98] J. Leisi, in: Proceedings of the PSI Summer school 1998, (to be published) and A. Badertscher, private communication, Nov. 1998
- [Bae70] P. de Baenst, Nucl. Phys. B24 (1970) 633
- [Bae77] H. Baer, K. Crowe, P. Truöl: *Radiative Pion Capture in Nuclei*, (Ch. 3 of *Advances in Nuclear Physics* Vol 9; ed.: M.Baranger, E.Vogt), Plenum Press, New York 1977
- [Bay86] A. Bay et al.: *Measurement of the Pion Axial Form Factor from Radiative Decay*, Phys. Lett. B 174,4 (1986) 445-449
- [Bay88] A. Bay et al.: *A Modular NaI(Tl) Detector for Intermediate Energy Photons*, NIM A271 (1988) 497-506
- [Beh56] R.E. Behrends, R.J. Finkelstein, A. Sirlin: *Radiative Corrections to Decay Processes*, Phys. Rev. 101,2 (1955) 866-873
- [Ber96] V. Bernard, N. Kaiser and U. Meißner, Phys. Lett. B383 (1996), 116
- [Bir64] J.B. Birks: *The Theory and Praxis of Scintillation-Counters*, Pergamon Press, Oxford, 1964, pp 473
- [Bir93] A.J. Bird et al.: *The Optimisation of Small CsI(Tl) Gamma-ray Detectors*, IEEE-NS 40,4 (1993) 395-399
- [Bis50] Bishop, Steinberger and Cook, Phys. Rev. 80 (1950) 291
- [Bol90] V.N. Bolotov et al. Phys. Lett. B, 243,3 (1990) 308
- [Bra93] B.B. Brabson et al.: *A study of two prototype lead glass electromagnetic calorimeters*, NIM A332 (1993) 419-443
- [Bro64] S.G. Brown, S.A. Budman: *Further Analysis of the Decay $\pi^+ \rightarrow e^+ \nu_e \gamma$* , Phys. Rev. 136,4B (1964) 1160
- [Bro95] J. Brose et al.: *CsI Crystal Uniformity Specification and Quality Control*, BaBar Note #175, unpublished
- [Bro96] Ch. Brönnimann: *The Pion Beta decay Experiment: Calibrations and Developments*, Thesis (Uni Zürich) April 1996, Shaker-Verlag, Aachen
- [Bry82] D.A. Bryman, P. Depommier, C. Leroy: *$\pi^+ \rightarrow e^+ \nu_e$, $\pi^+ \rightarrow e^+ \nu_e \gamma$ Decays And Related Processes*, Phys. Rep. 88,3 (1982) 151-205
- [Bry83] D.A. Bryman et al.: *New Measurements of the $\pi^+ \rightarrow e^+ \nu_e$ Branching Ratio*, Phys. Rev. Lett. 50,1 (1983) 7-10
- [Byr96] J. Byrne et al.: *A revised value for the neutron lifetime measured using a Penning trap*, Europhys. Lett., 33,3 (1996) 187-192
- [Cab63] N. Cabibbo, Phys. Rev. Lett. 10, 531 (1963)

- [Cam97] D. Campbell, private communication, 1997
- [Car79] R.L. Carrington et al.: *On the Detection of 50 MeV γ -Rays with a large Modularized NaI(Tl) Detector*, NIM 163 (1979) 203-220
- [Coc61] V.T. Cocconi et al., Nuovo Cim. 22 (1961) 494
- [Cra91] J.F. Crawford et al.: *Precision Measurement of the pion mass difference $m_{\pi^-} - m_{\pi^0}$* , Phys. Rev. Lett. 43 (1991) 46-58
- [Cri61] R. Crittenden, W. Walker, J. Ballam: *Radiative Decay Modes of the Muon*, Phys. Rev. 121,6 (1961) 1823
- [Cza93] G. Czapek et al., Phys. Rev. Lett. 70 (1993) 17
- [Dep63] P. Depommier et al.: *Further Measurements on the Decay $\pi^+ \rightarrow e^+ \nu_e \gamma$* , Phys. Lett. 7 No 4, 285-287
- [Dep68] P. Depommier et al. Nucl. Phys. B4 (1968) 189
- [Der82] E. Derenzo, J.K. Riles: *Monte Carlo calculations of the optical coupling between BGO crystals and photomultiplier tubes*, IEEE NS 29,1 (1982) 191-196
- [Eck50] S.G. Eckstein, R.H. Pratt: *Radiative Muon Decay*, Ann. Phys. 8 (1959) 297-309
- [Egl89] S. Egli et al., the SINDRUM collaboration, Phys. Lett. B22 (1989) 533
- [Eic83] W. Eichenberger, R. Engfer, A. van der Schaaf, Nucl. Phys. A412 (1983) 523-533
- [Enz58] H. Enz et J. Roussel: *Sur la luminescence de CsI et NaI*, Helv. Phys. Acta 31 (1958) 25-32
- [Eri88] T. Ericson, W. Weise: *Pions and nuclei*, Clarendon Press, Oxford, 1988
- [Ero90] B G Erozolimskii, Yad. Fiz. 52,6 (199) 1583
- [Fer34] E. Fermi: *Versuch der Theorie der β -Strahlen*, Zeitschr. f. Phys. 88 (1934) 161
- [Fey58] R.P. Feynman, M. Gell-Mann: *Theory of Fermi Interaction*, Phys.Rev. 109,1 (1958) 193-198
- [Gas88] J. Gasser, H. Leutwyler, Nucl. Phys. B 307 (1988) 779
- [Gas91] J. Gasser, H. Leutwyler, M.E. Saini: *Sigma-term update*, Phys. Lett. B 253 No. 1,2 (1991) 252o
- [Gla63] S.L. Glashow; *Partial-Symmetries of weak interactions*, Nucl. Phys. 22 (1961) 579-588
- [Gol58] M. Goldhaber et al., Phys. Rev. 109 (1958) 241
- [Gwi63] R. Gwin, R.B. Murray: *Scintillation Process in CsI(Tl)*, Phys. Rev. 131,2 (1963) 501-512
- [Ham95] N.M. Hamada et al.: *Suppression of the slow emission component in pure CsI by heat treatment*, NIM A365 (1995) 98-103
- [Han97] O. Hanstein, D. Drechsel, L. Tiator: *A dispersion theoretical approach to the threshold amplitudes of pion photoproduction*, Phys. Lett. B 399 (1997) 13-21
- [Hbo95] Application Software Group: *HBOOK-Statistical Analysis and Histogramming*, Reference Manual, CERN Geneva, Switzerland, 1995
- [Hil93] U.D. Hildenbrand: *Scintillation Detectors*, GSI-93-18 Preprint, Darmstadt, March 1993
- [Jan87] J.L. Jansons et al.: *Luminescence due to Radiative Transitions*, phys. stat. sol. (b) 144, 835 (1987)
- [Kal72] G. Källén, from *Quantum Electrodynamics: "Weak Interactions"* (ch. 7), Springer Verlag, New York, 1972

- [Kar98] V.V. Karpukhin et al.: *Cylindrical multiwire proportional chambers for the PIBETA detector*, to be published in NIM A (1998)
- [Kho95] N. Khomutov, private communication, 1995
- [Kob73] M. Kobayashi, T. Maskawa, Progr. Theor. Phys. 49, 652 (1973)
- [Kos97] V.T. Koslowski et al.: *The half-lives of ^{42}Sc , ^{46}V , ^{50}Mn and ^{54}Co* , NIM A401 (1997) 289-298
- [Kov97] M.A. Kovash: *Total Cross Sections for $\pi^- p \rightarrow n\gamma$ at 10 to 20 MeV*, πN Newsletter No.12 (1998), 51
- [Kub88] S. Kubota et al.: *A new scintillation material: Pure CsI with 10 ns Decay Time*, NIM A286 (1988) 275-277
- [Law98] D. Lawrence, Thesis, Univ. of Arizona, May 1998, unpublished and private communication
- [Lia97] P. Liaud et al., Nucl. Phys. A612,1 (1997) 53-81
- [Mak98] Aki Maki, Proceedings of the International Workshop JHF98, KEK, Tsukuba
- [Mar87] W.C. Marciano and A. Sirlin, Phys. Rev. D 35 (1987) 1672
- [Mar93] W.J. Marciano, A. Sirlin: *Radiative Corrections to π_{l2} Decays*, Phys.Rev. Lett. 71,22 (1993) 3629-3632
- [Mar93] W.J. Marciano, A. Sirlin: *Radiative Corrections to β -Decay and the Possibility of a Fourth Generation*, Phys.Rev. Lett. 56,1 (1986) 22-25
- [Mat97] E. Matsinos: *Isospin violation in the πN system at low energies*, Phys.Rev. C 56,6 (1997) 3014-3025
- [McF85] W.C. McFarlane et al.: *Measurements of the pion beta decay*, Phys.Rev. D 32,3 (1985) 547-565
- [Moh92] R.N. Mohaparta: *Rare Muon decays and physics beyond the standard model*, Zeitschr. f. Phys. C56 (1992) 117-128
- [Mos96] Yu A Mostovoi. K. N. Mukhin, O. O. Patarkin: *The neutron yesterday, today, and tomorrow*, Physics-Uspexhi 39 (9) 925-958 (1996) (translated from Uspheki Fizicheskikh Nauk 166 (9) 987-1022 (1996))
- [Nag91] A. Nagl, V. Devathan, H. Überall: *Nuclear Pion Photoproduction* (STMP Vol. 120), Springer-Verlag, Berlin 1991
- [Nob90] A.J. Noble, Thesis, University of British Columbia, 1990, unpublished
- [Ore88] Oreglia, Thesis, 1988, unpublished
- [Pan50] WKH Panofsky, R.L. Aamodt, J. Hadley: *The Gamma-Ray Spectrum resulting from Capture of Negative π -Mesons in Hydrogen and Deuterium*, Phys.Rev. 81,4 (1951) 565-574
- [PAW96] PAW (Physics Analysis Workstation) *Users guide Ver. 2.07*, CERN Program Library Q121, ed. CERN, Geneva 1996
- [PDG98] C. Caso et al, The European Physical Journal C3 (1998), 1
- [Per86] D.H. Perkins, *Introduction to High Energy Physics*, 3rd edition (1986), Addison-Wesley, Menlo Park, p.212
- [Pii86] L.E. Piionen et al: *Unique Determination of the Form-Factor ratio in Radiative Pion Decay*, Phys.Rev. Lett. 57 (1986) 1402-1405
- [Pob90] A. A. Poblaguev, Phys. Lett. B238,1 (1990) 108-111
- [Poc89] D. Pocanic et al.: *A precise measurement of the $\pi\beta$ -decay rate*, proposal R-89-01 (1989), unpublished (<http://pibeta.psi.ch/%7Epi-beta/docs/>)

- [Poc89] D. Pocanic et al.: *A precise measurement of the $\pi\beta$ -decay rate*, Status Update (1995), unpublished (<http://pibeta.psi.ch/%7EpiBeta/docs/>)
- [Ras76] G. Rasche, W.S. Woolcock: *The effect of Radiative Capture on Threshold πp Scattering and the Theory of the Panofsky ratio*, Helv. Phys. Acta 49 (1976) 557-567
- [Rit98] S. Ritt: *MIDAS User's and Programmer's Manual*, May 1998, unpublished
- [Rya63] J.W. Ryan: *Branching Ratios of Reactions of π^- Mesons Stopped in Hydrogen and Deuterium*, Phys.Rev. 130,4 (1963) 1554-1567
- [Sav95] G. Savard et al.: *^{10}C Superallowed Branching Ratio and the CKM-Matrix Unitarity*, Phys. Rev. Lett 74,9 (1995) 1521-1524
- [Sch90] P. Schotanus et al.: *Scintillation characteristics of pure and Tl-doped CsI crystals*, IEEE NS37,2 (1990) 177-182
- [Sch95] Schreckenbach et al., Phys. Let. B 349 (1995) 427
- [Sei96] R. Seitz: *Describing Energy Deposition in CsI Crystals*, BaBar Note#294, unpublished
- [Shr78] R.E. Shrock, L-L. Wang: *New, Generalized Cabibbo Fit and Application to Quark Mixing Angles in the sequential Weinberg-Salam Model*, Phys. Rev. Lett. 41,25 (1978) 161-163.
- [Sig96] D. Sigg et al., Nucl Phys. A 609 (1996) 269-309
- [Sir74] A. Sirlin: *Radiative Corrections to G_V/G_A in Simple Extensions of the $SU(2)\times U(1)$ Gauge Model*, Nucl Phys.B71 (1974) 29-51
- [Sir78] A. Sirlin: *Current algebra formulation of radiative corrections in gauge theories and the universality of the weak interactions* (1978) 573-605
- [Sir87] A. Sirlin: *Remarks concerning $O(Z\alpha^2)$ corrections to Fermi decays, conserved-vector-current predictions, and universality*, Phys.Rev. D 35,11 (1987) 3423-3427
- [Sir92] A. Sirlin, private communication, 1992
- [Slo98] P. Slocum, Thesis (Univ. of Virginia), Oct. 1998, unpublished
- [Smi75] J. Smith and W. Pong, Phys. Rev. B 12 5931 (1975)
- [Smi95] C. Smith, private communication, Feb.95
- [Spu77] J. Spuller et al. *A remeasurement of the Panofsky Ratio*, Phys. Lett. 67B,4 (1977) 479-482
- [Ste78] A. Stetz et al. Nucl. Phys. B138 (1978) 285-318
- [Stu42] ECG Stückelberg, Helv. Physica Acta 15 (1942) 23
- [Ua183a] UA1 Collaboration, Phys. Lett. B122 (1983) 103-116
- [Ua183b] UA1 Collaboration, Phys. Lett. B122 (1983) 398-410
- [Uts98] M. Utsuro et al., Proceedings of the International Workshop JHF98, KEK, Tsukuba
- [Wil94] D.H. Wilkinson: *Analysis of the super-allowed Fermi beta-decay*, TRI-PP-94-102, Nov 1994, unpublished and *G_V , CKM Unitarity, neutron decay; W_R ?*, Z. Phys. A 348 129-138 (1994)
- [Wil97] D.H. Wilkinson: *Evaluation of beta-decay, Part VI*, NIM A401 (1997) 275-280
- [Woo83] G. Woody et al., IEEE-Trans. Nucl. Sc. 37 (1983) 492
- [Wu57] C.S. Wu et al., Phys. Rev. 105(1957) 1413
- [Wus96] Graig Wuest, private communication, 1996

List of Figures and Tables

Figure 2-1 Cross section the PiBeta detector	20
Figure 2-2 Plastic Scintillator Hodoscope strips in assembly	22
Figure 2-3 Spectrum obtained with Hodoscope	22
Figure 2-4 Support Structure	23
Figure 2-5 Timing of Trigger	24
Figure 2-6 Scheme of Clusters and Superclusters	25
Figure 2-7 PiBeta detector	25
Figure 3-1 CsI Calorimeter	28
Figure 3-2 Fundamental Triangle from Geodesic Breakdown	28
Figure 3-3 Linear Attenuation Coefficient of CsI as a function of photon energy.	30
Figure 3-4 Atypical shower distributions of 50 MeV photons	30
Figure 3-5 Light Emission Spectrum of pure CsI.....	31
Figure 3-6 Response function of CsI crystal to cosmic muons	33
Figure 3-7 Comparison of common reflecting materials	35
Figure 3-8 Influence of uniformity from treatment of the front side	35
Figure 3-9 Cut through the Crystal Tomography Apparatus	38
Figure 3-10 Two dimensional tomography pictures of a CsI crystal	38
Figure 3-11 CsI crystal uniformity obtained with a Cs source and cosmic muons	39
Figure 3-12 Layout of the RASTA apparatus	40
Figure 3-13 Determination of light yield.....	41
Figure 4-1 CsI assembly	42
Figure 4-2 CsI assembly	43
Figure 4-3 Detector Acceptances	44
Figure 4-4 Angular resolution and position reconstruction	47
Figure 4-5 Differences in angular resolution for positrons and photons	48
Figure 4-6 Comparison of the angular resolution of photons and positrons at different energies.	48
Figure 4-7 Comparison of measured and simulated angular resolution.....	49
Figure 4-8 Photograph of the 1996 CsI detector array.....	50
Figure 4-9 Energy resolution of the CsI array	51
Figure 5-1 The Kinematics of the $\pi^+ \rightarrow e^+ \nu_e \gamma$ decay	54
Figure 5-2 Detector acceptances for radiative pion and muon decay	54
Figure 5-3 Numerical evaluation of the terms contributing to the $\pi^+ \rightarrow e^+ \nu_e \gamma$ decay rate	58
Figure 6-1 Area layout for the measurements with the LH2 target	64
Figure 6-2 Picture of the CsI array.....	65
Figure 6-3 Trigger logic for the measurement of the Panofsky ratio	66
Figure 6-4 Kinematics of the charge exchange reaction at rest	67
Figure 7-1 Pedestals and Noise	70
Figure 7-2 Evaluation of the noise threshold	71
Figure 7-3 Typical π^0 spectrum (max. in CsI).....	72
Figure 7-4 Typical π^0 spectrum (max in NaI).....	72
Figure 7-5 Gain matching progress (peak position)	73
Figure 7-6 Gain matching progress (accuracy).....	73
Figure 7-7 Comparison of simulation and data for gain matching	74
Figure 7-8 Position Reconstruction (geometric correction).....	75
Figure 7-9 Reconstruction of the angle of incidence in θ and ϕ direction	76
Figure 7-10 Evaluation of cut on shower losses	78
Figure 7-11 Shower distribution within the calorimeter and evaluation of a threshold function	79
Figure 7-12 Overlay of data and simulation.	81
Figure 7-13 Visualization of the timing cut	82

<i>Figure 7-14 Result of the timing cut</i>	83
<i>Figure 7-15 Photon spectrum of Panofsky ratio measurement superimposed by fit functions</i>	84
<i>Table 2-1 Classification of β-decays</i>	13
<i>Table 2-2 Classification of Quarks and Leptons</i>	14
<i>Table 2-3 π and μ decay modes and probabilities</i>	19
<i>Table 3-1 Properties of CsI</i>	29
<i>Table 3-2 Improvements due to optical coating</i>	37
<i>Table 4-1 Gain matching of simulation</i>	46
<i>Table 4-2 Summary of the obtained energy resolutions</i>	52
<i>Table 5-1 Acceptances for radiative pion and muon decay modes</i>	55
<i>Table 5-2 Listing of the $\pi^+ \rightarrow e^+ \nu_e$ runs</i>	57
<i>Table 5-3 Compilation of measurements of the radiative pion decay rate</i>	58
<i>Table 7-1 Angular resolutions of NaI-wall and CsI array</i>	77
<i>Table 7-2 Shower parameters for photons and positrons</i>	77
<i>Table 7-3 Compilation of all published determinations of the Panofsky ratio</i>	85

Acknowledgements

Zunächst möchte ich Herrn Prof. Dr. Hofer danken für die Aufnahme an das Labor für Hochenergiephysik des Teilchenphysik-Institutes der ETH Zürich. Durch die Ermöglichung der Doktorarbeit konnte ich interessante Aufgaben in Forschung und Lehre auf hohem Niveau kennenlernen.

Herrn Prof. Dr. Hans-Christian Walter gebührt Dank für die Aufnahme in die Forschungsabteilung des PSI. Die spannende Arbeit und das internationale Umfeld, die Mannigfaltigkeit an physikalischem Wissen und das sehr angenehme Arbeitsklima werden mir in guter Erinnerung bleiben. Danke auch für ein kritisches Gegenlesen und die Übernahme der Korreferentschaft.

Den größten Anteil am erfolgreichen Abschluß meiner Forschungstätigkeit hat Dieter Renker, der zu Tages- und Nachtzeiten stets ein offeneres Ohr (nicht nur) für physikalische Probleme hatte und es schaffte, mich mit dionysisch-lukullischer Umrahmung und sanftem Druck stets ein weiteres Stück voranzubringen; und der außerdem die Mühe nicht scheute, auch unreife Schriftergüsse zu kommentieren.

It's unfair to emphasize certain people of the PiBeta collaboration, since I often recall in general the sophisticated way of working and discussion within this group; however there are some special thanks that I have to pronounce:

Dinko has an admirable discipline of scientific work, which I unfortunately never will come close to. His way of encouragement and oodles of ideas have been extremely helpful for me.

Stefan wird mir als unbestreitbarer Computerexperte und scheinbar müheloser Organisator auch schwerer Aufgaben in Erinnerung bleiben. Auch wenn mein Programmierstil, so fürchte ich, recht chaotisch geblieben ist, konnte ich doch viel von ihm lernen.

I raise the glass to Emil, who - amongst others - gave me memorable experience while being in Charlottesville and joyous moments at and off work. His irresistible chin-up mentality often was encouraging. Not the less I appreciated his expertise concerning simulations.

Nicht vergessen werden sollten die hilfreichen Beiträge früherer PiBeta Mitglieder - namentlich Ketevi und Christian - auf deren Arbeit ich bestens aufbauen konnte. Additional thanks to my fellow Ph.D. students Penny and Dave for discussions concerning computing, data handling and analysis problems.

hp, der inzwischen auch das PiBeta Team verstärkt, war in all den Jahren, in Arbeit und Freizeit, ein verlässlicher Ratgeber und Kritiker, und trug maßgeblich dazu bei, daß ich mich hier rundum wohlfühlen konnte.

Zdenek war ein stets hilfsbereiter Geist, auch wenn es darum ging, dringende - teils unmögliche - Aufträge zu erledigen. Ein wahrer Meister an Bohrmaschine, Grill und Kochtopf.

Res Badertscher und Evangelos Matsinos sei gedankt für hilfreiche Diskussionen π -N Reaktionen betreffend.

Jörg Schottmüller danke ich für die Überlassung der LH2-Target Geometrie für die GEANT-Simulation.

Thanks to Danek for being a wonderful roommate and friend. I enjoyed the dialogues about Jazz, classical music, history etc. and the numerous cordial welcomes at his place. He is also indisputable expert on Fortran and GEANT.

For a quick reference in the quest of words I appreciated dict.leo.org; but I am indebted to Dinko for a critical review of my humble language skills.

Meinen Eltern möchte ich danken, daß sie mich stets unterstützt haben und immer an meinem beruflichen Vorankommen interessiert waren; auch wenn sie inhaltlich von meiner Arbeit nicht profitieren können.

Klara, Danke dafür, daß es immer mehr geben wird als Teilchen und Materie.

Curriculum Vitae

Persönliche Daten

Name	Thomas Flügel
Geburtsdatum	7. November 1968
Geburtsort	Frankfurt am Main
Wohnort	Gansingerstrasse 77, 5236 Remigen
Nationalität	deutsch
Familienstand	ledig

Schulbildung

1975 - 1979	Gruneliuschule, Grundschule, Frankfurt-Oberrad
1979 - 1988	Carl-Schurz-Schule, Gymnasium, Frankfurt-Sachsenhausen

Abschluss: Allgemeine Hochschulreife

Studium und Beruf

1988 - 1994	Studium der Physik an der Johann-Wolfgang Goethe Universität, Frankfurt Diplomarbeit am Institut für Kernphysik und bei der Gesellschaft für Schwerionenforschung, Darmstadt bei Herrn Prof. Dr. Th. Elze
-------------	--

Abschluss: Diplom in Physik

1994 - 1998	Wissenschaftlicher Mitarbeiter am Paul Scherrer Institut, Villigen Assistent an der Eidgenössischen Technischen Hochschule Zürich Doktorand unter der Leitung von Herrn Prof. Dr. H. Hofer
-------------	--